Energy Efficient Digital Logic Using Nanoscale Magnetic Devices

Brian Lambson

Electrical Engineering and Computer Sciences
University of California at Berkeley

Technical Report No. UCB/EECS-2013-55
http://www.eecs.berkeley.edu/Pubs/TechRpts/2013/EECS-2013-55.html

May 10, 2013

Energy Efficient Digital Logic Using Nanoscale Magnetic Devices

by

Brian James Lambson

A dissertation submitted in partial satisfaction of the
requirements for the degree of
Doctor of Philosophy

in

Electrical Engineering and Computer Science

in the

Graduate Division

of the

University of California, Berkeley

Committee in charge:

Professor Jeffrey Bokor, Chair
Professor Sayeef Salahuddin
Professor Irfan Siddiqi

Spring 2013

Energy Efficient Digital Logic Using Nanoscale Magnetic Devices

Abstract

Energy Efficient Digital Logic Using Nanoscale Magnetic Devices
by
Brian James Lambson
Doctor of Philosophy in Electrical Engineering and Computer Science
University of California, Berkeley
Professor Jeffrey Bokor, Chair

Increasing demand for information processing in the last 50 years has been largely satisfied by the steadily declining price and improving performance of microelectronic devices. Much of this progress has been made by aggressively scaling the size of semiconductor transistors and metal interconnects that microprocessors are built from. As devices shrink to the size regime in which quantum effects pose significant challenges, new physics may be required in order to continue historical scaling trends. A variety of new devices and physics are currently under investigation throughout the scientific and engineering community to meet these challenges.

One of the more drastic proposals on the table is to replace the electronic components of information processors with magnetic components. Magnetic components are already commonplace in computers for their information storage capability. Unlike most electronic devices, magnetic materials can store data in the absence of a power supply. Today's magnetic hard disk drives can routinely hold billions of bits of information and are in widespread commercial use. Their ability to function without a constant power source hints at an intrinsic energy efficiency. The question we investigate in this dissertation is whether or not this advantage can be extended from information storage to the notoriously energy intensive task of information processing.

Several proof-of-concept magnetic logic devices were proposed and tested in the past decade. In this dissertation, we build on the prior work by answering fundamental questions about how magnetic devices achieve such high energy efficiency and how they can best function in digital logic applications. The results of this analysis are used to suggest and test improvements to nanomagnetic computing devices. Two of our results are seen as especially important to the field of nanomagnetic computing: (1) we show that it is possible to operate nanomagnetic computers at the fundamental thermodyanimic limits of computation and (2) we develop a nanomagnet with a unique shape that is engineered to significantly improve the reliability of nanomagnetic logic.

Contents

Contents i

1 Introduction **1**
1.1 Energy and Information . . . 1
1.2 Background . . . 3
1.3 Tools and Techniques . . . 8
1.4 Summary . . . 9

2 Nanomagnetic Logic and the Thermodynamic Limits of Computation **10**
2.1 Landauer's Principle in Nanomagnets . . . 10
2.2 Approach . . . 11
2.3 Nanomagnetic Logic . . . 17
2.4 Discussion . . . 19

3 Magneto-optical investigation of Landauer erasure in nanomagnets **20**
3.1 Experimental Verification of Landauer Erasure Simulations . . . 20
3.2 Survey of Measurement Techniques . . . 21
3.3 MOKE Measurement of Landauer Erasure . . . 23
3.4 Discussion . . . 32

4 Signal Transmission in Nanomagnet Chains **34**
4.1 Implications of Landauer's Principle . . . 34
4.2 Adiabatic Mode of Transmission . . . 35
4.3 Time-Lapse PEEM Imaging of Adiabatic Mode . . . 37
4.4 Thermal Clocking . . . 40
4.5 Soliton Mode of Transmission . . . 42

5 Study of the Reliability of Nanomagnet Chains **46**
5.1 Limitations of Fabrication . . . 46
5.2 Approach . . . 46
5.3 Errors in ideal chains . . . 48
5.4 Experimental data . . . 51

5.5 Simulation data 52
5.6 Discussion 55

6 Anisotropy Properties of Concave Nanomagnets 57
6.1 A Need for Anisotropy Control 57
6.2 Existing Methods for Anisotropy Control 58
6.3 Anisotropy in Concave Nanomagnets 60
6.4 Discussion 64

7 Improving the Reliability of Nanomagnetic Logic 66
7.1 Concave Nanomagnets in Nanomagnetic Logic Applications 66
7.2 Simulation Study of Concave Nanomagnets 67
7.3 Experimental Verification 69
7.4 Discussion 73

8 Conclusion 75
8.1 NML: Addressing Societal Needs Through Innovation 75
8.2 Next Steps 76

A Nanomagnetic device fabrication 78

B Nanocharacterization: MOKE and PEEM 81
B.1 MOKE 81

I title 86
B.2 PEEM 92

C Micromagnetic simulations 94
C.1 MATLAB Simulations 94
C.2 OOMMF Simulations 99

Bibliography 102

Chapter 1

Introduction

1.1 Energy and Information

Over the last 60 years, the cost of components used in electronic information processors has declined at a consistent exponential rate, a trend that was first pointed out by Gordon Moore of Intel Corporation [1]. During this period, information technology has played an increasingly prominent role in society. Highlights include the emergence of personal computers in the 1980's, the Internet in the 1990's, and mobile communication devices in the 2000's.

In parallel with declining costs, the size, speed, and energy efficiency of digital logic devices have also improved exponentially. It was recently observed by Koomey *et al.* [2]

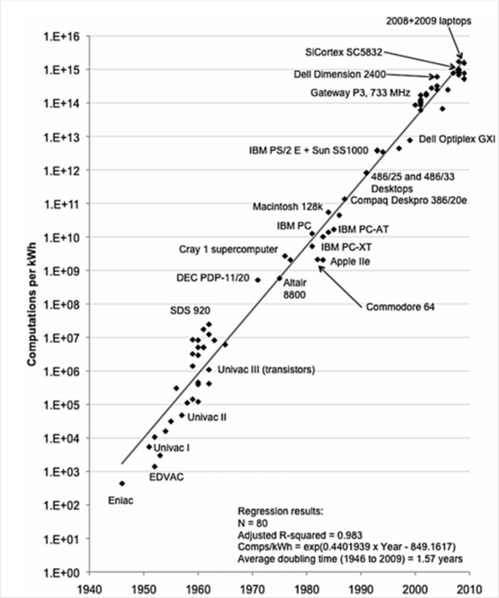

Figure 1.1: Exponential improvement in the energy efficiency of computers over time [2].

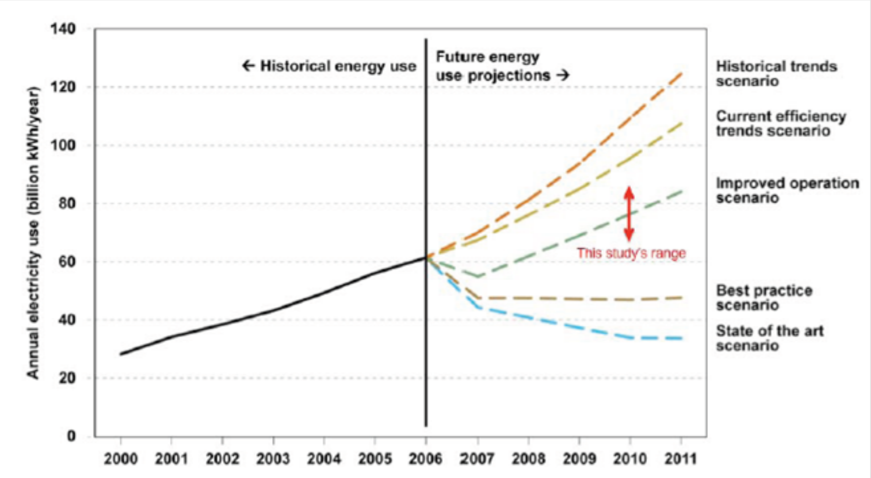

Figure 1.2: Rising energy consumption in data centers [3].

that the energy efficiency of computers, measured in computations per kilowatt-hour, has doubled about once every 1.6 years since the 1940's. The graphic shown in Fig. 1.1 indicates this trend on a logarithmic scale. That means that for the same amount of energy that was required to carry out a single computation at the advent of the information age, it is now possible to carry out over a trillion similar computations.

As computers have become more energy efficient, society has put many more of them to use. In fact, the growth in the usage of computers in some applications has outpaced the energy efficiency improvements shown in Fig. 1.1. As a result, the net consumption of energy has increased over the years. An example of an application where energy consumption is increasing is data centers [3], shown in Fig. 1.2. Between the years 2000 and 2006, the net energy consumption consumed in data centers in the U.S. doubled. Such a trend is both economically and environmentally costly, giving a strong incentive to pursue the development of more efficient computing technologies.

Further motivation for the development of efficient computing technologies is related to new applications that may be enabled by increased energy efficiency. Just as today's mobile computing technologies such as laptops, tablets, and smart phones are made possible by their ability to function using scarce energy resources, future computing paradigms such as smart dust, wireless sensor networks, and ubiquitous embedded microprocessors demand even better efficiency. Some of the benefits of more energy efficient computers are predictable; others we will only recognize in hindsight.

Today's computing technology is based on controlling the flow of electric charge by modulating the resistivity of semiconductor materials. Generally speaking, the smaller the semiconductor components are, the more efficiently they can modulate electric current. Soon, fundamental limits to component scaling will be reached [4]. To continue improving microprocessor technology, new physical phenomena need to be introduced into microprocessor components. Future devices may incorporate quantum tunneling effects, mechanical actuation, optics, or magnetics, among other phenomena. Of those, magnetics, or more generally electron spin, has the highest potential for approaching fundamental limits to energy efficiency.

Motivated by trends in magnetism and computing, as well as the desire to experimentally achieve fundamental thermodynamic limits to computation, this dissertation investigates the prospect of building computing devices from nanoscale magnetic elements. It builds on the findings of many pioneering researchers in this field. It is noteworthy that no novel physical phenomena are proposed or investigated here, only unexplored combinations of earlier known principles. Many of these principles are drawn specifically from three subfields of physics and engineering: energy efficient computing, magnetism and magnetic materials, and the thermodynamic limits of computation. In the next section, key developments in these three fields are surveyed.

1.2 Background

Trends in Energy Efficient Computing

The building blocks of today's computing devices are currently only a few tens of nanometers in size and are fast approaching fundamental limits to their continued scaling. At the same time, practical issues related to the heat density of electrically active nanostructures have already slowed improvements in the performance of microprocessors. Even if progress in device scaling were to continue indefinitely, the rate at which they produce heat demands attention now. As a result, many recent research efforts have been dedicated to the emerging field of energy efficient electronic devices. The goal of these efforts is to harness physical phenomena that occur uniquely at the nanoscale into digital logic components for improved energy efficiency relative to conventional CMOS devices.

At UC Berkeley, the Center for Energy Efficent Electronics Science (E3S) was established in 2010 to take on the challenge of reducing the power consumption of future digital logic devices. The center divides efforts into four focus areas, or themes: (1) nanoelectronics, (2) nanomechanics, (3) nanophotonics, and (4) nanomagnetics. Nanoelectronics explores logic devices that harness quantum tunneling phenomena through the careful engineering of device's bandstructure and geometry [5]. Nanomechanics explores the use of electrostatics forces to achieve switching behavior in nanoelectromechanical systems (NEMS), taking advantage of the nonlinear impact of device scaling on power consumption [6, 7]. Nanophotonics and nanomagnetics use light and electron spin, respectively, to transmit information, circumventing the resistive losses that occur in electronic charge-based devices.

To a rough approximation, the four E3S themes are ordered by how far along they are in their development. Theme 1, nanoelectronics, is arguably the approach to energy efficient computing that is closest to market, because the devices physically resemble conventional CMOS devices most closely. If a breakthrough is made in nanoelectronics, it is not difficult

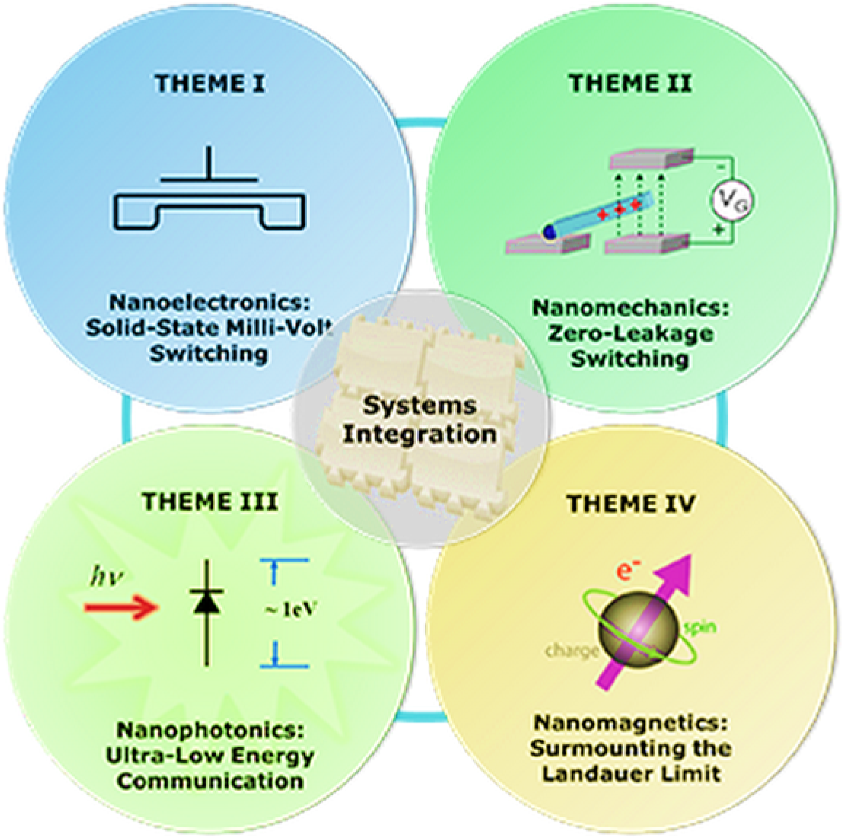

Figure 1.3: Source: Center for Energy Efficient Electronics Science

to imagine rapid deployment and scaling through modest modification of modern foundry capabilities. On the other end of the spectrum, nanomagnetics is a high risk, high reward approach. Building a device architecture in which the spin degree of freedom, not charge, stores and processes information is a radical departure from conventional architectures. It would likely take a very long time to fully realize a market-ready nanomagnetic computing device, but it is perhaps the long-term solution that offers the most potential benefit of the four themes, including the highest achievable energy efficiency. Other unique benefits of nanomagnetic computing include intrinsic radiation hardness and non-volatility.

Trends in Magnetism

The magnetization vector of ferromagnetic materials has long been used as a state variable in information processing applications. Indeed, the vast majority of today's digital information is stored in magnetic media. From cassette tapes to modern hard disk drives, the magnetic orientation of domains within magnetic materials have proved to be a remarkably convenient method for data retention. In most magnetic storage devices, an external magnetic field sets

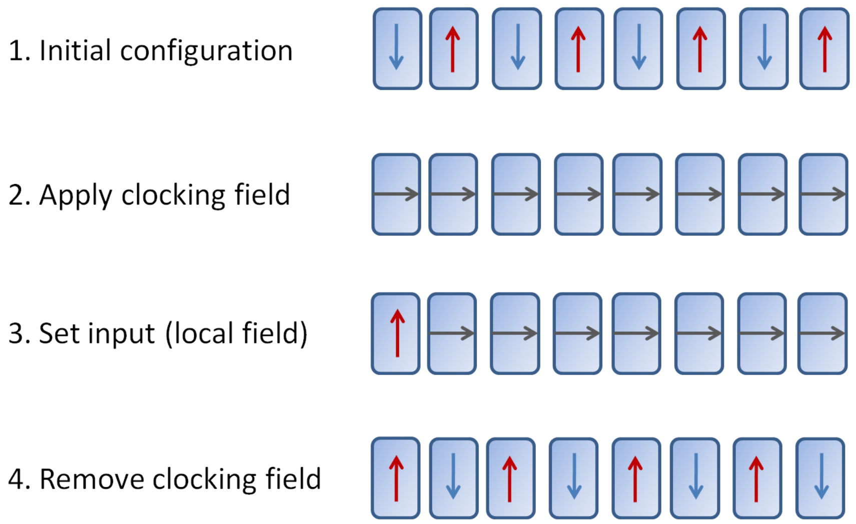

Figure 1.4: Typical clocking procedure used to cycle through computations in NML devices.

the orientation of a magnetic domain and later a sensor reads out the stored information by detecting the stray fields. Magnetic information storage has many desirable attributes: long data retention times, high density, relatively fast read/write times, and low cost.

At nanometer size scales, magnetic materials undergo a striking transition from multi- to single-domain behavior. In a single-domain nanomagnet, the size of an approximately uniformly magnetized region and the size of the nanoparticle itself are equivalent. Each nanomagnet can be assigned a magnetization vector with a constant magnitude that rotates in accordance with equations of precessional motion [8, 9, 10]. The single-domain transition has profound technological implications, including the ability to engineer devices with predictable and repeatable dynamical behavior [11, 12, 13, 14, 15]. In the context of computing devices, this means that new applications possibilities arise that extend beyond the traditional role of magnetic materials to information storage.

One of the earliest proposals for a nanomagnetic computing device was based on an architecture known as quantum cellular automata (QCA) [16]. While the original architecture called for devices comprising quantum dots exchanging electrical charge, it was adapted for devices comprising nanomagnets interacting through dipolar magnetic fields [17, 18, 19, 20]. Each nanomagnet has a single easy axis, typically imparted by the elongated shape, that serves as the information-bearing axis of magnetization, *i.e.* magnetization parallel or antiparallel to this axis represents a binary one or zero, respectively. Chains and arrays of nearly identical nanomagnets are used to propagate and process information, with communication occurring between nearest neighbors. Nearest-neighbor communication is mediated by the dipolar stray fields emanating from each magnet. For example, in a horizontal chain of nanomagnets with vertically oriented easy axes, nearest neighbors preferentially magnetize antiparallel to one another – this is the energetic ground state when the magnetostatic interactions are accounted for. Computing devices built out of interacting nanomagnets

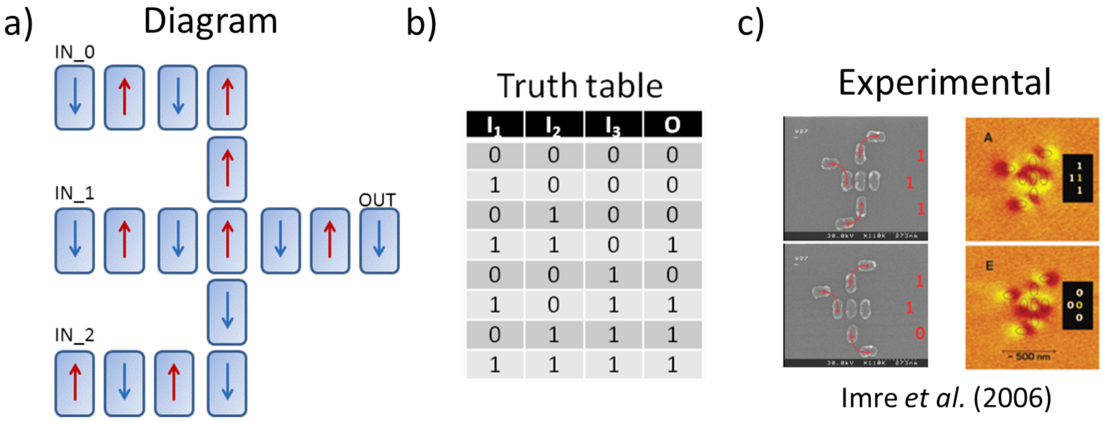

I_1	I_2	I_3	O
0	0	0	0
1	0	0	0
0	1	0	0
1	1	0	1
0	0	1	0
1	0	1	1
0	1	1	1
1	1	1	1

Figure 1.5: (a) Illustration of a majority logic gate and (b) a truth table describing its logical functionality. (c) First experimental demonstration of a majority logic gate [17]

communicating through dipole interactions are referred to as nanomagnetic logic (NML).

In order to cycle through computations in a NML circuit, a clocking procedure is needed. This procedure plays a role analogous to the clocking signal that drives microelectronic logic devices. One possible procedure is outlined in Fig. 1.4. Starting with a chain of nanomagnets in some initial state, a magnetic force (often a magnetic field) referred to as a clocking field is applied to the hard axis of the nanomagnets, causing them to rotate to a logically null magnetization state. Next, the input information for the next logical operation is enforced at the inputs (in Fig. 1.4, the leftmost nanomagnet). A variety of mechanisms for locally applying a magnetic force can be used here [21, 22, 23, 24], several of which will be discussed later on. Finally, the clocking field is removed, and the new output state of the circuit is determined based on the new inputs.

In addition to one-dimensional chains of nanomagnets, NML circuits consist of additional geometric arrangements in two or three dimensions. For example, a vertical chain of nanomagnets provides functionality similar to a horizontal chain of nanomagnets, but the geometry works out such that nearest neighbors preferentially align parallel, rather than antiparallel, to one another. Most important is the majority logic gate (MLG), shown in Fig. 1.5 (a). The MLG consists of a central nanomagnet surrounded by three input nanomagnet chains and a single output nanomagnet chain. The magnetization of the central nanomagnet is determined by the majority vote of the three input chains, with the truth table given in Fig. 1.5 (b). Any boolean logical operation that can be carried out by a traditional microelectronic information processor can also be carried out by an arrangement of MLG's interconnected by one-dimensional chains. The MLG was first demonstrated experimentally by a group of Notre Dame researchers in 2006 [17], with one of their devices shown in Fig. 1.5 (c).

A modification the Notre Dame-style NML architecture based on MLG's was proposed in 2008 by Carlton *et al.* [18]. The modification was designed to engineer around race conditions in MLG's, which refers to a case when a single input signal arrives to the central nanomagnet of a MLG before the other two and causes a logical error. In the modified design, each nanomagnet in the circuit has a secondary easy axis parallel to the direction of the clocking field. As a result, when the clocking field is removed to initiate signal propagation, the nanomagnets linger in the logically null magnetization state until the information from the inputs has sufficient time to propagate through the circuit. A redesigned logic gate with two inputs, called a B-gate, replaces the MLG in this modified architecture and is immune to differences in the time of arrival of each input.

The speed of a NML circuit is dictated by the minimum time it takes to clock the circuit without logical errors occurring. A simple estimate based on the relaxation time of a nanomagnet (the time it takes for a magnet to flip from the hard axis to the easy axis, approximately 100 ps) suggests that the performance limit is set by the relaxation time multiplied by the number of magnets in the critical path of the circuit. Assuming an efficient pipelined architecture with a 10-nanomagnet propagation distance per operation, this yields a maximum operating frequency of about 1 GHz.

Energy dissipation in NML can be sorted into two categories: dissipation in the clocking apparatus and dissipation in the magnets. The portion of the dissipation that occurs in the clocking circuitry, e.g. the resistive heating in wires used to generate an electromagnetic field, is highly technology dependent. One calculation for the power needed to clock an NML circuit using buried wires to generate Oersted fields on-chip at a frequency of 100 MHz estimated three orders of magnitude energy savings relative to conventional microprocessors [25]. However, alternative clocking mechanisms yield very different estimates; in fact, in Chapter 4 we analyze the possibility of NML operation with no external clocking force all. The energy dissipation fundamental to NML occurs within the nanomagnets themselves, an analysis of which is the subject of chapters 1 and 2 of this dissertation.

The Thermodynamic Limits of Computation

One of the intriguing aspects of nanomagnetic computing is that it circumvents the resistive heating mechanism that dominates energy dissipation in conventional digital logic devices. As a result, it is conceivable that nanomagnetic devices can be used to make experimental contact with fundamental limits to energy efficiency in information processors.

The intersection of information and thermodynamics is a unique subfield of physics and engineering that has been extensively studied in theory, but relatively little has been confirmed experimentally. Perhaps the best-known result in the thermodynamic limits of computation is Landauer's principle [26], which states that the minimum energy needed to erase a bit of information is $kT\ln(2)$. This limit applies to any physical system capable of storing a bit of information, regardless of its specific implementation. Derived from the second law of thermodynamics, the limit is rather abstract, a fact that has led to a variety of controversies and objections over the years. However, Landauer's result thus far has weathered the criticism and is broadly accepted by the scientific community.

Landauer's principle serves as a starting point for a large body of theoretical work on the thermodynamic limits of information. Most famously, the notion of reversible computing was explored by Bennett as a means of surmounting the Landauer limit by processing information without any erasure operations [27]. Specific implementations of reversible computers were proposed by Fredkin and Toffoli [28]. In addition, generalized versions of Landauer's principle that apply to quantum information processors and small systems (i.e. systems that do not strictly obey the second law of thermodynamics on short time scales) were derived [29, 30, 31].

Until recently, little experimental work was carried out to corroborate the many theoretical developments in the field. The main reason for this apparent lapse is simply that Landauer's limit is an extremely small quantity of energy, making it very difficult to measure. To illustrate, at room temperature $kT\ln(2)$ of energy dissipation would cause the temperature of 1 kg of water to rise by only about 7×10^{-25} K. Even so, experimental techniques have progressed to the point that such small quantities of energy have become measurable in recent years. In particular, a technique that uses small colloidal particles in externally modulated electrostatic or optical traps to function as a "computer" has been applied to several important experiments. In these experiments, the particle represents information and its position is measured as a function of potential energy, which is modulated by the optical traps. At least three key results have been measured by this technique in the last decade: the Jarzynski equality [32], information to energy conversion [33], and the Landauer limit itself [34].

While experiments using colloidal particles have been fruitful, their most glaring limitation is that such systems do not physically resemble or have the functionality of a microprocessor. They are not integrated devices. As such, there is no clear roadmap for scaling up these experiments to systems that carry out familiar and practical computations. This presents an opportunity in the field that nanomagnetic technologies, which are inherently integrated, can uniquely address.

1.3 Tools and Techniques

The work presented in this dissertation draws heavily from recent advances in nanofabrication, nanocharacterization, and scientific computing methods. In the appendices, several of the tools and techniques that played the most critical role in our investigation are reviewed. Appendix A describes the techniques we used to fabricate nanomagnetic devices. Most of the techniques we used are commonplace in the nanoscience research community. By largely following well-known fabrication procedures, we were able to rapidly build prototype devices and iterate through multiple sample designs. Appendix B describes two characterization techniques that were used to probe the behavior nanomagnetic devices: magneto-optical Kerr effect (MOKE) magnetometry and X-ray magnetic circular dichroism photoelectron emission microscopy (XMCD-PEEM). Both methods have noteworthy strengths and weaknesses. By using them in tandem, we were able to gain new insight into the properties of nanomagnets and nanomagnetic logic devices. Finally, Appendix C describes two scientific computing tools that we used to predict and/or explain the behavior of nanomagnet-based devices. One tool is publicly available software available for use to the magnetism community, and the second is a custom-built micromagnetic simulator.

1.4 Summary

The following dissertation is organized into six chapters that can be broadly classified into two themes. The first theme focuses on the use of nanomagnetic computing elements to experimentally access the thermodynamic limits of computation. Nanomagnetic memory and logic elements provide unique advantages over alternative experimental platforms for probing energy dissipation at the smallest of scales. In simulation and experiment, these advantages are harnessed to help illustrate how earlier theoretical work is manifested in real-world integrated technologies. This subject matter is covered in Chapters 2 and 3.

The second theme focuses on improving the reliability of signal transmission in nanomagnetic computing technologies. We first develop a nuanced understanding of the dynamic processes involved in signal transmission and then propose modifications that improve the reliability of NML. We discover that two modes of signal transmission can occur in NML circuits, one of which is better for energy efficiency and the second of which is better for reliability. For the purposes of designing a circuit that is as reliable as possible, we propose a geometric variant on the conventional nanomagnet shape that enables the second, more reliable mode of signal propagation to occur. This subject matter is covered in chapters 4 through 7.

Chapter 2

Nanomagnetic Logic and the Thermodynamic Limits of Computation

2.1 Landauer's Principle in Nanomagnets

Landauer's Principle was derived originally from the second law of thermodynamics and the observation that an information bearing system has at least two distinguishable states whereas and erased system has only one. Converting an information bearing system into an erased system thus requires a reduction in entropy of at least $k\ln(2)$ (the original system has an entropy of at least $k\ln(2)$ and the final system has an entropy of $k\ln(1) = 0$). The second law of thermodynamics, however, requires that the change in entropy be positive, which implies that the reduction of entropy in the memory element must be balanced by an equivalent or greater increase in entropy of the surrounding environment. If the memory element is coupled to a thermal reservoir, this means that the heat of the reservoir rises by at least $kT\ln(2)$.

While the derivation of the Landauer limit is straightforward, its interpretation – especially in complex computing devices with many interacting bits – is less so. For example, not all computations require the erasure of information, and it has been shown that any computation that requires information erasure can be embedded within one that does not [27, 35]. Moreover, when considering specific physical implementations of memory elements such as CMOS-based memories or magnetic memories, the relevance of Landauer's abstract derivation can become unclear. These considerations point to a need for experiments that shine light on the proper application and meaning of Landauer's principle.

Nanomagnetic memories and logic devices are one class of information processing platforms that have the potential to provide experimental access to the thermodynamic limits of computation. In nanomagnets, electron spin serves the role of the state variable, and the anisotropy and magnetostatic forces define the potential energy landscape of the system.

Nanomagnetic devices provide unique insights into Landauer's principle. Alternative approaches, most prominently the use of colloidal particles in electrostatic or optical traps as memory elements [32, 33, 34], are not integrated and therefore are not analogous to conventional digital logic processors. They are limited to investigating only the simplest manifestations of Landauer's principles that apply to single bit operations rather than combinatorial logic functions. Conventional semiconductor electronics cannot be used to investigate the thermodynamic limits because technology-dependent resistive heat dissipation and the dissipation related to Landauer's limit occur within the same components, making it difficult to decouple them in an experiment. In addition, the potential energies of their two logical states, V_{high} and V_{low}, are different, which presents additional challenges to their efficient operation such as charge leakage.

In summary, the important characteristics of nanomagnetic devices that make them attractive for investigating the thermodynamic limits of computation include:

- Decoupled logic and driving circuitry: External magnetic fields drive passive logic execution components, facilitating sensitive measurements of heat dissipation in logic components
- Integrated: Top down control of magnetic devices of arbitrary complexity is possible
- Practical: Magnetic hard disk drives, magnetic random access memories, and nanomagnetic logic are commercialized or under active research and development

These and other practical considerations, such as the availability of benchmarked simulation software, motivated us to conduct a detailed investigation of the thermodynamic limits of computation in nanomagnetic devices [19].

2.2 Approach

The first step in our investigation was to carry out simulations and analysis to verify the hypothesis that nanomagnetic devices are capable of achieving Landauer efficiency. As in Landauer's original approach, we focus initially on the memory erasure operation, which is the simplest possible non-conservative logical operation. We then build on these results to address more complex logic operations such as the majority logic gate that is central to the nanomagnetic logic architecture.

A nanomagnetic memory consists of a single-domain nanomagnet with an easy axis in the vertical direction along which the magnetization can orient up or down. These two states represent binary one and zero, respectively. The erasure operation, as defined by Landauer, drives the magnet from an initial unknown state in which the magnet is equally likely to be pointed up or down to a final known state in which the magnet is pointed up with unity probability. This behavior can be accomplished by applying external magnetic fields.

The external magnetic fields must be applied in a special procedure subject to the constraint that the magnetization of the magnetic bit cannot undergo an abrupt transition at

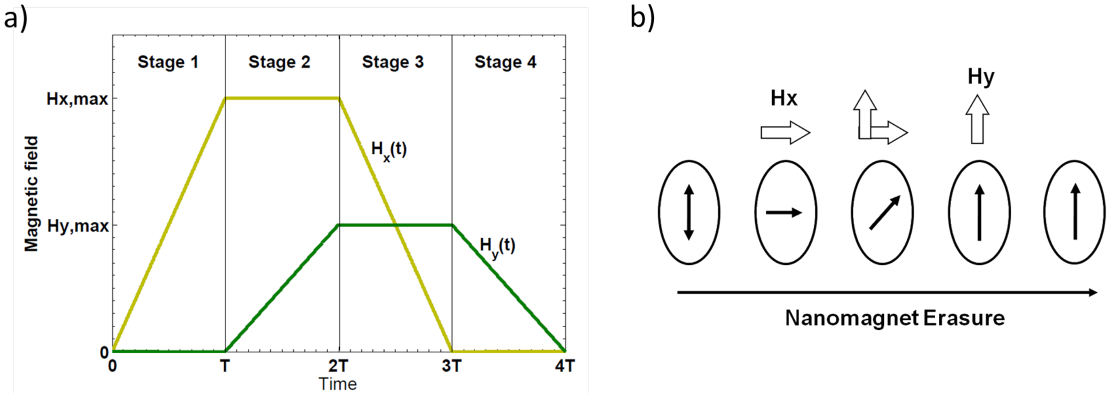

Figure 2.1: Procedure for applying magnetic fields to a nanomagnetic bit that carries out an erasure operation with Landauer efficiency.

any point during the erasure operation. An abrupt transition in the magnetic state causes energy dissipation in excess of the fundamental limits, mediated by the magnetic damping forces. This requirement can be met by ensuring that the magnet is in a state of thermal equlibrium all points during the operation. We therefore came up with the procedure shown in Fig. 2.1 (a) and (b). The procedure involves two magnetic field components, one oriented along the hard axis of the nanomagnet (horizontally) and the other along the easy axis (vertically). The horizontal component of the field serves to remove the anisotropy energy barrier that separates the up and down states of the nanomagnet and is applied first. The vertical component of the field is then ramped up in order to bias the magnet towards the desired final state (up). Finally, the two fields are sequentially removed in order to complete the operation. By inspection of the effect this procedure has on the magnet in Fig. 2.1 (b), we observe that at no point during the operation does the nanomagnetic bit undergo an abrupt tranistion, as required to achieve Landauer efficiency.

Once the procedure for applying magnetic fields is selected, it is necessary to calculate the evolution of the magnetization state of the nanomagnet as it undergoes erasure. This allows us to calculate the potential energy of the particle at all times throughout the operation as this quantity is given by the product of the magnetization and external magnetic field. Ultimately, it allows us to determine the energy dissipated as a result of the erasure operation. We employed two different mathematical approaches for this purpose. The first uses the stochastic Landau-Lifshitz-Gilbert (LLG) equation, which describes the precessional motion of a magnet interacting with a magnetic field and a thermal reservoir. This approach corresponds most closely to the real-world behavior of a nanomagnet; however, it is computationally intensive and requires averaging due to the stochastic component of the equation. The second approach approximates the magnetization vector as a Boltzmann distribution in three dimensions, facilitating fast and accurate calculations without the need for averaging.

Approach 1: LLG Equation We calculated the LLG equation using the finite difference midpoint technique [36]. Both the OOMMF and MATLAB simulation approaches discussed in Appendix C were tested and yielded similar results. The thermal statistics of the MATLAB simulations were verified by simulating the probability density function of the magnetization vector of a nanomagnet with a known energy profile, as described in Ref. [36]. The LLG equation is given by:

$$\frac{d\mathbf{M}}{dt} = -\gamma \mathbf{M} \times (\mathbf{H_{eff}} + \nu \mathbf{H_N}) - \frac{\gamma\alpha}{M_S}\mathbf{M} \times [\mathbf{M} \times (\mathbf{H_{eff}} + \nu \mathbf{H_N})] \tag{2.1}$$

where γ is the gyromagnetic ratio, and α is the Gilbert damping constant. In this equation, the noise term is the random thermal field, $\nu\mathbf{H_N}$, an isotropic white-noise vector whose components are independent Gaussian random variables with variance ν^2. This equation has accurately described many experimental phenomena and is widely accepted to be applicable to real magnetic structures.

For our simulations we selected a field ramp time of 50 ns and temperature of 300 K. The nanomagnets were modeled as circular disks with a diameter of 10 nm and thickness of 2 nm, uniaxial anisotropy energy density of 0.26 eV ($10kT$ at 300 K), saturation magnetization of 800 kA/m, and Gilbert damping constant of 1. All of the selected parameters are consistent with real magnetic materials except for the Gilbert damping constant, which is typically less than 0.1. A damping constant of 1 minimizes the time it takes for the nanomagnet to reach thermal equilibrium; had we instead used a damping constant less than 0.1, the ramp time needed to ensure the validity of the quasi-static approximation would have increased by perhaps an order of magnitude or more. A discussion of the dependence of energy dissipation in nanomagnets on ramp time when the quasi-static approximation does not hold is available in ref. [37].

The output of our simulations can be plotted as two hysteresis curves (magnetization as a function of applied field), one for each component of the magnetic field. The energy dissipation is given by area of the region bounded by the hysteresis curves, equivalent to the integration of the magnetic potential energy of the particle for the duration of the operation. The area of the hysteresis curve can be positive or negative in sign depending on which direction the curve is formed, clockwise or counterclockwise. A negative value implies that the energy flows from the external magnetic field into the nanomagnet during the operation, whereas a positive value implies that energy is returned from the nanomagnet to the external magnetic field. The total energy flow should be negative – more energy must be delivered to the nanomagnet than it returns to the magnetic field.

The resulting hysteresis curves are plotted in Fig. 2.2 (a) and (b). These curves are averaged over 2000 simulations. In half of the simulations, the magnet was initialized in the up state and in half it was initialized down. In all simulations, the final state of the magnet was up. Even though the initial state of the magnet is defined, not unknown, the same procedure for applying magnetic fields is used in both cases. This ensures that no trace of the initial information remains in the system upon completion of the erasure operation. The results of initializing the magnet up or down were the same to within 0.015 kT.

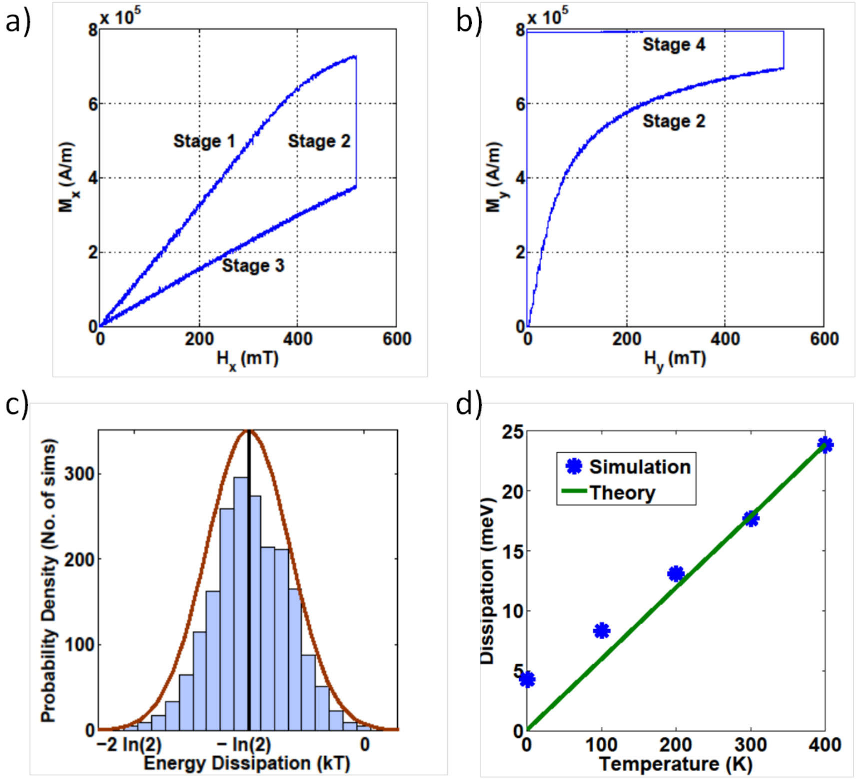

Figure 2.2: (a) X-axis and (b) y-axis hysteresis loops of a nanomagnet during the restore to one operation at 300 K, obtained by solving the stochastic LLG equation. Each point on the curve is the average of 2000 simulations. The total area of the loops is very close to $kT\ln(2)$. Stage numbers correspond to the raising and lowering of external applied fields as described in Fig. 2.1. (c) Histogram of the energy dissipated at 300 K. The envelope curve was obtained using the Boltzmann thermal distribution calculation. (d) Energy dissipation versus temperature. The solid line is the Landauer Limit, $kT\ln(2)$, and the discrete points are the average dissipation over 2000 simulations carried out at each temperature. The simulations deviate from theory at low temperatures because the nanomagnets take longer to reach thermal equilibrium, weakening the quasistatic approximation.

In Fig. 2.2 (c), we show the total area of the hysteresis loops, plotted as a histogram of the area before averaging over all the simulations. The mean energy dissipation was found to be $0.6842kT$, which corresponds to a 95% confidence interval of $0.6740kT$ to $0.6943kT$. These values are in very close agreement with the Landauer limit, $kT\ln(2) = 0.6932kT$. The energy dissipation had no statistically significant dependence on whether the nanomagnets initialized to 'one' or 'zero'; the mean energy dissipation for the separate cases were $0.6809kT$ and $0.6875kT$, respectively. The distribution around the mean is consistent with the generalized formulation of Landauer's principle for small systems given by Dillenschneider *et al.* [31], which states that heat fluctuations at the nanoscale make it possible for individual erasure events to dissipate less than $kT\ln(2)$ even though the average dissipation cannot be more efficient than Landauer's limit. Similar simulations were carried out for a range of temperatures from 0K to 400K to verify the linear dependence of energy dissipation on temperature, plotted in Fig. 2.2 (d).

By inspection of Fig. 2.2, we note that it is possible to traverse the hysteresis loops in the reverse direction in the case that the initial state of the nanomagnet is known to be up. This is accomplished by applying the external magnetic fields as defined in Fig. 2.1 in reverse order. The resulting sign change of $d\mathbf{H}$ when computing the area of the hysteresis loops implies that the reverse erasure operation recovers, rather than dissipates, $kT\ln(2)$. Such reverse operations have been previously considered by Maroney [38] to motivate a more general formulation of Landauer's principle [29] that applies to generic logic operations in addition to the special case of bit erasure.

Boltzmann calculation While the stochastic LLG equation phenomenologically models the dynamics of the nanomagnet during erasure, the average hysteresis loops of many simulations converge to a deterministic result. A faster way to arrive at this deterministic result is to use thermal distribution functions, which can generate accurate hysteresis loops in a single calculation. This approach is valid in the case that the nanomagnet has time to relax to thermal equilibrium at every time step, which holds true for the Landauer erasure when the magnetic fields are applied in a quasi-static manner. Similar to the LLG approach, the output of the calculation is the mean and probability distribution of the energy dissipation. For the case of an angular Boltzmann distribution, we have:

$$P(\theta) = \frac{1}{Z} e^{-\beta E(\theta)} \tag{2.2}$$

where $\beta = \frac{1}{kT}$, Z is the partition function

$$Z = \int_0^\infty e^{-\beta E(\theta)} d\theta \tag{2.3}$$

and $E(\theta)$ is the magnetization energy as a function of angle

$$E(\theta) = K_u V \cos^2\theta - M_S H_x V \cos\theta - M_S H_y V \sin\theta \tag{2.4}$$

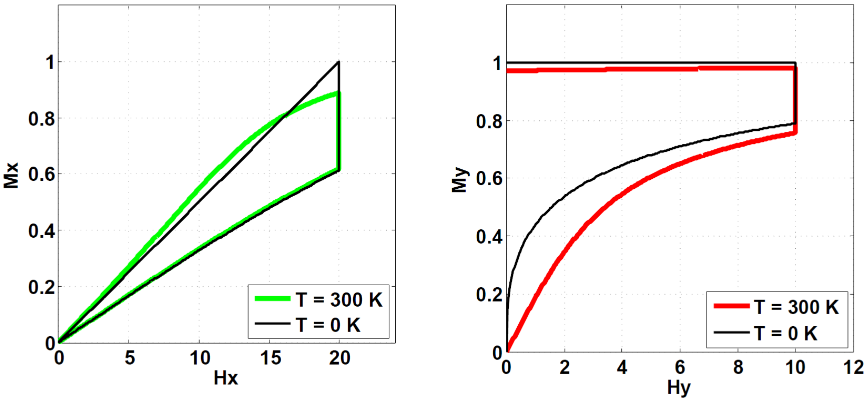

Figure 2.3: (a) X-axis and (b) y-axis hysteresis loops for Landauer erasure of a nanomagnet calculated using the Boltzmann thermal distribution approach. The black curve is calculated with a temperature parameter of 0K and the colored curve at 300 K.

for a single magnetic domain with uniaxial anisotropy energy density K_u. Using the relationships $M_x = M_S \cos(\theta)$ and $M_y = M_S \sin(\theta)$, we integrate over the probability density function to find the average magnetization as a function of $\mathbf{H}$ along the x- and y- axes:

$$\langle M_x(\mathbf{H})\rangle = \frac{M_S}{Z}\int_0^{2\pi} \cos(\theta) e^{-\beta E(\theta)} d\theta \tag{2.5}$$

$$\langle M_y(\mathbf{H})\rangle = \frac{M_S}{Z}\int_0^{2\pi} \sin(\theta) e^{-\beta E(\theta)} d\theta \tag{2.6}$$

To output the correct hysteresis loop for Landauer erasure, the limits of integration for equation (2.6) must be modified during stage 4 of erasure to the upper half angle (0 to π) corresponding to logical ‘one’. This modification arises because the anisotropy energy barrier between ‘one’ and ‘zero’ when H_x is zero is taken to be large enough to prohibit thermal transitions from ‘one’ to ‘zero’. As a result, equation (2.6) must account for the fact that the state of the particle is known to be ‘one’ during stage 4. It is interesting to note that if the limits of integration are not changed during stage 4, implying that the final state of the nanomagnet is unknown, the net area of the hysteresis loops is zero, i.e., no energy is dissipated on average. This could occur physically if the anisotropy barrier is too low or the ramp time is too long to prevent thermal switching as H_y is reduced to zero.

In Fig. 2.3, equations (2.5) and (2.6) are solved numerically and plotted against the applied field along their respective axes, yielding hysteresis loops similar to those obtained using the Landau-Lifshitz-Gilbert equation. For comparison, we also plot the hysteresis loops obtained at T = 0 K, given by the magnetization state of the potential energy minimum at a particular value of $\mathbf{H}$. The combined area of the x- and y- axis hysteresis loops is $0.6932kT$, which is $kT\ln(2)$ to four decimal places. Precision is limited only by the descretization of the numerical integration. This result confirms that energy efficiency approaching the Landauer's limit can be achieved in a nanomagnetic memory under realistic physical conditions.

The hysteresis curves plotted in Fig. 2.3 provide important insight into the physical energy dissipation mechanism during nanomagnet erasure. In particular, the most significant departure between the room temperature and 0K hysteresis loops occurs during stage 2 of erasure, i.e., when H_y ramps from 0 to $H_{y,max}$, which implies that the majority of energy dissipation occurs during this stage. During stage 2, every incremental increase of H_y results in a small shift in the equilibrium probability distribution of the magnetization towards the up state. This shift reduces the stored energy in the magnet due to the magnetostatic energy difference between the up and down states at nonzero H_y. In order for the probability distribution to relax to a lower energy configuration, the magnet must dissipate heat via damped oscillations of the magnetization. The dissipative relaxation cannot be avoided, even in the limit of an infinitely slow ramp rate. The total energy dissipation, which is found by integrating the dissipation as H_y is ramped to its maximum, approaches Landauer's limit, as our calculations confirm. Note that at 0K, the magnetization has zero probability of occupying the high energy 'zero' states for any H_y greater than 0. Therefore, no change in the probability distribution occurs with an incremental increase in H_y, and no energy is dissipated.

2.3 Nanomagnetic Logic

The next step is to expand our analysis of from isolated nanomagnets behaving as memory elements to interacting nanomagnets in an NML circuit. By calculating the relevant hysteresis loops associated with MLG operation, we show that although Landauer efficiency is not achieved when the inputs are reset before the output, dissipationless operation is possible when the output is reset before the inputs. This is an example of Bennett clocking and is a promising route for performing computations at the ultimate efficiency limits. Note that while the following analysis is for a single MLG, the approach can be scaled to a nanomagnetic logic circuit of arbitrary complexity.

Examples of reversible and irreversible computation cycles are shown in Fig. 2.4 (a) for a nanomagnetic logic circuit containing a single MLG. Both cycles begin and end in the same state, in which all nanomagnets in the circuit are forced into their null (hard-axis) state by a magnetic field. Logic execution is carried out by slowly removing the hard-axis magnetic field after setting the inputs using localized magnetic fields. Magnetostatic coupling between nanomagnets causes the final state of the circuit to be determined by the state of the three inputs. The output (rightmost) nanomagnet contains the result of the majority logic calculation and can be detected electronically or passed on to another portion of the circuit. Further details on signal propagation and thermal effects in nanomagnetic logic circuits can be found in [39].

To complete the computation cycle, the MLG circuit is reset to its null state by restoring

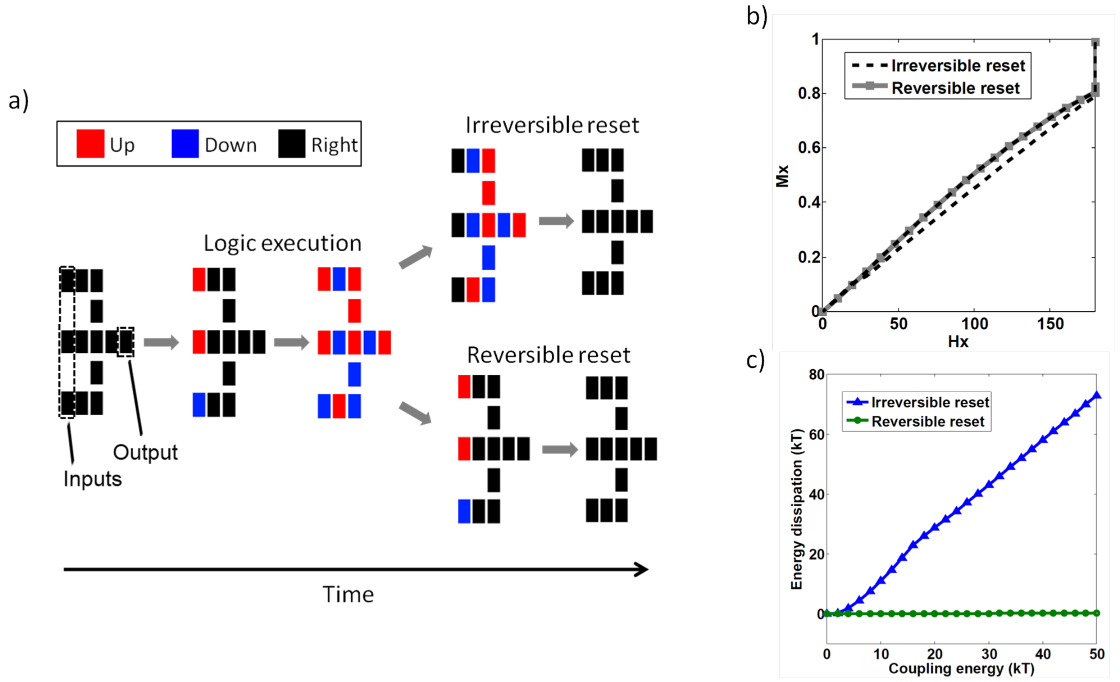

Figure 2.4: (a) Two possible computation cycles for a nanomagnetic logic circuit containing a single MLG and (b),(c) their corresponding hysteresis loops and energy dissipation. In (a), the circuit computes the majority vote of three inputs (leftmost nanomagnets) and passes the result to an output (rightmost nanomagnet). After logic execution, the circuit is reset to its initial state irreversibly (top branch) or reversibly (lower branch). In (b), the hysteresis loops for the magnetic field applied to the nanomagnets to the right of the inputs is plotted. The nearest neighbor coupling energy was set to 50 kT in this simulation. In (c), the energy dissipation of both computation cycles is plotted as a function of the nearest neighbor coupling energy between nanomagnets.

the hard axis field. In the irreversible cycle, the inputs are reset before the outputs, as is characteristic of information propagation in the forward direction. A pipelined nanomagnetic logic circuit must be reset irreversibly because the inputs of each stage are the outputs of a previous stage that must be reset first. Alternatively, it is possible to reset the circuit reversibly, i.e., the outputs are reset before the inputs. Past experimental implementations of the MLG have (perhaps unintentially) been operated reversibly because the inputs are hard-coded into the circuit and persist before and after the application of the hard-axis field [17].

To calculate the average energy dissipation for both cases, we employ the thermal equilibrium calculations described in the previous section. The hysteresis loops we obtain correspond to the X- and Y- axis fields applied locally to each input and the X-axis field driving the remainder of the gate (all nanomagnets to the right of the inputs). Each of the eight possible input permutations are calculated separately and averaged. In Fig. 2.4 (b), the average hysteresis loops for the X-axis magnetic field applied to the magnets to the right of the inputs are plotted for the irreversible and reversible cases. In the reversible cycle (red line), no hysteresis is observed, indicating zero energy dissipation. This result can be attributed to the temporal symmetry of the reversible cycle; because the computation proceeds in the same manner forwards and backwards, all of the hysteresis loops exactly retrace their path as the applied magnetic fields are lowered and raised. On the other hand, there is no such symmetry in the irreversible case. As a result, the hysteresis loop (dotted line in Fig. 2.4 (b)) opens and the energy dissipation is nonzero. The amount of energy dissipation is a function of the magnetostatic coupling energy, as observed in Fig. 2.4 (c). The coupling-energy dependent dissipation mechanism for irreversible nanomagnet operations has been discussed previously in ref. [37].

Note that there is a difference between the reversible MLG operation considered here and conservative logic schemes, which are also logically reversible but do not require the inputs to be stored for the duration of the computation [28]. A nanomagnet-based implementation of a conservative logic gate, while desirable, has not been demonstrated at this time.

2.4 Discussion

Nanomagnetic logic typifies much of the theoretical work that has been carried out to date on the thermodynamic limits of computation. We have found that the combined area of the hysteresis loops of a nanomagnet during bit erasure approaches Landauer's thermodynamic limit of $kT\ln(2)$ with high precision in the damped switching mode. In addition, we showed that nanomagnets behave according to generalized formulations of Landauer's principle that hold for small systems and generic logic operations. Finally, we calculated the energy dissipation in a nanomagnetic majority logic gate, finding that reversible, dissipationless computation can be achieved when the outputs are reset before the inputs. We conclude that nanomagnetism is an attractive platform for experimentally investigating the thermodynamics limits of computation and suggest possible applications for this work in energy-efficient magnetic memory technologies and write/erase procedures thereof. In the next chapter, we carry out experimental studies to verify the simulation work described in this chapter.

Chapter 3

Magneto-optical investigation of Landauer erasure in nanomagnets

3.1 Experimental Verification of Landauer Erasure Simulations

The simulation results discussed in the previous chapter laid the theoretical foundation for investigating the thermodynamic limits of computation in nanomagnetic devices. The next step is to demonstrate that it is feasible to conduct experiments with such devices. The requirement is that we must be able to measure the energy dissipation in magnetic devices with sufficient resolution to distinguish the quantity $kT\ln(2)$ of energy.

This chapter focuses on the measurement of Landauer efficiency during the nanomagnet erasure operation. While recent experiments by Berút *et al.* [34] have previously verified Landauer's Limit experimentally, there are still compelling reasons to carry out our investigation. First, there is fundamental and practical interest from the magnetism community to reproduce the verification of Landauer's Limit in nanomagnetic devices. Unlike the memory systems studied in earlier experiments, magnetic memory and storage devices have a multitude of commercial applications. Discoveries that improve their energy efficiency are both exciting and potentially commercially valuable. Second, verifying Landauer's Limit in nanomagnetic devices is a gateway experiment to the exploration of the thermodynamic limits of computation in more complex digital logic circuits. Whereas earlier experimental platforms have limited capabilities beyond the manipulation of a single bit, NML can be scaled to perform computations of arbitrary size and complexity. Verification of Landauer's Limit in nanomagnetic devices sets the stage for these types of experiments.

3.2 Survey of Measurement Techniques

The measurement of $kT\ln(2)$ of energy requires a technique that has extremely high sensitivity. Both the precision and accuracy of the technique must be tuned to give the highest possible measurement resolution. One conceivable approach to this experiment, to directly measure a change in temperature caused by the erasure of a nanomagnet, was not pursued because it appears unlikely that it can achieve the necessary precision. Instead, we focused on measuring the magnetization of a nanomagnet as a function of applied magnetic fields in a manner similar to the approach taken in our simulations in Chapter 2. The area of the M-H curves we measure is equivalent to the energy dissipation. This approach also bears similarity to the technique used by Berút *et al.* in which the potential energy of a particle was measured as a function of time and integrated rather than attempting a more direct measurement of heat dissipation.

Many methods exist for measuring the magnetic moment of nanomagnets. Our experimental approach was to use the MOKE technique described in Appendix B, but other options were considered at different points in the investigation. The strengths and weaknesses of some of these techniques are described here.

Vibrating Sample Magnetometry In vibrating sample magnetometry (VSM), the magnetic moment of a sample is measured by detecting the amount of electrical current it induces when it vibrates between two conductive coils. A lock-in technique is used to compare the detected electrical current to the vibration frequency of the sample stage. This technique can offer sensitivity to samples with magnetic moments as small as 10^{-7} emu. By comparison, the magnetic moment of a single domain permalloy nanomagnet is on the order of 10^{-13} emu.

While VSM is most often used to study continuous magnetic films that have a relatively large magnetic moment, it is conceivable to use VSM to measure hysteresis in large arrays of nanomagnets. In order to make high resolution measurements using this technique, the size of the nanomagnet array must be large enough to boost the signal far above the instrument's sensitivity. Approximately 10^8 nanomagnets would be needed. Assuming 1 μm spacing between magnets, this corresponds to a 1 cm^2 array. While large, such a fabrication effort is feasible. However, we did not pursue this option, in part due to the inherent inflexibility associated with fabricating and testing samples that require unusually long electron beam write times, but also due to lack of convenient access to a VSM tool with the necessary sensitivity.

SQUID Magnetometry A magnetometer based on a superconducting quantum interference device (SQUID) can be used to achieve sensitivity higher than the VSM magnetometer. The magnetic moment of a sample is measured by detecting the change in the order parameter of a superconducting loop when a magnetic flux passes through it. The higher sensitivity of a SQUID magnetometer relative to a VSM could permit the detection of a magnetic moment from smaller arrays of nanomagnets. Nano-SQUID magnetometers that are fabricated

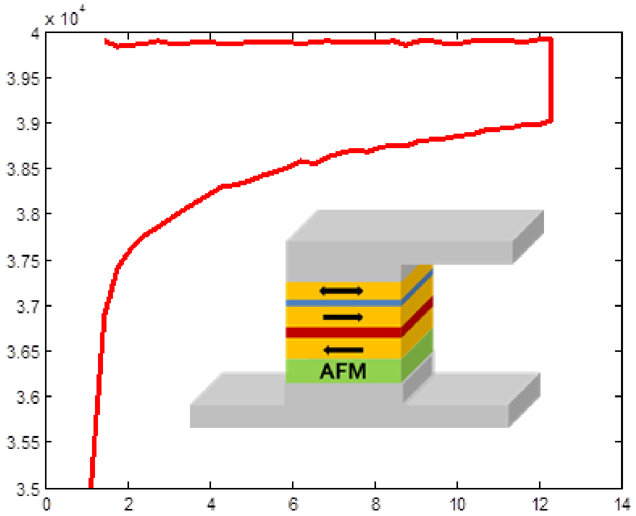

Figure 3.1: Hysteresis curves measured in a TMR sensor during Landauer erasure (y-axis only). Inset shows the layer structure of the TMR device.

on-chip could even detect changes in the magnetization of a single nanomagnet. However, due to the need for highly specialized tools and cryogenic temperatures, we opted not to pursue this technique.

Magnetic Tunnel Junction The magnetization of a single nanomagnet can be detected by passing a spin polarized current through it and measuring the resistance. If the magnetization is parallel to the spin polarization of the current, the resistance is relatively low, and if it is antiparallel the resistance is high – this effect is known as magnetoresistance. Values of magnetoresistance (the resistance ratio between the parallel and antiparallel states) as high as 600% have been measured when spin polarized current is injected into the magnet through a MgO tunnel barrier [22, 23], permitting high sensitivity measurements. This device is called a magnetic tunnel junction (MTJ) and consists of a pinned reference magnetic layer on one side of the tunnel barrier and a free magnetic layer on the other.

Working with collaborators at IBM, we fabricated MTJ devices in which the free layer was a single domain permalloy nanomagnet with an ellipsoidal shape. We then probed the resistance of the devices by applying a small test current and measuring the voltage across the junction as a function of the applied magnetic field. The applied magnetic fields were the same as the protocol for Landauer erasure described in the previous chapter. Using this approach, we were able to measure hysteresis curves in units of resistance as a function of applied magnetic field, as shown in Fig. 3.1. We note qualitative similarities between the experimental data and the simulation results of the previous chapter.

In spite of the potential of an MTJ-based approach to achieve highly sensitive measurements, a number of challenges would have to be overcome to successfully verify the Landauer limit using this technique. First, a reliable method for converting the measured resistance to magnetization, as is required for using hysteresis curves to calculate energy, would need to be developed. A simple calculation based on the volume and saturation magnetization of a nanomagnet is not sufficiently accurate if those values come from the design specification rather than the characterization of the as-fabricated sample. Second, the robustness of the devices needs to be improved. Calculating Landauer efficiency requires performing multiple measurements of a single device, but many of the devices we tested became open or short circuits after one or two measurements. Finally, we need to develop a method for measuring both the x- and y-axis hysteresis properties of a magnet – an MTJ typically only has one axis of sensitivity. These challenges have not been overcome at this time and there is no obvious roadmap to a resolution, so an alternative approach is needed.

3.3 MOKE Measurement of Landauer Erasure

One measurement technique that has the potential to overcome many of the challenges faced by the alternate methods described in the previous section is MOKE, which is discussed in detail in Appendix B. Using MOKE, it is possible to measure both the x- and y-axis hysteresis curves of small arrays of nanomagnets with very high sensitivity. Because a MOKE apparatus is relatively simple to customize, we have broad control over the experimental conditions such as the sample temperature and the orientation of the magnetic fields. These factors led us to pursue the experimental verification of Landauer's Principle using MOKE.

One drawback of MOKE relative to other measurement techniques is that its signal to noise ratio tends to be comparatively low when characterizing nanostructures. Our first step in the investigation was to tune up our apparatus to maximize the signal to noise ratio. A number of actions were taken to improve the apparatus, which included:

- Mechanically stabilizing optical components by re-mounting to sturdier bases
- Increasing laser power from 0.15 mW to 8 mW
- Developing an alignment procedure for obtaining precisely p-polarized light from the first polarizer
- Optimizing the density of the nanomagnet array to maximize fill factor without introducing unwanted dipole interactions
- Reducing the cutoff frequency of the input filter of the LIA to eliminate high frequency noise
- Modifying electrical circuitry to simultaneously read magnetic field and LIA voltage values

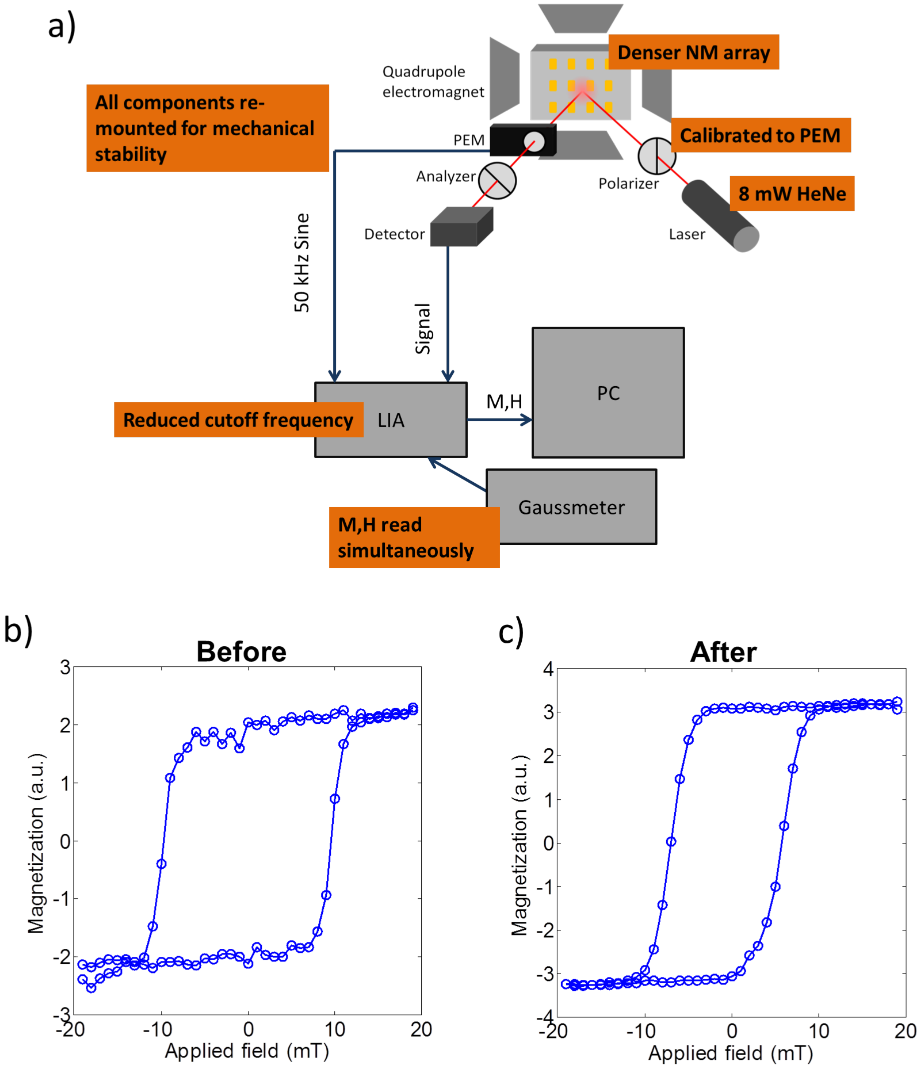

Figure 3.2: (a)Labeled illustration indicating modifications to MOKE apparatus to improve signal to noise ratio. (b) and (c) plot hysteresis loops measured before and after modifying the MOKE apparatus.

These improvements are illustrated in Fig. 3.2 (a). In (b) and (c), we compare hysteresis loops obtained before and after tuning the MOKE apparatus and verify a strong reduction in noise as a result of the changes.

In addition to reducing high frequency noise, low frequency drift had to be controlled in order to improve the sensitivity of our measurements. Low frequency drift may arise from changes in ambient conditions, such as temperature fluctuations, that affect the optical response of polarization components. Such drift has a characteristic time dependence on the order of tens of seconds and limits our ability to improve our signal to noise ratio through

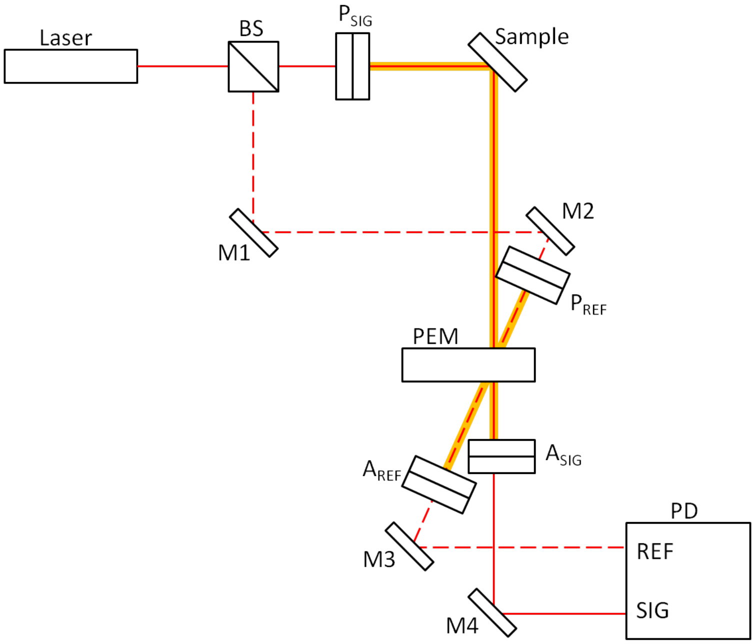

Figure 3.3: Diagram of MOKE apparatus employing drift-reduction techniques including beam referencing and reduction of optical componentents in polarization-sensitive portion of the beam path. The dashed red line is the reference beam path, and the highlighted portions of the beams are the polarization sensitive portions of the beam (i.e. between the polarizer and analyzer).

averaging.

Several measures were taken to reduce drift in our experiment. First, we reduced the number of optical components in the polarization-sensitive portion of the optical path to only essential components i.e. polarizers, the sample, and the PEM. Lenses and mirrors used in other experiments were removed from the setup. Because the diameter of the beam emitted by the laser is approximately the same as the width of the nanomagnet arrays (1 mm), focusing the light onto the sample was not an essential step and could be eliminated entirely. Mirrors, needed to direct the beam, were positioned outside of the polarization sensitive path, as shown in Fig. 3.3 (the polarization-sensitive portion of the optical path is highlighted).

Second, we employ a beam referencing technique that makes use of the auto-balancing feature of the Nirvana photodetector, also shown in Fig. 3.3. A reference beam is split from the signal path using a beamsplitter and directed through the PEM, passing through the PEM optic at the same position as the signal beam. Both the reference and signal beams are detected by the Nirvana photodetector. The output voltage is proportional to $P_{SIG} - g \times P_{REF}$, where g is a factor that is dynamically adjusted such that the DC output voltage is zero. Using this approach, the AC output voltage is relatively insensitive to drift in the intensity of the laser and drift in the modulation amplitude of the PEM, as they affect both P_{SIG} and P_{REF} in equal proportions. To maximize the benefit of this approach, care must be taken to adjust the reference beam polarizer, analyzer and mirrors such that both the DC and AC output voltages of the photodetector are close to zero. We accomplished this by using an oscilloscope to measure the AC output waveform and adjusting the polarization optics of the reference beam until maximum cancellation occurred.

In order to make accurate comparisons between hysteresis curves measured at different sample temperatures, we needed to reduce the number of adjustments to the MOKE apparatus between temperature changes. Typically, the Hall sensor was physically rotated between measurements to allow us to accurately set both the X and Y axis magnetic fields. The motion of the Hall sensor led to small changes in the signal path, causing the measured hysteresis curves to shift slightly between measurements. To resolve this issue, we positioned the Hall sensor such that its two axes of sensitivity aligned with the X- and Y- axes, allowing simultaneous measurement of the two magnetic field components and eliminating the need to move the sensor between measurements. This was found to significantly improve the consistency of measurements at different sample temperatures. After this improvement, the only mechanical adjustment between measurements was to M4 in Fig. 3.3 to redirect the signal beam onto the photodiode, as the beam unavoidably shifts when the sample temperature changes.

Our next step was to proceed with the measurement of Landauer erasure in a controlled manner using the improved MOKE apparatus. The experiment consists of several steps, the first of which is to fabricate nanomagnet arrays of nanomagnets that can be probed optically. The sample we fabricated contained arrays of magnets with a variety of different sizes and intermagnet spacings. The goal was to find an array of magnets that were large and closely packed enough to give a high fill factor and therefore a robust MOKE signal. At the same time, smaller magnets interact more strongly with the thermal bath, leading to more measurable changes in hysteresis curves during Landauer erasure, and widely spaced magnets are less likely to interact through stray dipole fields. We found the optimal array to consist of nanomagnets with dimensions of about 80 nm x 100 nm in plane and 10 nm thickness and an intermagnet spacing of 500 nm. An example of an array we fabricated is shown in Fig. 3.4. A hexagonal packing scheme was adopted to maximize the fill factor without reducing the intermagnet spacing.

We then determined the average magnetic moment of the nanomagnets in the array. This step was needed to calibrate the y-axis of the hysteresis plot to ensure that the area of the curves was in the desired units of energy. We needed to quantify the magnetic moment experimentally because the simpler approach, to make a calculation based on the literature value of the magnetization of a permalloy magnet with a particular size, would only yield an approximate value. As we are making a precision measurement, such an approximation is not acceptable.

The approach we use to calculate the magnetic moments of the nanomagnets involves measuring the coercivity of the nanomagnets as a function of temperature. The coercive field is measured along the nanomagnet easy axis. We then determine the fitting parameters

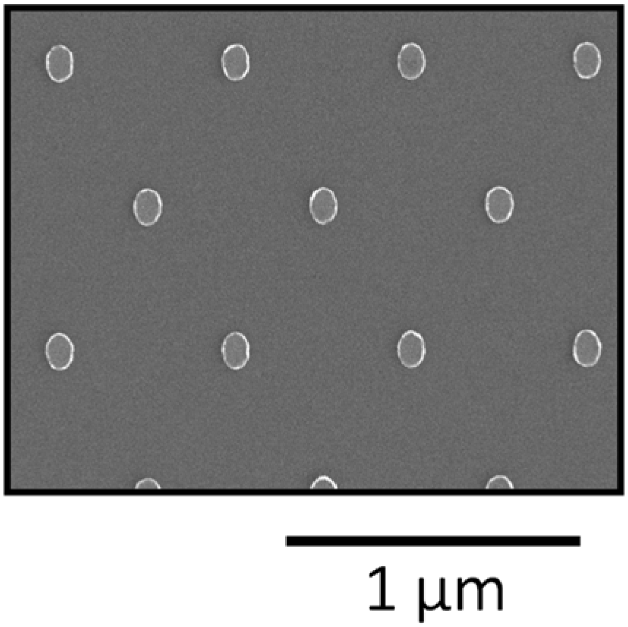

Figure 3.4: Scanning electron micrograph of a typical array of nanomagnets measured by MOKE.

for this function using the Sharrock equation [40]. This equation is given by:

$$H_c = H_0 \left(1 - \left(\frac{k_B T}{\Delta E_0} \ln\left(\frac{f_0 t_0}{\ln(2)}\right)\right)^{1/n}\right) \tag{3.1}$$

Where H_c and T are the measured coercive field and temperature, f_0, t_0 k_B and n are constants, and H_0 and ΔE_0 are the fitted parameters. H_0 is the projected coercive field at 0 K temperature and ΔE_0 is the anisotropy energy barrier of the nanomagnet. The significance of these two parameters is that they are related to the magnetic moment of the nanomagnets by:

$$\mu = M_S V = \frac{2\Delta E_0}{H_0} \tag{3.2}$$

Where M_S and V are the saturation magnetization and volume of the nanomagnets, respectively. As a result, we are able to experimentally determine the scaling factor that relates the MOKE voltage to the magnetization of the nanomagnets using the Sharrock equation fitted to the H_c-T curve.

We applied this technique to a sample similar to the one shown in Fig. 3.4. The sample temperature was varied between 300 K and 400 K in steps of 20 K. The sample was in ambient conditions during the measurement, so we could not reduce the temperature below room temperature due to condensation forming and blocking optical access to the nanomagnet array. At each temperature, we measured hysteresis curves along the easy axis of the

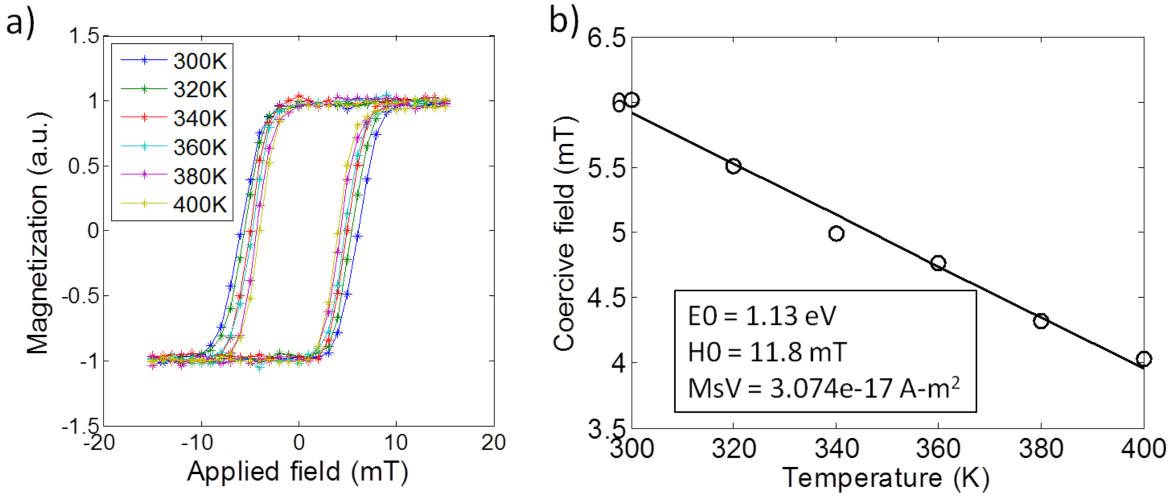

Figure 3.5: (a) Hysteresis curves of an array of nanomagnets measured at varying sample temperatures. (b) Coercive field of an array of nanomagnets as a function of temperature. Inset indicates axis along which hysteresis was measured by MOKE.

magnets, averaging the curves for ten minutes. These results are plotted in Fige. 3.5 (a). The coercive field was extracted from these curves and plotted as a function of temperature, shown in Fig. 3.5 (b). Both the experimental data (open circles) and fitted curve based on the Sharrock equation (solid line) are plotted. The resulting fitted parameters are $H_0 = 11.8$ mT, $\Delta E_0 = 1.13$ eV, and $M_S V = 3.074 \times 10^{-17}$ A·m^2.

Once nanomagnet arrays were fabricated and characterized, we were able to proceed with measuring the hysteresis curves corresponding to the four stages of Landauer erasure outlined in Chapter 2. The first step in the experiment is to precisely determine the orientation of the easy and hard axes of the sample – aligning the magnetic fields to the easy or hard axes of the nanomagnets by eye is not sufficiently precise to achieve Landauer efficiency. The alignment is done by determining the angle at which the MFMA signal of the nanomagnets reaches a maximum. The MFMA measurement is carried out using the technique described in Appendix B and in Ref. [41]. The maximum MFMA signal occurs exactly when the direction of MOKE sensitivity is along the easy axis of the nanomagnets. The sample is then rotated by 90° to achieve sensitivity along the hard axis of the nanomagnets.

Another important step in setting up the experiment is to demagnetize the poles of the quadrupole electromagnet to ensure that the only magnetic fields exerted on the sample are the ones prescribed by the erasure protocol. Any stray magnetic fields – for example, a static field oriented along the hard axis of the nanomagnets while measuring the hysteresis curve along the easy axis – alters the behavior of the nanomagnets and adds a systematic error to the calculation of energy dissipation. To demagnetize the poles of the electromagnet along a particular axis, we applied an oscillating magnetic field starting from a large amplitude and decaying until the amplitude reached zero. This procedure was carried out before every measurement in which the magnetic field along one axis was required to be nulled.

Measuring Landauer efficiency in nanomagnets requires four curves to be measured, two along the hard axis and two along the easy axis of the nanomagnet. In reality, eight curves are needed to fully close both the x- and y-axis hysteresis loops, but four of those curves do not vary in the magnetic field dimension, *i.e.* they appear as vertical lines in the hysteresis curve. These curves have no impact the overall energy dissipation and were therefore not measured. The four relevant curves were measured by sweeping the magnetic field along the axis of MOKE sensitivity while holding the field fixed in the perpendicular direction. The four permutations of sensitivity axis and perpendicular field strength that were measured are:

1. HA, $H_\perp = 0$ mT
2. EA, $H_\perp = 11$ mT
3. HA, $H_\perp = 5$ mT
4. EA, $H_\perp = 0$ mT

where HA and EA refer to MOKE sensitivity along the hard axis and easy axis of the nanomagnets, respectively, and $H_\perp$ is the static field applied in the direction orthogonal to the MOKE sensitivity.

The strength of the perpendicular applied field during stage 2 was chosen to be large enough to fully saturate the nanomagnets along their hard axis. In early experiments, this value was determined by performing an MFMA measurement of susceptibility as a function of applied field and finding the field at which peak susceptibility occurred (see Appendix B). However, the MFMA does not account for variations among the saturation fields the nanomagnets. Nanomagnets with saturation fields greater than the strength of the perpendicular magnetic field exhibit hysteresis during stage 2, dissipating energy in excess of the Landauer limit. To account for these variations, in the current experiment we selected the strength of the perpendicular field by inspection of Fig. 3.5 (a). We selected a field strength large enough to fully saturate the magnets in a given direction at all temperatures, in this case about 11 mT.

To measure each of the four curves, we first set the orthogonal magnetic field and then swept the component of the field along the axis of MOKE sensitivity at 50 mHz. We then averaged the MOKE signal as a function of applied magnetic field for ten minutes per curve. Finally, we repeated the measurement over a range of sample temperatures from 300 K to 400 K in increments of 20 K. We waited 5 minutes between temperatures for the sample temperature to settle. We measured the two Y-axis hysteresis curves while increasing temperature from 300 K to 400 K, then we rotated the sample 90 degrees and measured the X-axis hysteresis curves while decreasing the temperature. It was necessary to split up the measurement in this manner because if we had mechanically rotated the sample at each temperature, the measurement would have been impacted by undesired changes in the position of the sample.

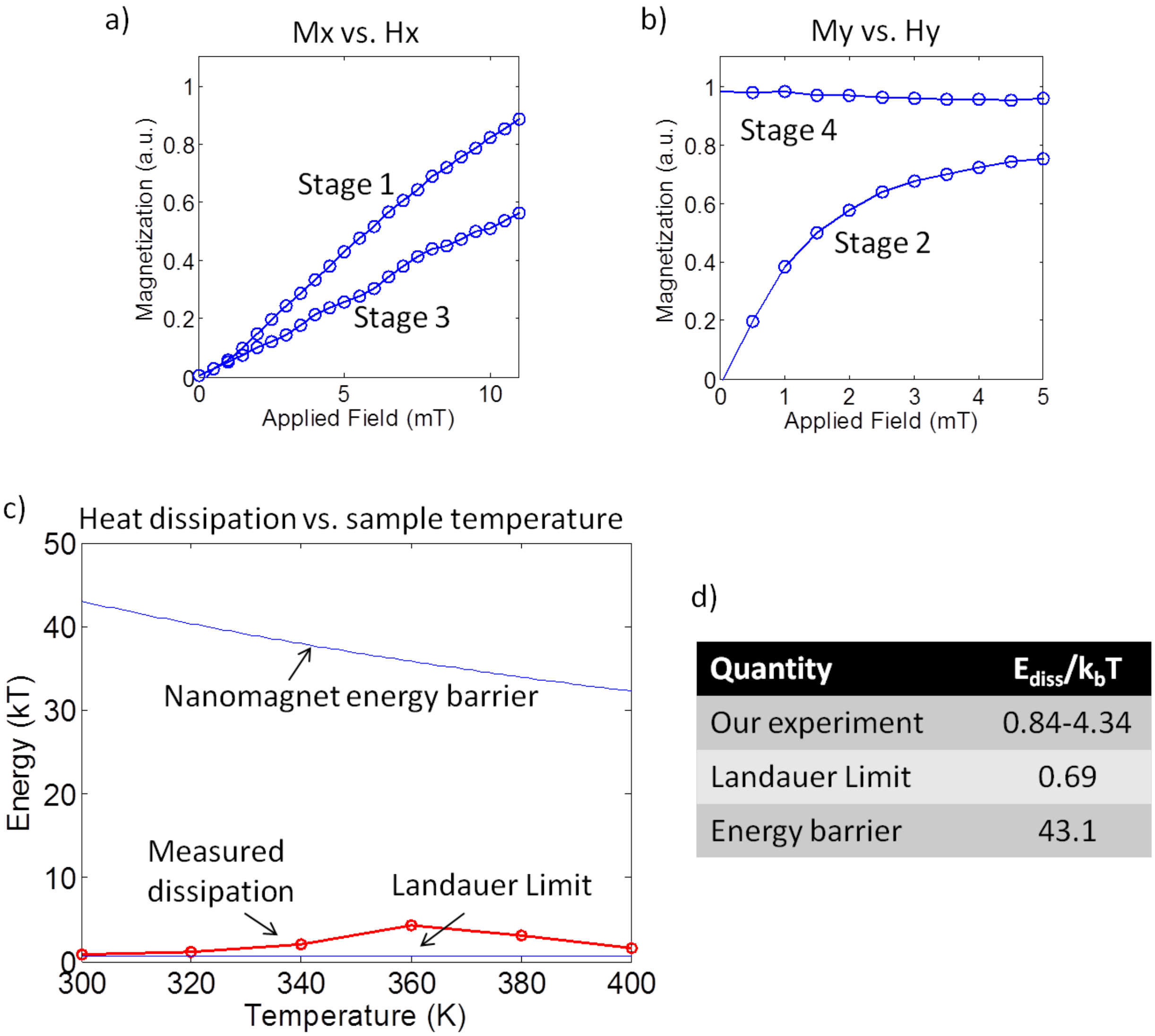

Quantity	E_{diss}/k_bT
Our experiment	0.84-4.34
Landauer Limit	0.69
Energy barrier	43.1

Figure 3.6: (a) X-axis and (b) y-axis hysteresis curves measured by MOKE technique. (c) Plot of energy dissipation as a function of temperature and (d) tabulated results for quantitative comparison.

Data processing was carried out in MATLAB. The data output by the MOKE apparatus was contained in a table comprising pairs of magnetic field (B) and MOKE signal (M) values. First, we filtered the M and B data using a high-pass filter with the cutoff frequency parameter set to 0.00001 (a very low cutoff frequency) to reduce the effect of drift during the measurement. This was followed by a low pass filter with a cutoff frequency parameter set to 20, which implements a moving average with a window size of 20 data points. The B data was further processed by identifying regions increasing and decreasing B during the magnetic field sweep by taking the difference between each pair of neighboring points. If a systematic offset was detected in the B data, we shifted the data by an empirically determined constant factor to cancel out the offset. For example, if the X-axis of the Hall sensor picks up any of the orthogonal Y-axis magnetic field during stages 2 and 3 of the measurements, it results in a systematic offset. In the data set used in Fig. 3.6, an offset of 1 mT was found during stages 2 and 3 of the measurements. After filtering and accounting for systematic offsets, we quantized the B data by snapping each point to the nearest 0.5 mT.

Turning to the M data, we binned and averaged all M corresponding to a given value of B, separated depending on whether the field was increasing or decreasing. Next, we identified the maximum and minimum of the MOKE signal and scaled the curves such that the maximum corresponded to positive saturation magnetization and the minimum corresponded to negative saturation magnetization, the saturation magnetization being given by the calibration measurement in Fig. 3.5. The presence of an orthogonal (y-oriented) magnetic field precluded us from fully saturating the nanomagnets along the axis of sensitivity, so the maximum and minimum MOKE signals for stage 1 and 4 of the measurement were also used to scale the MOKE signals for stage 3 and 2, respectively. The nanomagnets were considered saturated when the strength of the magnetic field was greater than 10 mT. After scaling, we plotted the hysteresis curves and calculated their area and energy dissipation as a function of temperature.

In Fig. 3.6, we show the results of the experiment. Plots (a) and (b) are examples of hysteresis curves measured along the x- and y-axis of the nanomagnet. Qualitatively, we note a strong similarity between the measured hysteresis curves and the simulated hysteresis curves from Chapter 2. Quantitavely, we found that the energy dissipation was a relatively noisy function of temperature with a range of 0.84 kT to 4.34 kT. For comparison, the Landauer Limit is $kT\ln(2)$, or 0.69 kT and the energy barrier height of the nanomagnet, calculated by converting 1.13 eV to units of kT, was 43.1 kT at 300K. This comparison is plotted and tabulated in Fig. 3.6 (c) and (d). We are able to conclude from this data that it is possible to erase a nanomagnet with an energy dissipation significantly lower than the anisotropy energy barrier of the nanomagnet. At the same time, our results are qualitatively consistent with the Landauer Limit, and future work is needed to further address the systematic and random error observed in our experiment.

3.4 Discussion

In an effort to explore the unique capability of NML to make experimental contact with the thermodynamic limits of computation, we carried out measurements of energy dissipation during Landauer erasure of nanomagnets using a MOKE technique. Our objective was to gather data that qualitatively and quantitatively matched the simulation data in Chapter 2. To do so, we first set out to tune the MOKE apparatus to achieve the necessary noise levels for precision measurement of hysteresis curves. Ultimately, we were able to achieve noise levels more than 25 times smaller than the Landauer Limit itself, which is sufficient to meaningfully compare measured energy dissipation with theoretical values.

Outside of instrument noise, there are other nonidealities that have the potential to add systematic error to our experiments. Factors that may be of concern include deviations from uniform magnetization within individual nanomagnets, variations in size and shape among nanomagnets, and changes in nanomagnet material properties with temperature. For example, nanomagnets that are tilted with respect to the vertical axis may exhibit hysteresis when a horizontal magnetic field is applied to them, e.g., during stage 1 of Landauer erasure. The presence of hysteresis results in systematically dissipating energy in excess of the Landauer limit, yet it is unavoidable due to lithographic limitations. The amount of hysteresis is dependent on both the tilt angle and the ramp rate of the magnetic field, with slower ramp rates leading to reduced hysteresis by allowing the magnets to remain closer to thermal equilibrium. The resulting change the shape of the X-axis hysteresis curves is expected to be small but has been observed in simulations and some measurements, lending support to the hypothesis that random tilt among nanomagnets results in at least a portion of the observed systematic error.

Another source of systematic error in our experiment may have been the selection of a perpendicular field strength during stage 2 of the erasure operation that was not sufficiently strong to saturate the nanomagnets along their hard axis. In a nanomagnet with uniaxial anisotropy, saturation occurs when the field strength along the hard axis is equal to twice the coercive field. The coercive field of the magnets as a function of temperature is plotted in Fig. 3.5 (b). At low temperatures e.g. 300 K, the selected field strength of 11 mT is less than twice the coercive field, whereas at higher temperatures e.g. 400 K the selected field strength is greater than twice the coercive field. This observation provides an explanation for the discontinuity in the experimental data shown in Fig. 3.6 (c) at 360 K, which appears to be close to where the transition between not-fully-saturated and fully-saturated occurs. In future experiments, it may be useful to apply a stronger perpendicular field during stage 2. The disadvantage of using a stronger field is that the field sweep must cover a wider range, resulting in a lower integration time per data point.

While we did our best to mitigate noise and error sources through careful design of the sample and the experimental procedure, there remains the possibility that these error sources added a systematic bias to our results. Hence, we refrain for now from making strong claims about having quantitatively observed a match between experimental data and theoretical predictions. The next phase of the investigation – assuming the precision and accuracy of the MOKE technique reach desired levels – includes first and foremost expanding from the analysis of single-bit operations to multi-bit logic operations. This is the key scientific value that the nanomagnet-based platform provides relative to alternative experimental platforms that have been used by other researchers. We anticipate that the nanomagnet-based platform can become an open-ended canvas for experimentally verifying many of the important past and future theoretical results in the thermodynamic limits of computation. For now, the remainder of this dissertation will build on our analysis of energy dissipation in nanomagnetic devices to address practical concerns affecting the reliability and performance of NML.

Chapter 4

Signal Transmission in Nanomagnet Chains

4.1 Implications of Landauer's Principle

One of the most conceptually challenging aspects of Landauer's Principle is the fact that whereas Landauer's derivation applies to a system with two components – a memory element and a thermal reservoir – most practical devices are coupled to a third component, the driving circuitry that modulates the potential energy landscape of the memory element. In the case of nanomagnetic devices, the driving circuitry is the electromagnet that produces the clocking field. The energy dissipation in the driving circuitry is not included in the calculation of energy efficiency. However, neglecting this source of heat dissipation opens the door to criticism of the Landauer principle as being impractical, irrelevant or incorrect.

While it is possible to argue that heat dissipation in an electromagnet is related to its electrical resistance and is therefore technology dependent rather than fundamental, a more convincing approach would be to eliminate the electromagnet entirely. This approach allows us to focus our analysis solely on device components that are active in the logic execution process. The question is whether or not it is possible to operate nanomagnetic devices without driving circuitry.

In this chapter, we examine the role of the clocking field in driving signal propagation in nanomagnetic logic devices. Two distinct regimes of operation are examined, one in which the clock field has little or no role in assisting signal transmission (adiabatic mode) [39] and the other in which it plays an important role (soliton mode) [18, 42]. In the adiabatic mode, Landauer efficiency is attainable and the clock field can even be eliminated entirely. However, speed and reliability concerns with the adiabatic mode may point to the soliton mode as being the more promising route from a practical standpoint.

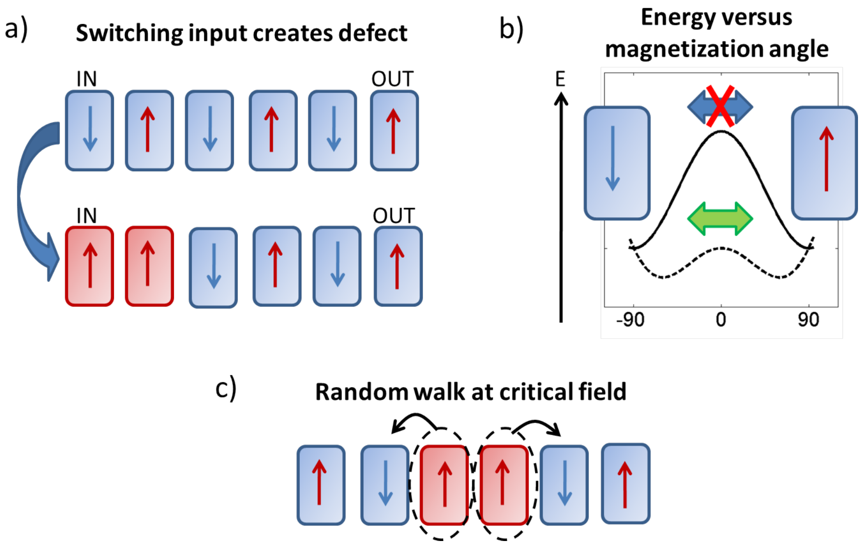

Figure 4.1: Origins of random-walk dynamics. In (a), a change in the input value creates a defect at the beginning of the circuit. (b) Initially, an energy barrier prevents the nanomagnets comprising the defect from flipping, but with a large enough clocking field thermal flipping can occur. (c) Either magnet in the defect pair can flip first, so the defect is as likely to move away from the output as towards it.

4.2 Adiabatic Mode of Transmission

The most widely studied model for NML, based on work by Imre *et al.* [17], is built from arrays of nanomagnets with a single easy axis oriented along their elongated axis. The clock field is applied perpendicular to the easy axis. Here we show that this results in the adiabatic mode of signal transmission, or random walk dynamics.

Our analysis centers on a horizontal chain of nanomagnets with a single input on the left hand side. In order to behave as a functioning NML circuit, the output nanomagnet located on the right hand side of the chain should reflect changes in the input. Every time the input changes its state, a defect comprising two nearest neighbor nanomagnets magnetized in the same direction as one another is generated. The creation of a defect by switching the input is illustrated in Fig. 4.1 (a). This defect must be removed from the chain by propagating to the output, thereby setting the output nanomagnet to the orientation that is logically consistent with the new input.

The role of the clocking field is to modulate the height of the energy barrier separating the up and down states of the magnet. When the energy barrier is high, for example when the clocking field is turned off, the magnets retain their state for a long period of time even when coupled to a thermal reservoir and other noise sources. This is represented by the solid curve in Fig. 4.1 (b). However, as the clock field is increased, the energy barrier becomes comparable to or smaller than the thermal energy. Under these condition, a nanomagnet is able to flip at an appreciable rate between the up and down magnetization states (dotted curve in Fig. 4.1 (b)).

In a chain of nanomagnets, the likelihood of a magnet flipping depends on the configuration of its nearest neighbors. In the case of a nanomagnet that has two nearest neighbors pointed in antiparallel to its current orientation, then the magnet is subjected to a magnetic field in the vertical direction that reinforces its current magnetization state. Such a magnet has a relatively low probability of switching its orientation even when the clock field is turned on. When all the magnets in a chain are aligned antiparallel to one another, then each nanomagnet is under the influence of these reinforcing fields. However, once a defect is introduced into the circuit, either by setting a new input or by other means, then the nearest neighbors of the nanomagnets that comprise the defect are oriented in opposite directions. As a result, their dipole fields offset one another, and the magnet is free to flip as long as the energy barrier is sufficiently low.

Each defect consists of two nanomagnets, one on the left and one on the right. The rate at which each one flips is a function of Arrhenius statistics. It is not known or controllable as to which one will flip first. Each time a magnet flips, the defect moves one position to the left or right and the process repeats. The result is a random walk of the defect, a process that terminates when the defect exits the chain and all the magnets are aligned antiparallel to one another. A step in a random walk is illustrated in Fig. 4.1 (c).

The rate at which the random walk occurs dictates the speed of information transmission in an NML circuit. The rate is a function of the average number of steps in the random walk before the output state is correct multiplied the average time between steps. The average time between steps is controlled by the strength of the clocking field. In fact, there is a range of clocking fields at which signal transmission occurs at an appreciable rate but correctly oriented magnets – those aligned antiparallel to their neighbors – remain unlikely to flip and introduce new defects into the circuit. Within this window, the clocking field can be tuned for either fast propagation speed at the high end or high reliability at the low end. The fastest the magnet can flip is limited by the attempt frequency of the nanomagnet, approximately 10 GHz.

The average number of steps in the random walk is a nonlinear function of the length of the nanomagnet chain. Following a calculation for first passage time of a random walk described by Carlsund [43], we estimated the number of steps needed to transmit a signal along a 10-magnet chain with 99% certainty to be 392 steps. The duration of a clock cycle must therefore be no less than about 40 ns to achieve an error rate of under 1%. Notably, this is significantly slower than the 1 GHz clocking frequency that would be achieved if the transmission occurred by direct propagation from input to output.

Eliminating the clocking field While the use of a clocking field facilitates dynamic control over the rate of the random walk, there are other methods that can be used. In particular, it is possible to tune the shape of the nanomagnet to provide an inherently small anisotropy energy barrier that allows the random walk to occur, and it is possible to change

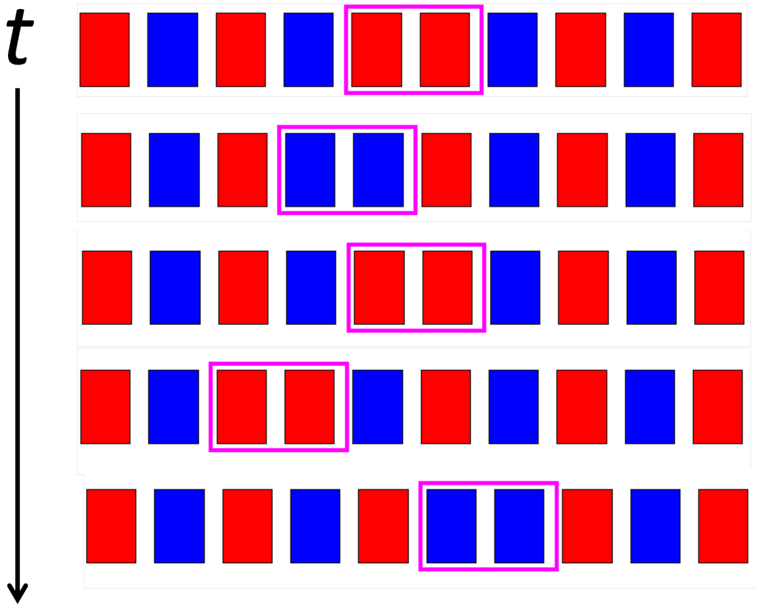

Figure 4.2: Screen shots from a MATLAB simulation in which adiabatic signal transmission occurs.

the temperature of the devices. These approaches can be used to transmit a signal through a chain of nanomagnets without the use of an external magnetic field. This works because there exists a range of energy barriers in which only defects propagate, and a clocking field facilitates but is not necessary to set the barrier correctly.

4.3 Time-Lapse PEEM Imaging of Adiabatic Mode

We conducted a series of micromagnetic simulations and experiments to verify the model we proposed for adiabatic signal transmission in NML. Both OOMMF and MATLAB based simulations were used to solve the stochastic Landau-Lifshitz-Gilbert equation for chains of nanomagnets. As shown in screen shots taken from a MATLAB simulation in Fig. 4.2, random walk dynamics were observed. The energy barrier was tuned to allow random walk dynamics to occur by reducing the shape anisotropy of the nanomagnet, applying a clocking field, and by changing the temperature, validating the hypothesis that any of the three control methods could be used effectively.

The next step was to experimentally observe random walk dynamics in nanomagnet chains. The measurement approach we used for this purpose is photo-electron emission microscopy (PEEM) because it provides resolution on the size scale of individual nanomagnets but does not perturb the magnets. These features of PEEM are crucial because in order to observe random walk dynamics, the microscope cannot induce a bias in the magnetization of the defects as they propagate. However, PEEM has several limitations in the context of our experiment. First, it is not possible to apply a magnetic field strong enough to clock nanomagnet chains to a sample inside the PEEM chamber. The only external control we have of the nanomagnets during a measurement is their temperature. Second, the integration time required to capture a single PEEM image with sufficient contrast to easily resolve the magnetization state of a nanomagnet chain is on the order of one minute. This time scale is not well-matched to the time scale of the random walk dynamics observed in the simulation, which occurred over the course of nanoseconds.

In order to work around the limitations of the PEEM technique while leveraging the tool's unique advantages, we conducted our experiment in the following manner. The sample design included nanomagnet chains with a wide range of aspect ratios, ranging from nearly square nanomagnets to highly elongated nanomagnets. Among the range of aspect ratios were some nanomagnet chains with anisotropy energy barriers within the critical window for successful signal propagation by a random walk at room temperature. At the high end of the range, the random walk occurs very slowly, with the average time between steps on the order of minutes or hours. This allows us to observe the random walk directly by stitching together PEEM images captured sequentially over the course of several hours. By modulating the temperature of the sample, we could adjust the rate of the random walk or change the state of the input nanomagnets.

Another challenge in the sample design for this experiment was the fact that once a defect is removed from a chain, the chain is in an energetic ground state and a new defect is unlikely to reappear. As such, using a sample design in which chains have a single input and output – as in our typical experiments – would undesirably leave many chains without any defects to observe. To work around this problem, we patterned two inputs per chain, one on each end, and set their input state to be logically opposite to one another. This configuration guaranteed that each chain would contain at least one defect, increasing our odds of observing random walk dynamics.

The samples were fabricated using the process flow described in Appendix A. The nanomagnet dimensions were 80 nm wide, 6 nm thick, and with a height that varied from 80 nm to 160 nm in 2nm increments. Each chain consisted of 15 nanomagnets with easy axes in the vertical direction and two input nanomagnets on either end oriented in the horizontal direction and offset from the center of the chain in the vertical direction. The input nanomagnets were elongated to ensure that their magnetization did not change during the experiment. Prior to inserting the sample into the PEEM chamber, a large magnetic field was applied along the horizontal axis of the chain to set the state of the inputs.

After sample fabrication, we began imaging in PEEM. We first scanned the sample to manually identify nanomagnet chains that appeared to be undergoing a random walk at the time scale of interest. We also adjusted the sample temperature. Once we observed chains that appeared to change states between consecutive images, we set up an automated image capture loop. The loop captured about 600 images at 25 second intervals. After completion, the images were processed and played back sequentially as a time-lapse movie.

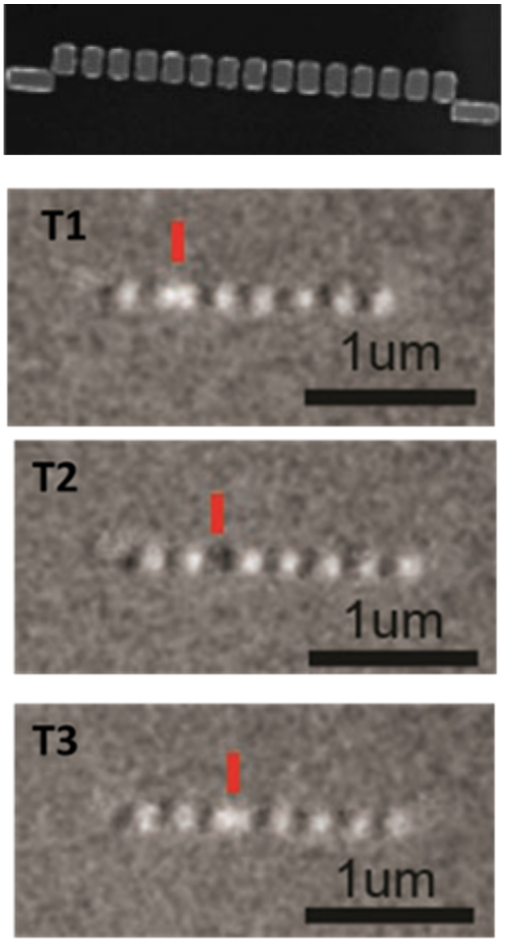

Figure 4.3: Scanning electron(top) and magnetic contrast (bottom) microcraphs of a single nanomagnet chain showing a defect undergoing a random walk over the course of several hours.

In Fig. 4.3, selected images from the time lapse series are shown to illustrate the movement of a defect among different locations in the chain. Each image is of the same chain captured at different times during the experiment. The temperature was fixed during the imaging. At other aspect ratios, the random walk was observed to occur at faster or slower rates, consistent with our model in which the anisotropy energy barrier plays a key role in dictating propagation speed.

Defect annihilation When a NML circuit contains multiple defects simultaneously propagating via random-walk, there is a chance that they encounter one another before reaching an output nanomagnet. In this situation, two outcomes are possible: they can repel one another or they can annihilate one another. The latter outcome is desirable because it means the circuit reaches its ground state more quickly.

Experimental observation is useful to determine which of the two outcomes is most likely in practice. However, it is difficult to engineer a chain that has multiple defects as required to conduct such an experiment. Our approach to this challenge was to engineer the terminal magnets of a chain to serve not as fixed inputs but rather as destabilizers that lower the anisotropy barrier of the magnets at each end of the chain. This allows the terminal magnets to flip due to thermal interactions at a temperature at which other magnets in the chain are stable. These terminal magnets serve as defect ‘generators’ that introduce new defects into the chain even when it is initially in its ground state. The destabilizing force for the defect generators was supplied by horizontally oriented magnets placed at the vertical center of the nanomagnet chain. The dipole fields of the horizontal magnets were directed along the hard axis of the nanomagnets. Because of the defect generators, there was some likelihood that a chain would have multiple defects in it at any given time, allowing us to observe their interaction in PEEM.

In Fig. 4.4, we show PEEM images taken from an experiment similar to the one used to image the random walk of an individual defect. The difference is that now each chain has defect generators on both ends. As required for this experiment, two defects are seen in the chain initially, and both undergo a random walk. Eventually, they approach and annihilate one another. This verifies that annihilation is a usable method for eliminating defects in NML circuits. One practical significance of the finding is that it suggests that by randomizing all of the magnets and allowing the defects to be annihilated, the average transmission speed can be made faster than the original case in which the defect always starts at the input.

4.4 Thermal Clocking

Although the results of the previous section suggest that a clock is not necessary to operate a functional NML device, there still may be value in being able to externally modulate the flip rate of the nanomagnets. For example, because the adiabatic mode of signal transmission is analagous to annealing, there may be annealing protocols that are optimally efficient that require time-dependent control of the flip rate. From earlier experiments, it has been established that an externally applied magnetic field works as a clock that can drive a functioning MLG. However, the resistive losses incurred by modulating a magnetic field electrically are likely to offset much of the energy efficiency gains of the NML architecture. We therefore explore the use of an alternative mechanism, temperature, as a clocking force for NML.

Illustrated in Fig. 4.5 (a), the idea of a thermal clock is to raise the temperature to a high value relative to the anisotropy energy of the magnets to turn the clock on and reduce the temperature to turn it off. At high temperatures, all magnets flip rapidly between the up and down states regardless of their nearest neighbor configuration. Averaged over time, this corresponds to a logically null state similar to a magnet that has been forced to magnetize along its hard axis by an external field. As the temperature is reduced, adiabatic signal

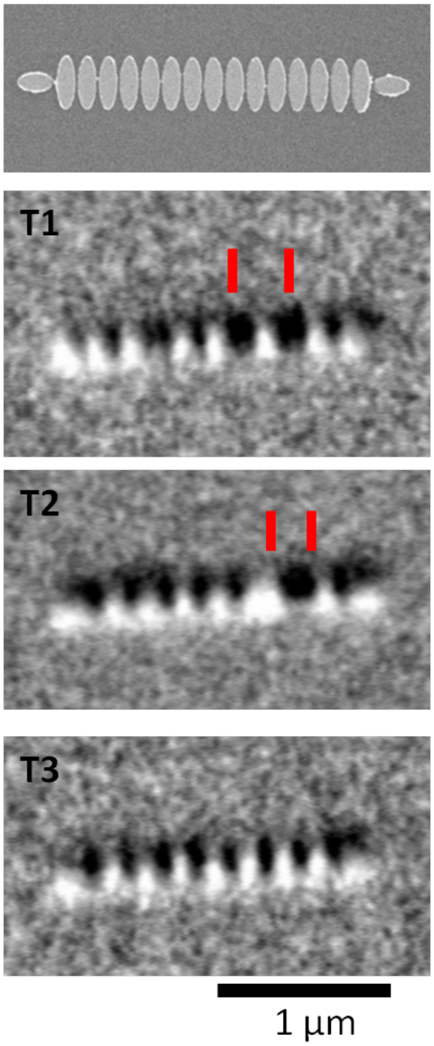

Figure 4.4: Scanning electron (top) and magnetic contrast (bottom) micrographs showing two defects in a nanomagnet chain annihilate one another during adiabatic signal transmission.

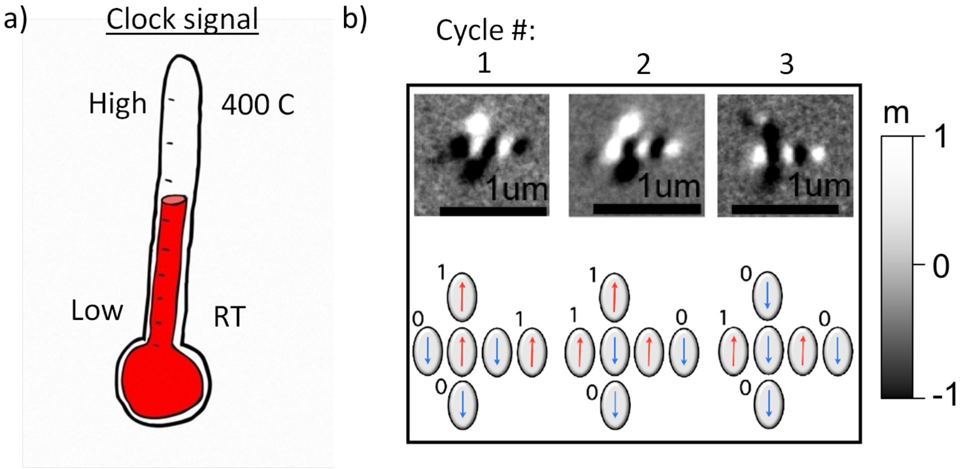

Figure 4.5: Thermally clocking an NML circuit. (a) Depiction of a clock in that switches between a high temperature and a low temperature state to control signal transmission. (b) Magnetic contrast images of a single MLG after three different thermal clocking cycles, verifying correct logical functionality.

propagation occurs and finally all the magnets are locked in their final output state. The clocking cycle can then be repeated with new inputs.

To investigate experimentally, we fabricated MLG's with dimensions similar to the nanomagnet chains investigated in the previous sections. We then cycled the temperature up to about 400 C, near the Curie point of the permalloy nanomagnets. This temperature was high enough that even the elongated input nanomagnets were randomized. Upon cooling, the inputs first settled into new magnetization states and then the majority logic function occurred by adiabatic signal transmission. The output state was then measured in PEEM. Fig. 4.5 (b) shows three PEEM images of the same device taken after consecutive clocking cycles. After each cycle, the inputs change but the output state is the correct boolean function of the inputs. This confirms the possibility of using temperature rather than magnetic fields as a clocking mechanism in NML.

4.5 Soliton Mode of Transmission

A second mode of signal propagation was proposed by Carlton *et al.* [18] and is referred to as a soliton mode because there is a well-defined signal front that propagates unidirectionally from the inputs towards the outputs. The principle of operation in illustrated in Fig. 4.6. After clocking the magnets along their hard axis, magnets successively flip from the hard axis to the easy axis starting at the input. The magnets linger in their logically null state and are tripped when their nearest neighbor flips and exerts a vertically oriented dipole field on them. This mode of propagation was initially proposed to resolve the problem of race conditions in

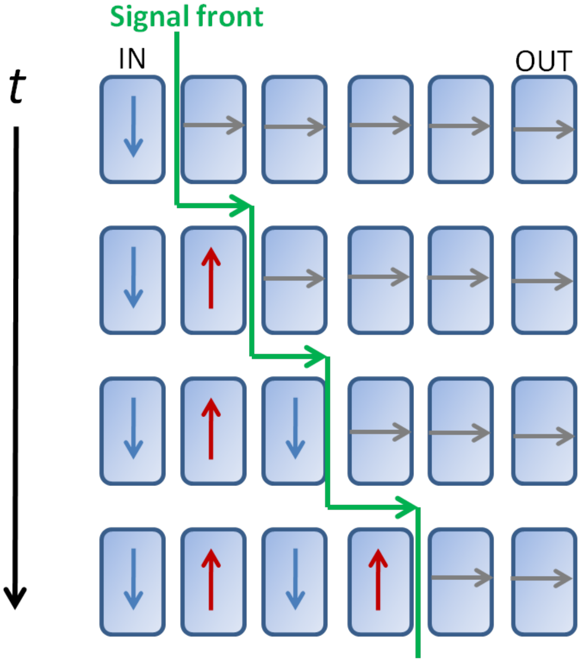

Figure 4.6: Soliton signal propagation in a nanomagnet chain.

MLG's, in which the first input to arrive at the decision bit exerts excessive influence over the output state. Other benefits of the soliton mode have since been appreciated and will be outlined in subsequent chapters.

Comparison to Adiabatic Mode In order for the soliton mode to occur, the energy profile of the nanomagnets that make up the NML circuit must be altered. Typical nanomagnets that are fabricated from permalloy and ellipsoidal or rectangular in shape have a potential energy profile similar to the one shown in the upper plot of Fig. 4.7. The potential energy minima lie along the easy axis and the maxima lie along the hard axis. There are no additional local minima or maxima. Nanomagnets with this or similar potential energy profile transmit signals in the adiabatic mode. A potential energy profile similar to the one in the lower plot of Fig. 4.7 is desired to achieve the soliton mode. The local minimum in potential energy along the horizontal axis ensures that magnets that are horizontally magnetized by the clocking field linger in this state after the clocking field is removed. Only when a biasing field is applied in one of the vertical directions does the magnet exit the energy well and flip to the vertical axis. The depth of the energy well should be sufficient to ensure that thermal agitation does not cause magnets far from the inputs to flip inadvertently, but it should not be so deep that the stray fields from its neighbor cannot flip it when the signal front has arrived.

One of the fundamental differences between the adiabatic mode and the soliton mode of

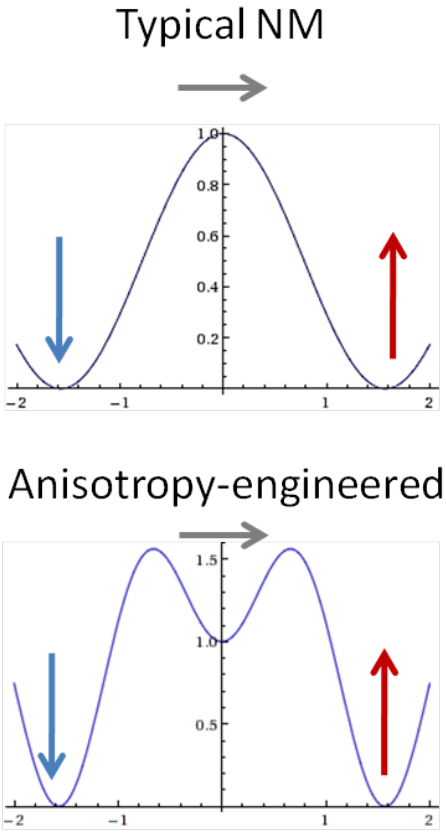
Typical NM

Anisotropy-engineered

Figure 4.7: Comparison of the energy profile of a typical nanomagnet used in NML applications versus the energy profile necessary for soliton signal transmission to occur.

signal propagation is the transfer of energy between the clocking field and the nanomagnets. In the adiabatic mode, the role of the clocking field is to modulate the height of the energy barrier separating the up and down magnetization states of the nanomagnets. The raising and lowering of an energy barrier is a reversible physical process provided the magnets remains in or near thermal equilibrium as the field changes. This can be accomplished by changing the field slowly, and it means the clocking field does not need to supply any energy to the nanomagnets, an issue we explored earlier in Chapter 2. On the other hand, in the soliton mode, the nanomagnets do not remain in thermal equilibrium – the metastable hard-axis state of the nanomagnets is a non-equilibrium configuration. Therefore, the clocking of an NML circuit is accompanied by the transfer of energy from the clock field to the nanomagnets. This energy is dissipated as heat when the magnets flip from the hard axis to the easy axis.

The above analysis suggests a tradeoff when comparing the adiabatic and soliton mode of NML operation. In the adiabatic mode, fundamental thermodynamic limits of computation are attainable, a scientifically and technologically interesting proposition. However, performance and reliability suffers as a result of the stochastic nature of signal transmission. The solution is to adopt the soliton mode of transmission, which is deterministic and can therefore be much faster on average. The tradeoff is that the clocking field must now do work on the nanomagnets in order to impart the hard-axis metastability required for the soliton transmission to occur. Whether or not this trade-off is worthwhile depends to some extent on how much the reliability suffers in the adiabatic mode, a question we explore in greater detail in the next chapter.

Chapter 5

Study of the Reliability of Nanomagnet Chains

5.1 Limitations of Fabrication

In the last chapter, we examined different modes of signal transmission in nanomagnet chains. The picture that was painted was somewhat idealistic. Our simulation models assumed perfectly fabricated chains, and our experiments did not address the statistical likelihood of a particular behavior being observed. As a result, we lacked insight into the reliability of NML, an important metric if practical applications rather than scientific discovery are one of the end goals of our research.

This chapter examines what happens when we relax the assumption of perfectly fabricated NML circuits. We develop several models for lithographic variations among magnets that can be implemented in micromagnetic simulations using a single-spin approximation [44]. This allows for rapid statistical analysis, as thousands of single spin simulations can be run over a span of hours or days. We also consider nonidealities that affect the clocking field, such as the angle at which the clocking field is applied relative to the horizontal axis of a chain of nanomagnets.

The stochastic parameters in our simulations are fitted to experimental data gathered primarily from large arrays of nanomagnet chains fabricated by our standard liftoff process. This gives us insight into how close or far our current devices are from meeting reliability benchmarks needed for practical applications. Even though the analysis in this chapter is by nature technology-dependent, we find that it is still possible to draw conclusions about the likelihood of various approaches to NML working.

5.2 Approach

The results of this chapter involved conducting experiments to gather information about errors in NML circuits and then developing simulation models that fit the experimental

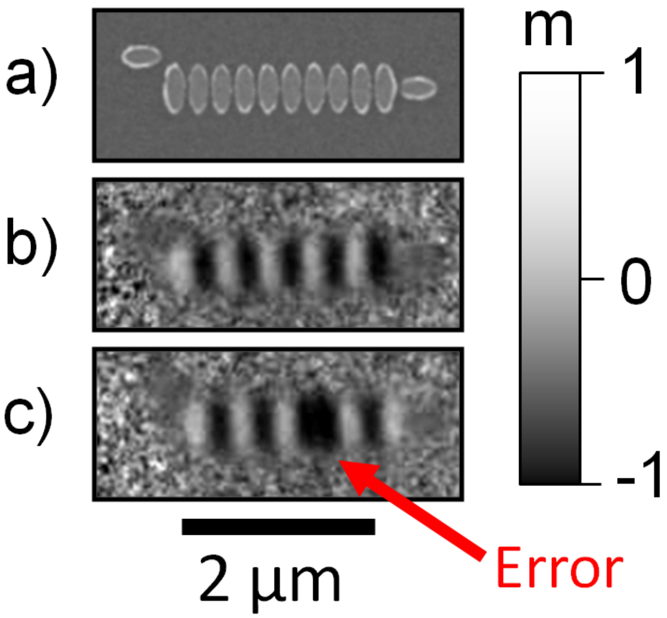

Figure 5.1: Scanning electron (a) and magnetic contrast (b) and (c) images of two different nanomagnet chains with similar dimensions. The chain in (b) is error free (all magnets are magnetized antiparallel to their nearest neighbors) whereas the chain in (c) contains an error as indicated.

data. The experiments were carried out using PEEM and MFM techniques. An example of an error measured by PEEM is shown in Fig. 5.1 (c). Two neighboring magnets aligned parallel to one another stand out as unusually large white or black regions, facilitating the process of counting errors. The PEEM microscope's wide field of view and relatively short time needed to capture images once a sample has been loaded into the chamber made this technique well-suited to our statistical analysis. Each sample used in this technique consisted of large arrays of nanomagnet chains, often with hundreds of identical chains per array, so that statistically relevant numbers of devices could be analyzed efficiently.

The MFM technique does not offer the wide field of view or fast imaging time of the PEEM technique. However, one advantage of MFM is the ability to apply a clocking field to a sample without unloading it. Therefore, we used MFM to study the reliability of an individual chain of nanomagnets as it undergoes multiple clocking cycles. Together with PEEM, we were able to explore reliability in NML circuits across two distinct dimensions: reliability among many different NML circuits and reliability of a single circuit over multiple clock cycles.

Once we gathered and analyzed the experimental data, we conducted analogous micromagnetic simulations and tried to methodically introduce nonidealities into the simulations that matched the experimental data. The nonidealities could include variation in the size of

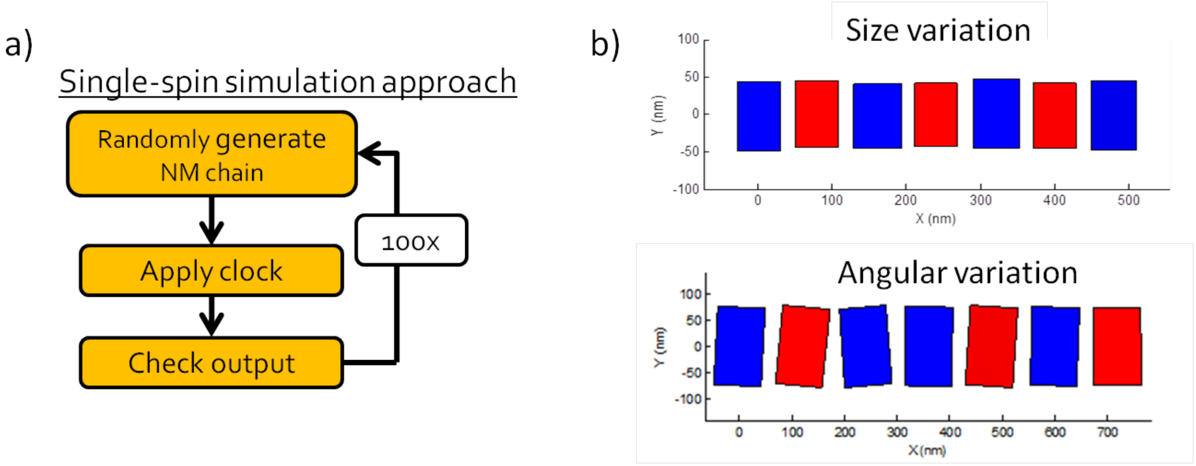

Figure 5.2: (a) Approach to conducting statistical reliability analysis using micromagnetic simulations. (b) Illustration of two types of nonidealities that were studied by statistical analysis.

the nanomagnets, variation in the angle of the nanomagnet easy axis, and variation in the angle of the clocking field. Because we hoped to use the single spin approach, we did not include nonidealities such as edge roughness which require pixel by pixel control over the nanomagnet shape. Such nonidalities were assumed to be encapsulated in the variation in size and angular alignment of a nanomagnet.

A typical simulation process is diagrammed in Fig. 5.2 (a). First, a random generator is used to produce an NML device, typically a chain of nanomagnets, with variations among nanomagnets. A parameter such as a standard deviation is typically defined during this step. Second, we run the simulator by clocking the device and calculating its evolution over time using the stochastic LLG equation. Various clocking procedures and temperature parameters could be used to achieve different outcomes. Finally, we check and tabulate whether or not the output state contained errors. The simulation process is then repeated on the order of 100 times to gather statistics. In some cases, a new chain is generated in every clocking cycle, whereas in others the same chain is clocked multiple times. Examples of randomly generated chains are shown in Fig. 5.2 (b).

5.3 Errors in ideal chains

Before investigating errors in non-ideal chains of nanomagnets, we carried out simulations on ideal chains. Our motivation was two-fold. First, we wished to compare the minimum achievable error rates for adiabatic versus soliton mode of signal propagations, and second, we wished to compare various procedures for clocking NML circuits at different time scales.

Fig. 5.3 shows two simulations comparing the adiabatic and soliton modes of signal

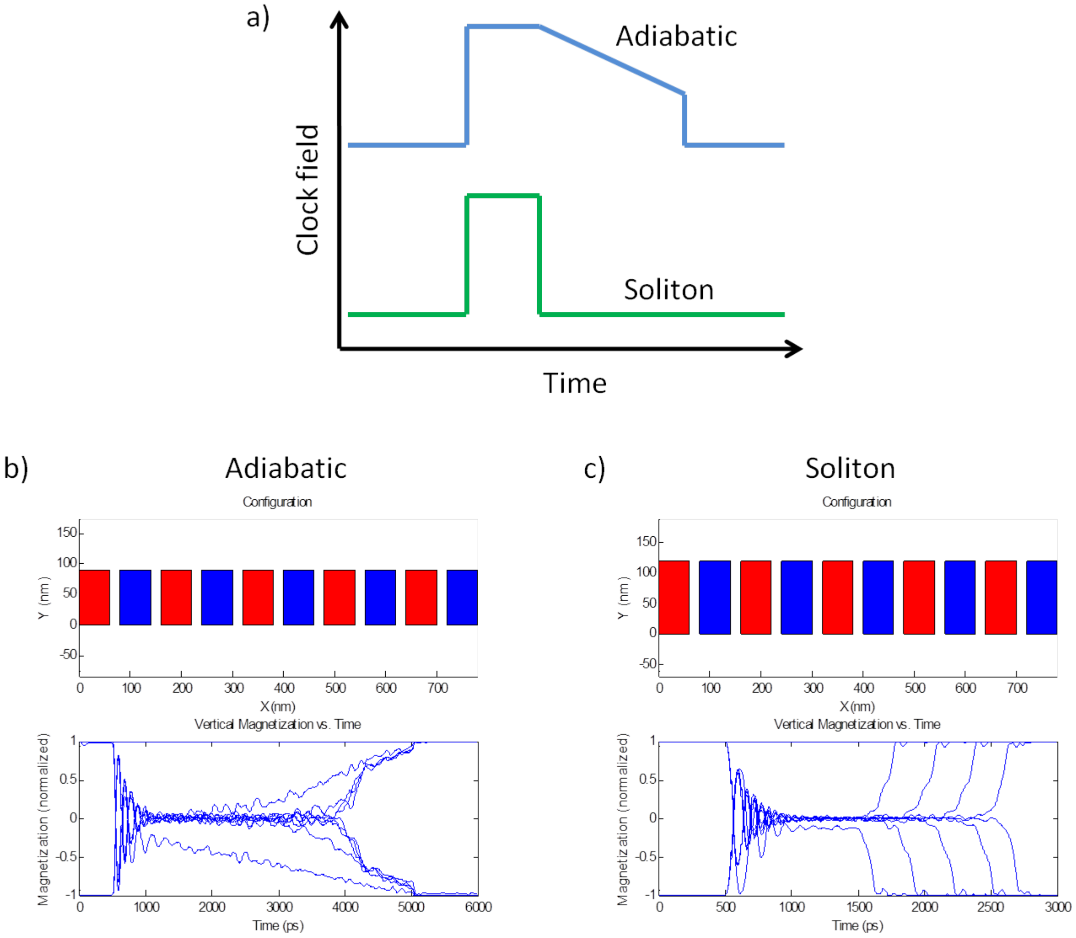

Figure 5.3: (a) Clocking field waveforms optimized for different modes of signal transmission. In (b) and (c), the results of micromagnetic simulations using these waveforms is shown. The upper portion of the image depicts the chain and the lower portion depicts the evolution of the magnetization of each nanomagnet as the clocking field is cycled.

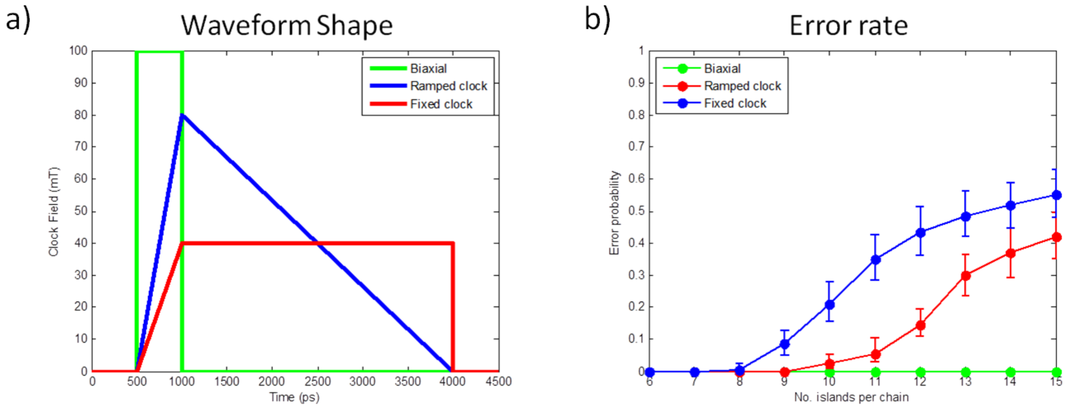

Figure 5.4: Comparison of error rates in ideal nanomagnet chains with different clock waveforms and modes of signal transmission. (a) Timing diagram of the clock waveform and (b) error rate as a function of chain length.

transmission. Because the dynamics are different, we expect the behavior and reliability to depend on the procedure for applying the clocking field. In the soliton mode, the random-walk requires the clocking field to remain high for a long enough period of time for any defects to exit the chain. One way to accomplish this is to ramp the field down slowly from a high value to a low value before removing the field entirely. This procedure is shown in the top curve of Fig. 5.3 (a). The resulting dynamics are shown in the bottom plot of (b), which shows the vertical component of the magnetization of each nanomagnet as a function of time. As the clock field is reduced, all of the magnets slowly rotate from horizontal magnetization (correponding to zero vertical magnetization) to the vertical axis. In the soliton mode of transmission, a ramped clock field is unneccessary. Once the clock field forces the magnets to the horizontal magnetization state, it can be removed abruptly and the cascade begins. The bottom plot of 5.3 (c) reveals the one-by-one flipping of magnets from the horizontal to the vertical axis after the clock field is removed.

The next question to address is how these two modes of signal transmission compare in terms of reliability. We ran batches of 100 simulations similar to the ones shown in Fig. 5.3. Each simulation used a different seed for the random number generator used to simulate the effect of temperature, leading to slightly different behavior in each simulation. The temperature parameter was set to 300 K. We also varied the clock waveform, as shown in Fig. 5.4 (a). For soliton mode (also referred to as biaxial mode), we used the abrupt rising and falling edge waveform, whereas for adiabatic mode we tested the two different procedures characterized by the red and blue curves. For the ‘fixed clock’ waveform, we set the field to a value at which the random-walk occurred and held the field at that value for 3 ns before removing it. For the ‘ramped field’ waveform we initially increased the clock field to a very high value and then slowly ramped it down to zero.

In Fig. 5.4 (b), we compare the error rates for the three clock waveforms shown in (a).

We measure the error rate as a function of increasing chain length, which is varied from 6 to 15 magnets. Several observations can be made from this data. First, no errors occur in the biaxial mode of signal transmission, independent of chain length. This suggests that it may be promising to us the biaxial mode for long distance communication in NML circuits. The adiabatic mode has a nonzero error rate after about eight or nine magnets, depending on the clock waveform. The error rate gets as high as about 50% for the longest chains. The results of the adiabatic mode simulations depend strongly on the clock waveform, with the fixed field procedure yielding lower error rates. This suggests that the longer time the clocking field is set within the critical range for the random walk to occur, the better the error rates are. However, a broader conclusion is that only short chains can reliably propagate a signal in the adiabatic mode, even if the clock field procedure is optimized.

5.4 Experimental data

At the time the following experiments were carried out, only chains that operated in the adiabatic mode could be fabricated. Therefore, the experimental portion of our study of error rates is restricted to adabatic signal transmission. In Chapters 6 and 7, we will examine methods of fabricating NML circuits that operate in the soliton mode.

Using MFM, we collected error statistics from a single chain of nanomagnets clocked multiple times. In between each measurement, a clocking field of 2200 Gauss or -2200 Gauss was applied along the horizontal axis of the nanomagnet chain, alternating between a positive and negative field. The benefit of the alternating field was to ensure that the entire chain was being clocked properly. The chain was clocked 20 times, and after each cycle we noted the number and location of errors in the chain. The results are shown in Fig. 5.5. In (a), we show the raw data, with boxes indicating errors. In (b), we show a histogram of the location of errors over the 20 clock cycles. The island number indicates the position of the error. The histogram reveals that errors occurred in preferred locations along the chain; some locations contained errors after most if not all clocking cycles, while others never contained errors. This data strongly suggests that lithography plays a role in the number and location of errors in the chain, with the nonuniformities among neighboring magnets giving rise to ‘sticking points’ for defects as they undergo a random walk.

The MFM experiments were restricted to a small number of chains due to the relatively small field of view of the microscope and the challenging procedure for moving the probe tip to different regions of a sample. Therefore, our study of the reliability of large numbers of nominally identical chains was carried out using PEEM. We fabricated samples containing arrays of over 100 chains and imaged them in PEEM after applying a clocking field. An example of a PEEM image from this study is shown in Fig. 5.6 (a). Errors show up prominently as white or dark regions on a predominantly gray background.

One of the parameters varied in this study was the length of the chains in the array. In Fig. 5.6 (b), we show the error rate as a function of chain length. Here, the error rate is normalized to the length of the chain i.e. we count as the number of errors per chain and divide by

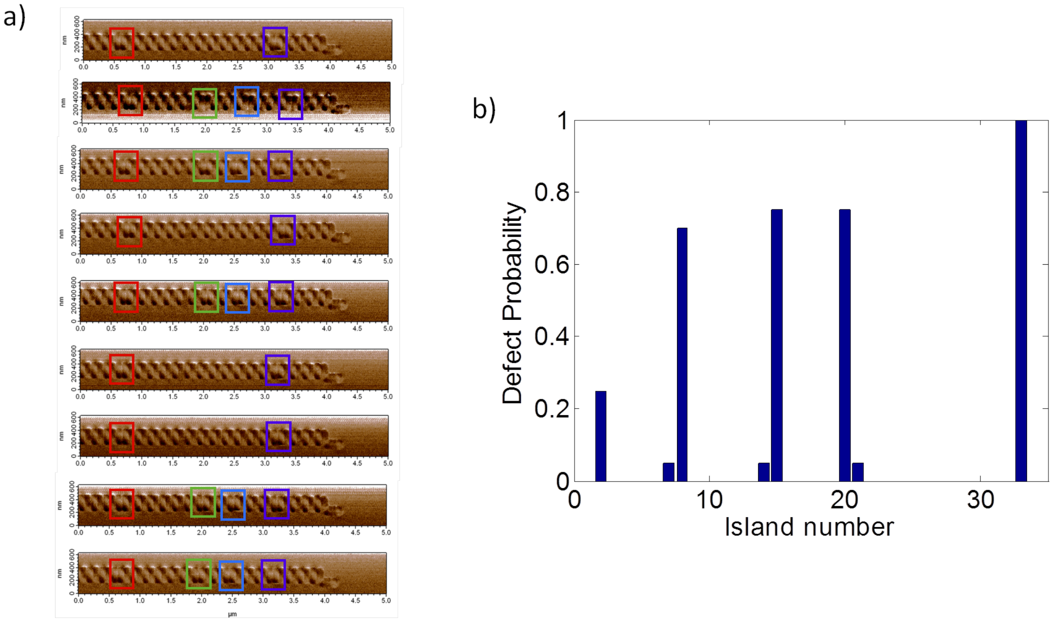

Figure 5.5: (a) Magnetic force microscopy images of a single nanomagnet chain after repeated clocking cycles. Colored boxes indicate logical errors in the output state. (b) Histogram showing the frequency and locations of errors over 20 clocking cycles.

the number of magnets per chain. Each data point is the average of about 100 chains, with each chain clocked only once. The error rate is low for short chains but plateaus at about 0.05-0.10 for longer chains, meaning an error occurred once every 10-20 magnets. The low error rate for very short chains indicates that the input magnet exerts a direct influence on the first few magnets that forces them into the correct output state most of the time. This force becomes negligible more than 2-3 magnets from the input. Another important observation is that the error rates are very high compared to the micromagnetic simulations carried out in the previous section. The error rate in the simulations was substantially zero for chains shorter than eight magnets, whereas the experimental error rate is nonzero even for one- or two-magnet chains. This discrepancy is likely attributed to fabrication-related nonidealities, the effects of which we explore using micromagnetic simulations.

5.5 Simulation data

Using the simulation approach outlined earlier in the chapter, we attempted to model nonidealities observed experimentally by making simple adjustments to otherwise idealized single-spin simulations. Two particular approaches were tested: size variations and angular variations among nanomagnets (see Fig. 5.2 (b)). In both cases, we ran simulations that corresponded to experiments in which we examine trends in error rates as a function of the

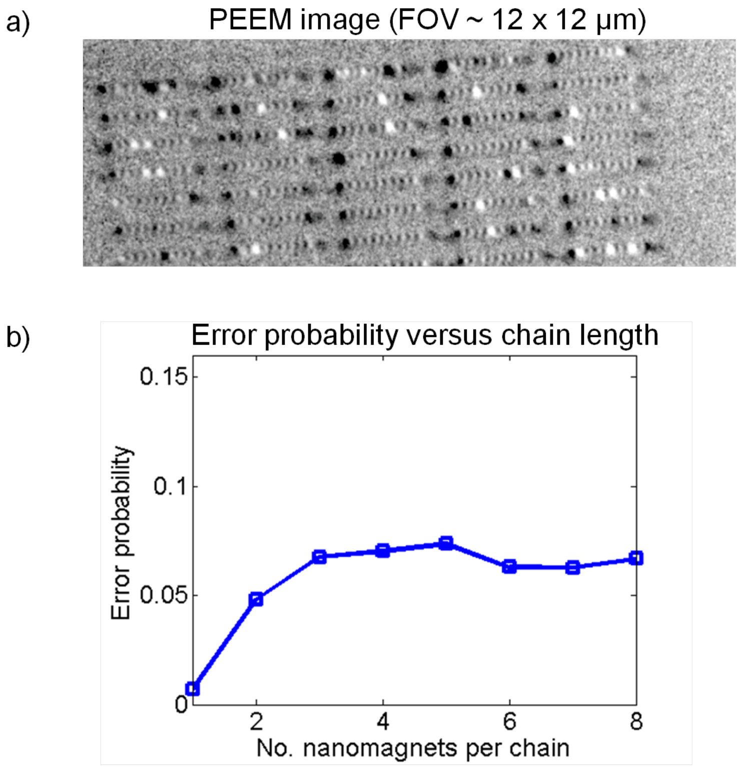

Figure 5.6: (a) Magnetic contrast image of an array of nanomagnet chains. Bold black and white regions indicate logical errors. (b) Results of statistical analysis of errors in nanomagnet chains, plotted as a function of the chain length.

length of the nanomagnet chain. We also examined the reliability of a single long chain over multiple clock cycles.

Of the two approaches, the simulations that incorporated angular variations among magnets gave the most accurate agreement with experimental data. Some of the illustrative results are shown in Fig. 5.7. In (a), an example chain with a randomly distributed easy axis angle with a standard deviation of 3° is shown. In (b), we examine the error rate as a function of chain length, an analysis corresponding to the experimental data in Fig. 5.6 (b). The misalignment angle (given as a standard deviation) ranged from 1 to 3 degrees. While approximate, the 2° misalignment angle was quantitatively the closest match to the experimental angle. In (c), we simulate the clocking of a long chain with a 2° misalignment angle 100 times and plot the distribution of errors. This simulation is analogous to the experimental data shown in Fig. 5.5. Again, strong qualitative agreement is observed between the two plots, in particular the clear presence of preferred locations for errors.

Adiabatic vs. soliton mode Experimentally, we were unable to test the reliability of NML circuits operating in the soliton mode of signal propagation. In simulation, though,

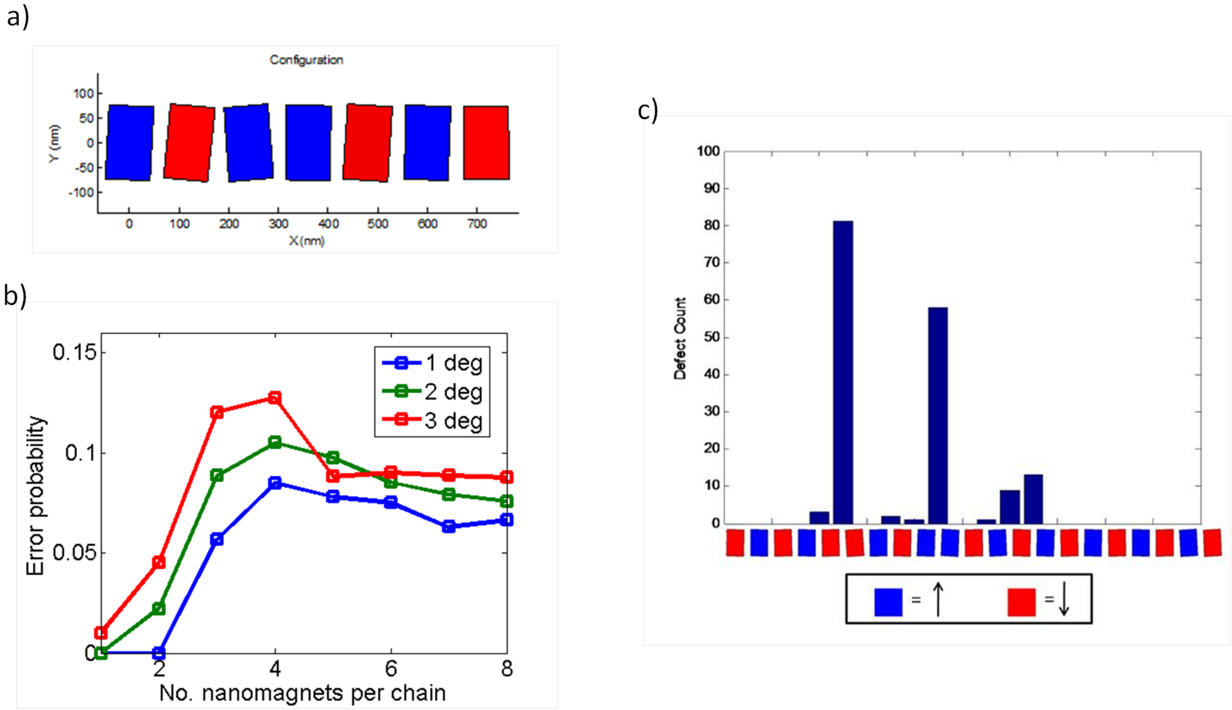

Figure 5.7: (a) Example of a chain of nanomagnets with a distribution in misalignment angle among neighbors. (b) Simulated error rate as a function of chain length for chains with a standard deviation of 1-3° in misalignment angle. (c) Histogram of the frequency and location of errors after simulating the clocking of a single chain with a misalignment angle of 2° 100 times.

we faced no such restrictions. We therefore used single-spin simulations to compare the reliability of NML chains in the presence of fabrication-related nonidealities.

For the comparison, we simulated chains of eight nanomagnets with an angular misalignment in the easy axes of the nanomagnets operated in both the adiabatic and soliton mode. In these simulations, all the nanomagnets in a chain were ideal except for one magnet in the middle of the chain. The central nanomagnet had an angular misalignment was varied from 0° to 4° in increments of 0.5°. This helped us maintain a consistent comparison between the adiabatic and soliton mode by not introducing a stochastic element to the simulations. The simulations were carried out in the manner described in Fig. 5.2 (a). In the nanomagnet chains operating in the soliton mode, we varied the strength of the biaxial anisotropy term from 32 to 46 kJ/m^3.

The results of the simulations are shown in Fig. 5.8. In (a), we observe that the error rate of the adiabatic mode of signal transmission has a nonzero slope at the origin. From the standpoint of practical applications, this is bad news because it means that unless the fabrication results in all but perfect nanomagnet chains, the error rates will be substantial.

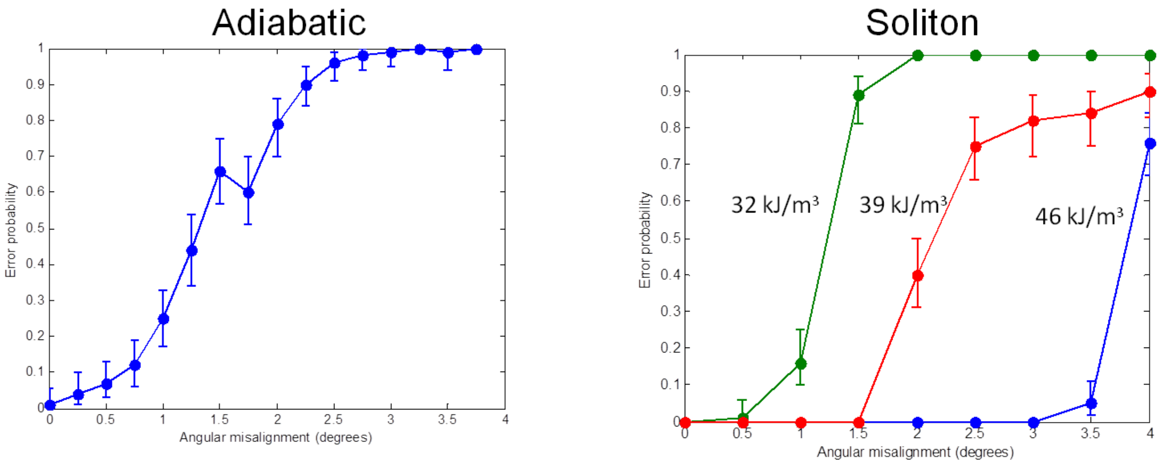

Figure 5.8: Comparison of error rates in the adiabatic mode (a) and soliton mode (b) as a function of misalignment angle of a central nanomagnet in a chain. The chains operating in the soliton mode had varying amounts of biaxial anisotropy energy density.

The better scenario is shown in (b), where the error rate in NML chains operating in soliton mode becomes nonzero only after the angular misalignment surpasses a critical threshold. This implies that as long as the fabrication of NML devices conforms to a particular tolerance, then reliable signal transmission is achievable. The higher the anisotropy energy density, the greater the tolerance to nonidealities.

5.6 Discussion

Reducing the error rates in NML is one of the most important hurdles to overcome in order to pursue the deployment of this technology in practical applications. The results of our experiments and simulations help to understand the origins of errors in NML and suggest a roadmap for how to eliminate them.

The first observation from our data is that there is both a deterministic and random source of errors in the adiabatic mode of signal propagation. The deterministic component arises from fabrication related nonidealities in the circuit that cause variations among individual nanomagnets. In particular, our analysis suggests that there is a real or effective misalignment in the easy axis of the nanomagnets relative to the vertical axis of the circuit. This effect is manifested as preferential locations of errors in the output state and nonzero error rates even for very short chains. The random component of the error rate arises from thermal fluctuations that cause repeated clocking of a single chain to yield different results in different cycles. In both experiment and simulation, cycling the clock on a single chain and tabulating the location of errors after each cycle gave support to the hypothesis of both a deterministic and random contribution to the error rate in NML chains. Perhaps a larger takeaway message is that the error rate in NML chains operating in the adiabatic mode is substantial, casting a serious doubt on its viability as a practical route to applications.

The second observation from the simulation data is that the soliton mode of signal transmission has a tolerance for angular misalignment whereas the adiabatic mode does not. Moreover, there were no observable thermally induced errors in the soliton mode in our simultations. This suggests that both the deterministic and random sources of errors are mitigated when operating in the soliton mode. Moving forward, these results teach us that the soliton mode is the key to achieving high reliability in NML circuits. The next two chapters will explore a new method for implementing the soliton mode in practice and verify its impact on error rates experimentally.

Chapter 6

Anisotropy Properties of Concave Nanomagnets

6.1 A Need for Anisotropy Control

A typical nanomagnet used in NML applications has a rectangular or ellipsoidal shape. Due to the shape anisotropy contribution, the long axis of the magnet is an easy axis. No other easy axes – defined here as local or global minima in the magnetic potential energy landscape – exist in such nanomagnets. This form of anisotropy works well for the adiabatic mode of signal propagation. However, for the soliton mode of signal transmission, it is problematic because two easy axes are needed: one along the information-bearing axis (vertical) and the other in the direction of the clocking field (horizontal).

Shape anisotropy alone is insufficient to provide more than one easy axis. The contribution of shape anisotropy to the energy profile of a nanomagnet has a $\sin^2\theta$ dependence in two dimensions, where θ is the magnetization angle in the plane of the sample. This function has two energy minima separated by 180°. What is needed is four energy minima separated by 90° (all the minima need not be of equal depth). We established in the previous chapter that the soliton mode of signal propagation is desirable for its improved reliability relative the the adiabatic mode. Our challenge, then, is to engineer nanomagnets with fourfold anisotropy by tuning their material properties and geometry and then apply such nanomagnets to NML circuits operating in the soliton mode.

In this chapter, we introduce a method for controlling anisotropy in nanomagnets by tuning the edge profile of the nanomagnet. In particular, we explore the impact of concave shapes (shapes with indentations along one or more edges) on the anisotropy properties of nanomagnets. This approach is based on the same physical foundation as configurational anisotropy, where geometric features such as corners of polygons are used to induce anisotropy. Our new approach is compared to other common methods for tuning anisotropy properties such as the use of crystalline materials exhibiting magnetocrystalline anisotropy.

6.2 Existing Methods for Anisotropy Control

Before examining anisotropy in nanomagnets with concave shapes, we survey methods for anisotropy control that have been investigated previously and clarify their limitations in the context of NML applications. We examine three methods: shape, magnetocrystalline, and configurational anisotropy. Other methods exist and may play a role in future NML developments, such as interfacial anisotropy. However, the three discussed here have played the most prominent role in the course of the work carried out for this dissertation.

Shape anisotropy As mentioned previously, shape anisotropy has been the conventional choice for NML applications to date. Shape anisotropy arises in single domain nanomagnets with elongated geometries, such as ellipses. Due to the difference in the strength of the demagnetization field depending on whether the particle is magnetized along the long axis or short axis, the long axis behaves as a magnetically easy axis. For many computational applications, a single easy axis is sufficient because it allows the magnet to store binary information in a non-volatile manner. However, it does not meet the dual-axis stability requirements for NML operating in soliton mode.

Magnetocrystalline anisotropy A second type of anisotropy that has found widespread use in commercial applications such as magnetic hard disk drives is magnetocrystalline anisotropy. This type of anisotropy arises from the spin-orbit interaction in crystalline magnetic materals, whose long-range translational symmetry gives rise preferred axes of magnetization. Depending on the crystal structure of the material, magnetocrystalline anisotropy can give rise to one or more easy axes. For example, a material with a cubic crystalline structure may have three easy axes that lie along the $\langle 100 \rangle$ directions.

Our initial attempts to engineer NML circuits operating in the soliton mode used magnetocrystalline anisotropy. With the assistance of collaborators at IBM and the UC Berkeley Department of Physics, we obtained unpatterned films of crystalline magnetic materials grown by molecular beam epitaxy (MBE). Two types of films were obtained: single-crystal iron on a magnesium oxide substrate, and single-crystal cobalt on a copper substrate.

There are several limitations of using magnetocrystalline anisotropy in NML applications, the sum of which led to us eventually abandoning the approach. The most significant challenge is that it was found to be difficult and unreliable to etch nanostructures into crystalline magnetic materials. Our typical lift-off fabrication process does not work on MBE-grown materials. An etching process must be used, a more complicated procedure due to the need to deposit and then remove an etch mask without leaving residue on the protected nanomagnets. The process is made more difficult by the fact that single-crystal iron and cobalt have relatively low etch rates. Another limitation of using magnetocrystalline anisotropy is that the strength of the anisotropy is not tunable once the film is grown. In NML devices there is a high sensitivity to the balance between the magnetocrystalline and shape anisotropy. Without being able to optimize the magnetocrystalline anisotropy strength, it is very difficult to engineer working NML circuits. While there may be long term hope for overcoming these challenges, an alternative experimental approach is desirable in the early stages of NML development.

Configurational anisotropy When designing NML devices, we often assume that the magnetization of a single-domain magnetic nanoparticle is approximately uniform. However, this assumption that is not always valid, and the subdomain configuration of single domain nanomagnets can change their anisotropy properties significantly. Configurational anisotropy arises in single-domain nanomagnets that enter non-uniform magnetization configurations to minimize magnetic charge at interfaces [45]. The energy landscape in configuration space may contain local minima that do not exist when considering the case of uniform magnetization only, leading to the emergence of multiple easy axes. For example, in polygon-shaped nanomagnets, easy axes could be oriented towards either the corners or edges of the polygon, depending on the film thickness [46]. Because configurational anisotropy is not restricted to a single easy axis, it has the potential to be used to achieve soliton mode behavior in NML.

We first encountered configurational anisotropy experimentally while characterizing the anisotropy properties of rectangular nanomagnets using the MOKE technique described in Appendix B. An array of identical rectangular nanomagnets 80 nm in width, 120 in height, and 10 nm in thickness were first deposited by our lift-off fabrication technique. The array size was about 1 mm x 1 mm with a magnet-to-magnet spacing of 600 nm. When we measured their anisotropy profile, we observed two easy axes oriented along the diagonals of the rectangle. Although the configurational anisotropy contribution is weak relative to the strength of the shape anisotropy, its effect was sufficiently large to warrant further investigation.

Using micromagnetic simulations, Cowburn *et al.* found that easy axes oriented towards corners of a polygon shape were indicative of a low-energy magnetization state referred to as the 'leaf' state [47]. The leaf state is an outwardly bowed configuration that causes magnetic charge to be concentrated in opposite corners of the nanomagnet. Its converse is the 'flower' configuration, an inwardly bowed configuration that causes magnetic charge to be concentrated towards the edges. In square nanomagnets, the leaf state was found to be more stable in thin film nanomagnets, but in thicker films the flower was found to be more stable. The difference is nontrivial, because the easy axis of the leaf configuration is parallel to the diagonal of the nanomagnet whereas the easy axis of the flower configuration is parallel to the edge. In NML applications, it is desirable for the easy axes to lie parallel to the edges of the nanomagnets. However, in nanomagnets whose dimensions are similar to those used previously in NML, configurational anisotropy tends to induce easy axes along the diagonals. This is a key limitation to an otherwise suitable method for anisotropy control in NML applications. Our objective in the work presented in this chapter is to overcome this limitation through the use of concave shaped nanomagnets.

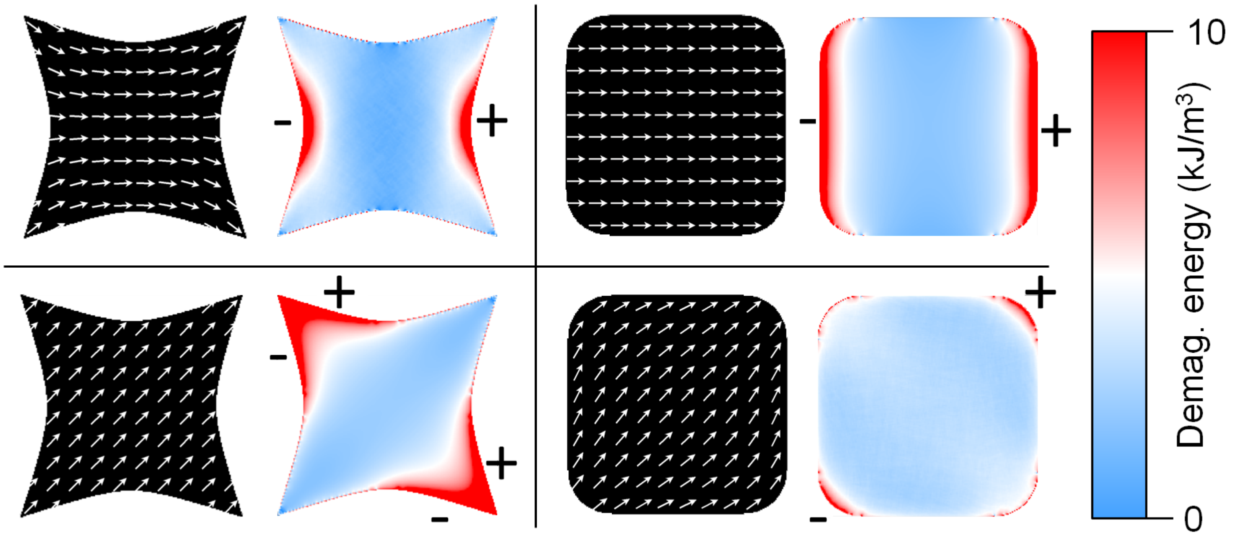

Figure 6.1: Micromagnetic simulations of concave (left column) and simple (right column) square nanomagnets magnetized along 0° (top row) and 45° (bottom row). The left image shows the magnetization pattern and the right image shows the distribution of demagnetization energy. The presence of magnetic charge near regions of high demagnetization energy is indicated. The corners of the simple square were rounded to account for lithographic limitations but do not impact the results meaningfully.

6.3 Anisotropy in Concave Nanomagnets

Small magnets with concave edge profiles have been shown to have anisotropy properties that substantially differ from those of convex shapes [48, 49]. It is natural that configurational anisotropy, which depends on interactions at the interfaces of nanomagnets, is highly sensitive to the geometry of the nanomagnet. Concavities have a large surface area and therefore have a disproportionate impact on the overall anisotropy profile. Prior literature stops short of developing a detailed understanding of micromagnetics of configurational anisotropy in concave nanomagnets, perhaps because this analysis would have had little practical value at the time. Our starting point is therefore to carry out micromagnetic simulations that shed light on the interplay of magnetic charge that affects anisotropy in concave nanomagnets. We then conduct experiments to verify the simulation data. In the next chapter, we explore the application of concave nanomagnets to NML.

Micromagnetic simulations using OOMMF [50] were carried out to investigate the origins of configurational anisotropy control in concave nanomagnets. In Fig. 6.1, we compare the magnetization patterns of normal and concave square nanomagnets when magnetized along both 0° and 45°. The dimensions of the squares are 100 nm x 100 nm x 10 nm. When magnetized along easy axes, the nanomagnets were allowed to relax to their stable

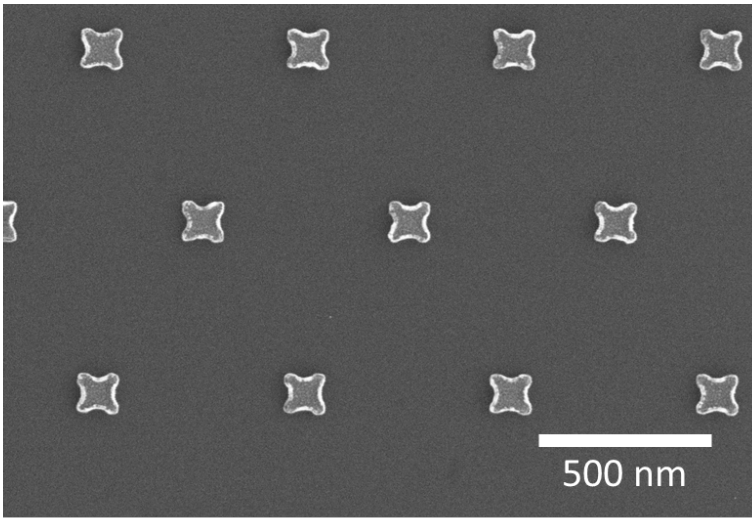

Figure 6.2: Scanning electron micrograph of an array of concave nanomagnets.

configuration, and along the hard axes, the nanomagnets were held fixed with uniform magnetization. Fig. 6.1 also shows the distribution of demagnetization energy density for each configuration. A high demagnetization energy density arises from magnetic charge accumulation at the surface of the nanomagnet. In a concave square magnetized along its easy axis (0°), regions of high demagnetization energy are located on opposite sides of the shape from each other, indicating that magnetic charges are well-separated. On the other hand, when magnetized along the hard axis (45°) the demagnetization energy is concentrated intensely in the upper left and lower right corners of the magnet. This indicates that a large concentration of magnetic charge of opposite polarity accumulates in close proximity to each other, and it is a result of the constricted geometry near corners. Further narrowing of the nanomagnet corners by increasing the concavity depth would continue to increase the total demagnetization energy of the 45° magnetization state. For comparison, a simple square nanomagnet is shown in the right column of Fig. 6.1. A simple square nanomagnet oriented at 45° adopts an outwardly bowed magnetization configuration that concentrates magnetic charges at opposite corners, where they are furthest apart from each other. The maximal separation between opposing charges means the diagonal axis is easy. But even when the normal square is magnetized along its hard axis (0°), there remains a relatively large distance between the uncompensated spins, so the difference in demagnetization energy between the easy and hard axes of a simple square is significantly smaller than that of a concave square. Thus, configurational anisotropy can be enhanced in concave nanomagnets compared to normal nanomagnets. Furthermore, the direction of the easy axis can be rotated from the diagonal axis of the square to the edge axis.

To carry out experiments verifying our findings in micromagnetic simulations, we fabricated arrays of identical concave nanomagnets – starting with squares and square-like shapes – and characterized their anisotropy profiles using a MOKE magnetometer configured to perform modulated field magneto-optic anisometry (MFMA) measurements. The center-to-center spacing between nanomagnets is 600 nm. The in-plane dimensions of the nanomagnets are 100 nm x 100 nm, and the thickness of the magnetic layer was varied from 10-15 nm. A scanning electron micrograph of a typical finished array is shown in Fig. 6.2. To take MFMA measurements, we follow a procedure similar to Cowburn *et al.* [41]. We apply a DC magnetic field of 40 mT in the plane of the array to orient the magnets along an angle θ and simultaneously apply a small AC field at 10 Hz in the transverse direction. We then measure the AC magneto-optical response with a MOKE magnetometer using a lock-in technique. The output voltage from the lock-in amplifier, χ_M, is related to the transverse susceptibility, χ_T, and the anisotropy field, H_{anis}, by the equation:

$$\chi_M^{-1} \propto \chi_T^{-1} = \frac{H_{anis} + H}{M_S} \tag{6.1}$$

where H is the strength of the applied DC field and M_S is the saturation magnetization of the nanomagnet. A qualitatively meaningful anisotropy profile is thus obtained by plotting the inverse of χ_M for each angle of the applied DC field. Maxima indicate magnetic easy axes and minima indicate magnetic hard axes.

In Fig. 6.3, we plot the experimentally-obtained anisotropy profiles of both normal square nanomagnets and modified square nanomagnets with concave edges of varying indentation depth and film thickness. In all plots, χ_M^{-1} is multiplied by a normalizing factor. Data was obtained for angles between 0 and 180 degrees and copied between 180 and 360 degrees to produce a complete angular profile. The lobes of the anisotropy profile plots indicate magnetic easy axes. We observe that normal squares have easy axes oriented towards the corners, in agreement with earlier findings, but that concave squares with sufficient concavity depth and thickness have easy axes oriented along the edges. The thickness-dependence of configurational anisotropy has been established previously, but the dependence on concavity depth is a new observation. This verifies the ability to control the direction of magnetic easy axes through small adjustments to a nanomagnet's shape. Our results suggest that concave shapes, in addition to NML applications, may be useful in nanomagnetic devices that require different anisotropy properties in each magnetic element. Often it is only practical to deposit and pattern a single magnetic film, so lithographic control of anisotropy, rather than thickness control, is desirable.

In several shapes measured in Fig. 6.3, e.g. 10 nm concavity depth and 5 nm thickness, the strength of the anisotropy is noticeably weaker than other samples. In subsequent experiments, we quantified the variation of anisotropy strength among the different shapes. To do so, we used the MFMA technique to determine χ_M as a function H, with H oriented along the magnetic hard axis. As established by Cowburn *et al.* [45], the peak value of the χ_M-H plot occurs when H is equal to the hard-axis anisotropy field. In Fig. 6.4 (a) we plot χ_M-H for three of shapes in Fig. 6.3. The anisotropy field for each shape, determined by the locations of the maxima of the fitted curves, is plotted in Fig. 6.4 (b) (the anisotropy field is taken to be negative when the hard axis is oriented along 45°). The anisotropy field is observed to be a monotonic and nearly linear function of concavity depth for each thickness

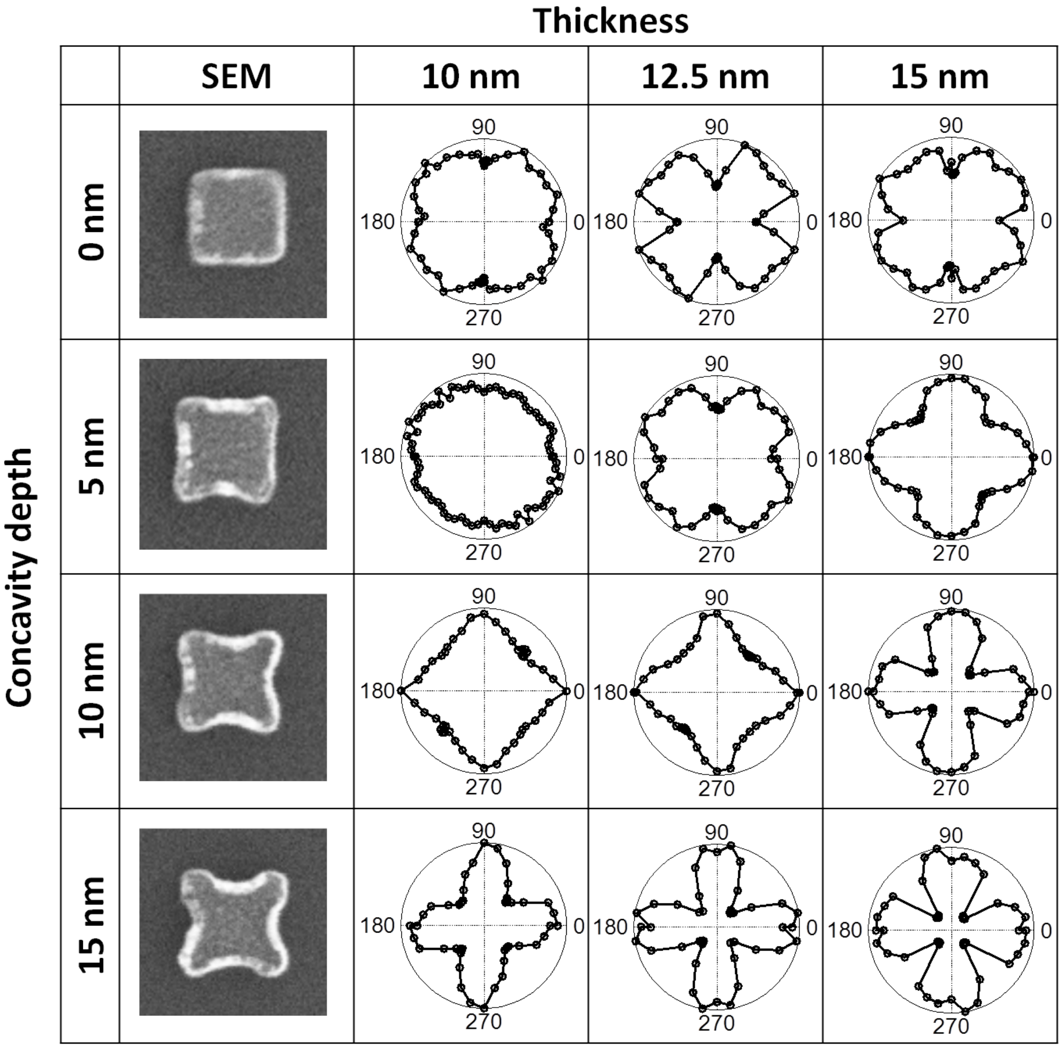

Figure 6.3: Scanning electron micrographs and anisotropy profiles of nanomagnet squares with concavities of varying depths and film thicknesses. The edge length of the squares is 100 nm.

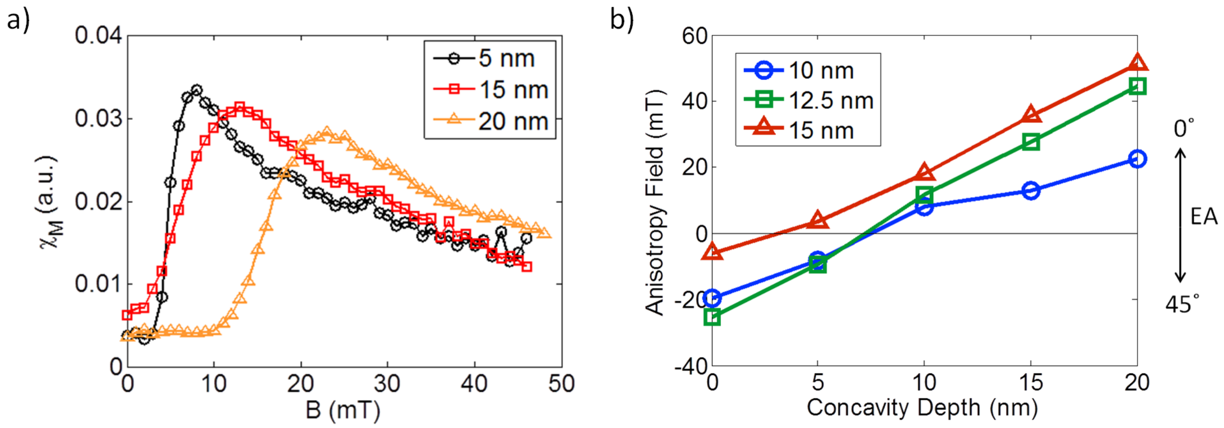

Figure 6.4: Selected examples of χ_M-H curves measured along the hard axes of the 10 nm thick magnets in Fig. 6.3. The location of the peak gives the anisotropy field, plotted in (b). (b) H_{anis} as a function of concavity depth and film thickness in concave nanomagnet squares.

we tested. The trend remains strong up to about 50 mT, the maximum magnetic field that could be tested in our apparatus. These trends indicate that concave shape engineering gives widely-tunable yet predictable control of nanomagnet behavior.

Concave triangles Control of configurational anisotropy using concave shapes is not limited to squares. To illustrate this point, we conducted a similar study of the anisotropy properties of triangular nanomagnets. Energy efficient digital logic devices based on triangular nanomagnets have been proposed and are one application that could benefit from tunable anisotropy control [51]. We studied nanomagnets with equilateral triangle shapes with base lengths of 120 nm. In Fig. 6.5, we show SEM images and corresponding anisotropy profiles of a simple triangle shape and a concave triangle shape. The concavity depth is 20 nm. The anisotropy profile shows that in a simple triangle, the easy axes lie along the edges of the triangle, consistent with previous measurements, while in concave triangles the easy axes are perpendicular to the edges. This result verifies that the use of concavities to modulate the anisotropy properties of nanomagnets can be broadly applicable to a variety of shapes.

6.4 Discussion

Constructing useful information processing devices from nanomagnets requires broad control over their anisotropy properties, especially as they grow in sophistication beyond early-stage research and proof-of-concept experiments. However, relatively few options exist for anisotropy control at the nanoscale, and many of them are weighted down by crucial lim-

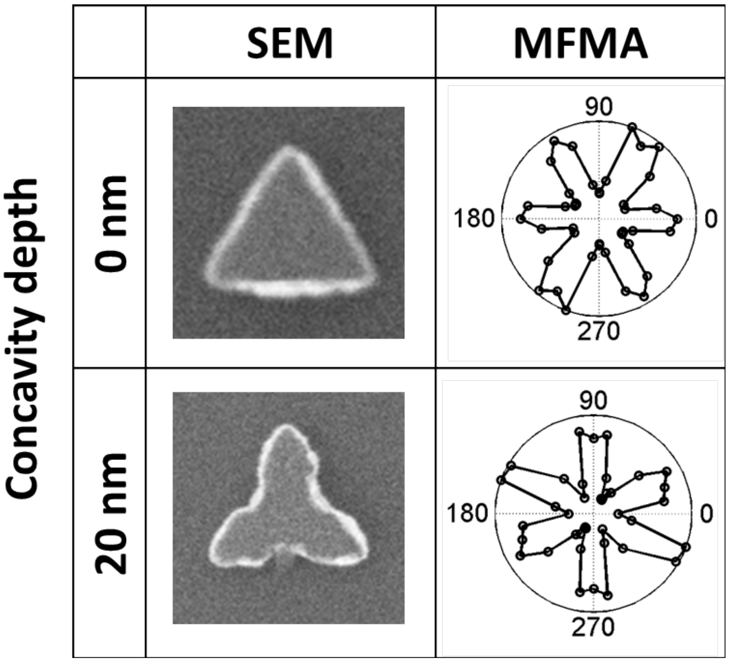

Figure 6.5: Scanning electron micrographs and anisotropy profile of triangular nanomagnets with and without concave edges. The base length of the triangles is 120 nm.

itations. Our investigation of nanomagnets with concave edge profiles is intended to be a starting point for continued exploration of the shape space of nanomagnets in search of useful anisotropy properties. Applications need not be confined to memory and computing devices. For example, magnetic sensors and biological technologies may also be able to harness concave shaped nanomagnets for their uniquely tunable anisotropy properties. We suggest using techniques similar to the ones described in this chapter to predict and analyze the behavior of such nanomagnets. For example, in the next chapter, we apply some of these techniques to study nanomagnets suitable for NML applications.

Chapter 7

Improving the Reliability of Nanomagnetic Logic

7.1 Concave Nanomagnets in Nanomagnetic Logic Applications

In Chapter 5, we established that the soliton mode of operation offers a pathway to highly reliable NML devices in the face of imperfect fabrication capabilities. In chapter 6, we established that configurational anisotropy in concave nanomagnets can be used to manipulate the energy landscape of nanomagnets in the manner required to achieve the soliton mode of operation. Here, we tie these two concepts together and design NML devices using concave nanomagnets that operate in the soliton mode [42]. Using micromagnetic simulations and experiments, we verify the functionality of our devices and show improvements in reliability relative to devices operating in the adiabatic mode.

The modification we propose to induce the desired anisotropy properties in nanomagnets for soliton-mode NML applications is illustrated in Fig. 7.1. The shape resembles a rectangle with concavities along its two short edges (top and bottom). The size and thickness of the nanomagnet can otherwise be comparable to nanomagnets that have been previously studied in NML applications. We expect the subdomain magnetization state in the concave shape to adopt a stable inwardly bowed configuration when magnetized along the horizontal axis. This is in contrast with what we would expect in a rectangle without concavities or an ellipse shaped nanomagnet, which we know to be unstable when magnetized along the horizontal axis. In order to induce the soliton mode of signal transmission, the shape anisotropy arising from the elongated vertical axis of the nanomagnet should be tuned in relation to the configurational anisotropy arising from the concavities.

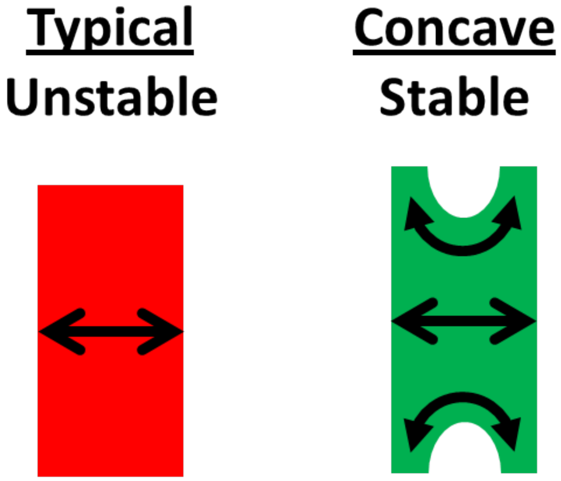

Figure 7.1: Illustration of the geometry of a concave nanomagnet in comparison to a typical rectangular nanomagnet. While the rectangular nanomagnet is unstable when magnetized along the short axis, the concave nanomagnet adopts and outwardly bowed configuration that induces stability.

7.2 Simulation Study of Concave Nanomagnets

Micromagnetic simulations were carried out to verify the configurational anisotropy properties of the concave rectangle. The effect of configurational anisotropy cannot be simulated using the single-spin approximation because the subdomain magnetization of the nanomagnets play a fundamental role in their behavior. Therefore, the simulation studies were carried out using OOMMF. The running time of OOMMF simulations is substantially longer than single spin simulations, so we have not conducted detailed parametric studies of the reliability of concave nanomagnets as we did for ellipse-shaped nanoamagnets in Chapter 5. Future work employing computer clusters optimized for running large numbers of simulations in parallel is planned in order to address this deficiency.

We initially use micromagnetic simulations to observe the behavior and anisotropy properties of isolated concave nanomagnets. Three approaches are used, each one being applied to both a concave nanomagnet and an ellipse-shaped nanomagnet as a control. First, we measure a hysteresis loop along the horizontal axis of the nanomagnets. An open hysteresis loop with a nonzero remanent magnetization indicates the desired response to a clocking field applied along the horizontal axis. In Fig. 7.2 (a), the concave nanomagnet demonstrates hysteresis along the horizontal axis while the ellipse nanomagnet does not. Second, we calculate the anisotropy profile of the nanomagnets to confirm that the concave nanomagnet has two easy axes offset by 90° from one another. Fig. 7.2 (b) confirms that the concave nanomagnet has a dominant easy axis along the shape easy axis and a minor easy axis along the shape hard axis. The ellipse nanomagnet has only one easy axis in the elongated direction.

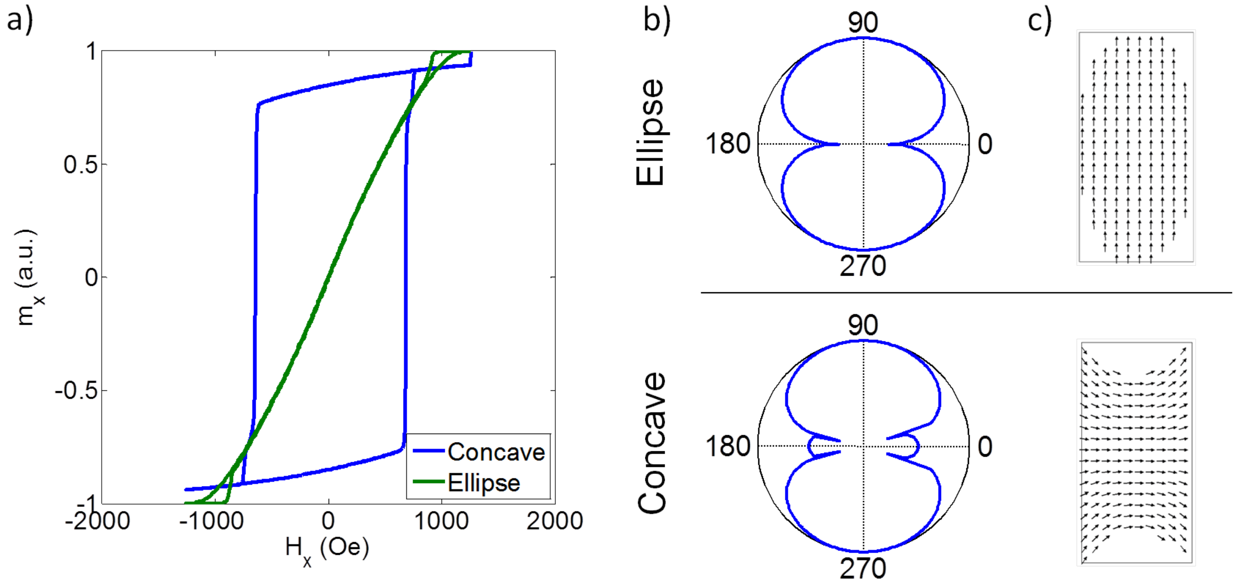

Figure 7.2: Micromagnetic simulations that verify the desired anisotropy properties of concave nanomagnets for NML applications. (a) Hysteresis loops taken along the horizontal axis of the nanomagnets. (b) Anisotropy profile of the nanomagnets. (c) Zero-field magnetization state after applying and removing a clocking field along the horizontal axis of the nanomagnets.

Finally, we observe the magnetization state of the nanomagnets in the absence of magnetic fields after being initially magnetized along their horizontal axis. In Fig. 7.2 (c), we confirm that the concave nanomagnet adopts an inwardly bowed magnetization configuration that is stable along the horizontal axis, whereas the ellipse nanomagnet is not stable along the horizontal axis.

Our next set of simulations addresses chains of concave nanomagnets, and the intention is to verify that the soliton mode of signal propagation occurs. For comparison, we also simulated a chain of ellipse-shaped nanomagnets with equivalent dimensions. Screen captures from the simulations are shown in Fig. 7.3 (a). In both simulations, the leftmost magnet is fixed in the vertical direction to set the desired output state of the chain, and the rightmost magnet is fixed to the right to stabilize the terminal magnet. The nanomagnets are initialized along the horizontal axis by an applied magnetic field of 150 mT, which is removed linearly over the first 1 ns of simulation time to initialize signal propagation. The temperature parameter in the simulations is set to 300 K. Each concave nanomagnet remains magnetized in its metastable state along the horizontal axis until its nearest neighbor flips and produces a dipole field in the vertical direction, giving rise to the predicted cascade-like behavior. By contrast, in the ellipsoidal chains, stochastic thermal processes caused the nanomagnets to flip to the vertical axis too rapidly for the information from the input magnet to propagate

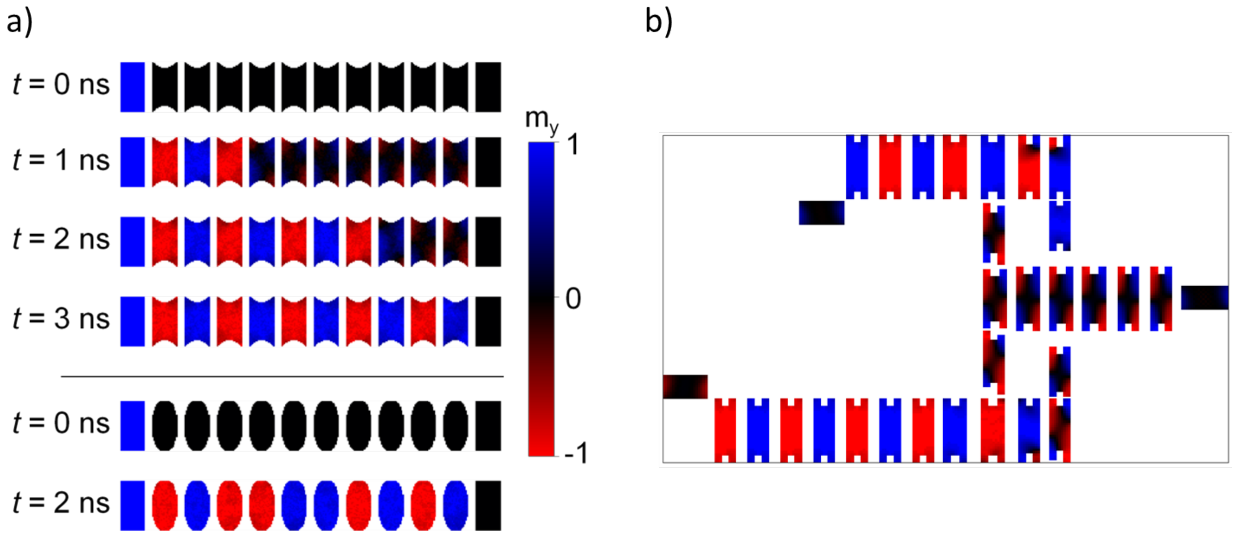

Figure 7.3: (a) Micromagnetic simulations showing cascade-like signal propagation in a chain of concave nanomagnets (top) and error-prone signal propagation in a chain of normal nanomagnets (bottom). (b) Signal propagation in a concave nanomagnet device with square features.

reliably down the chain. As a result, some of the magnets flip to a logically incorrect state (parallel to their nearest neighbors).

In all of the micromagnetic simulations discussed above, the concave rectangular nanomagnet consists of concave edges that terminate in fine points. Such geometric features are not able to be patterned reliably using electron beam lithography. To make sure that this experimental limitation would not hinder the real-world performance of concave nanomagnet NML circuits, we conducted similar simulations on concave nanomagnets with square and edges whose minimum feature sizes were within our lithography capabilities. In all cases, similar behavior and performance to the shapes with pointed features was observed, as exemplified by the device in Fig. 7.3 (b).

7.3 Experimental Verification

Our next step in this investigation was to carry out experiments confirming the simulation data presented in the previous section. In correspondence with the simulation data, four experiments were carried out: (1) Measurement of hysteresis loops along nanomagnet hard axis; (2) Measurement of anisotropy profile of concave nanomagnets; (3) Observation of subdomain magnetization configuration of concave nanomagnets; and (4) observation of soliton signal propagation in concave nanomagnet chains. Additionally, we were able to experimentally collect data on the reliability of concave nanomagnet chains in comparison

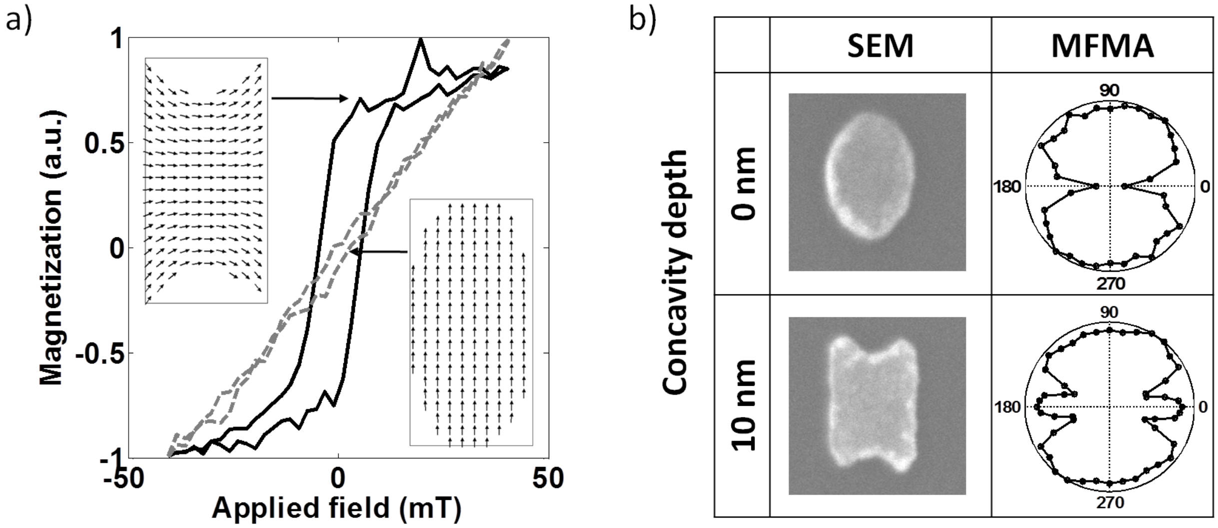

Figure 7.4: (a) Comparison of hysteresis loops measured along the hard axis of concave and ellipsoidal nanomagnets by MOKE magnetometry. (b) Scanning electron micrographs and anisotropy profiles of ellipse- and concave rectangular nanomagnets for use in nanomagnetic logic. The nanomagnet dimensions are 80 nm x 120 nm

to ellipse chains.

The first two experiments require us to measure the magnetization of isolated nanomagnets under the influence of a magnetic field. The MOKE technique is well-suited to this task. Therefore, for these experiments we fabricated large arrays of concave and ellipse shaped nanomagnets and measured their average properties by MOKE. The dimensions of the nanomagnets are 80 nm x 120 nm with 10 nm thickness. In the concave nanomagnet, the depth of the concavity is 10 nm. The concavity shape that was defined in the electron beam lithography mask had square edges as opposed to the pointed features shown in the simulation results.

First, we measured the hysteresis loop of the arrays, applying a field along the horizontal (short) axis of the nanomagnets and measuring the MOKE response along the same axis. The results are shown in Fig. 7.4 (a). As in the simulation data, we observe hysteresis in the concave nanomagnet array but overlapping curves in the ellipse nanomagnet array. In the hysteresis curve for the concave nanomagnets, the fact that the transitions from the positive to negative magnetization states are not abrupt indicates that there are lithographic variations among the magnets in the array. The soliton mode of signal transmission must be robust enough to overcome this nonuniformity to transmit information reliably.

Next, we conducted MFMA measurements to determine the anisotropy profile of concave nanomagnets in comparison with ellipse nanomagnets. The procedure used is the same as the one described in the previous chapter. In Fig. 7.4 (b), we compare the experimental anisotropy profile of a concave rectangle with that of an ellipse. In both ellipses and concave

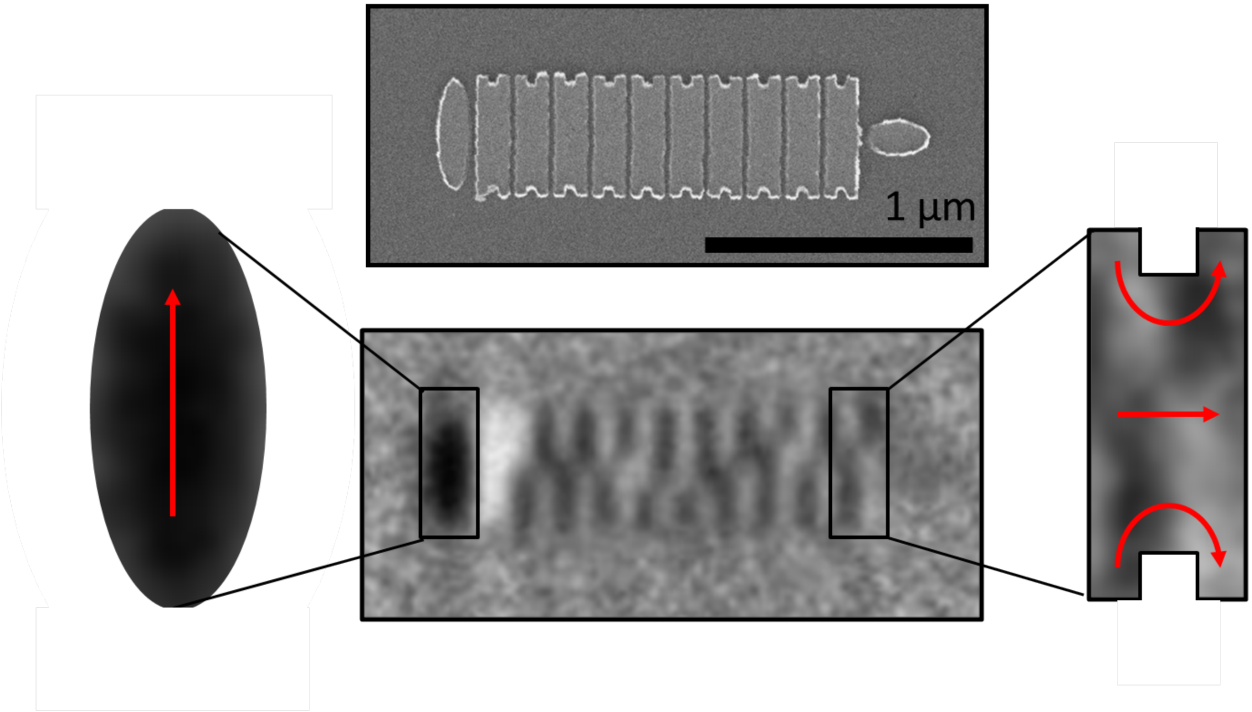

Figure 7.5: Scanning electron (top) and magnetic contrast (bottom) images of a chain of concave nanomagnets. The insets compare the observed magnetization state of the ellipse shaped input nanomagnet, which is magnetized up, and a concave nanomagnet, which adopts an inwardly-bowed configuration that is magnetized to the right.

rectangles, we clearly observe a dominant shape easy axis in the vertical direction, but only in the concave rectangle do we additionally observe a minor easy axis in the horizontal direction. These results correspond qualitatively to the simulation data in Fig. 7.4 (b).

Magnetic contrast imaging of concave nanomagnet chains was carried out using the PEEM technique. Many of the factors that were taken into account during the design of the experiment were similar to those encountered when verifying the adiabatic mode of signal transmission in chains of ellipse nanomagnets. Namely, it was crucial that the microscopy process did not disturb the state of the nanomagnets, ruling out the MFM technique. Because we use PEEM, we again face the experimental limitation of not being able to apply a clocking field to the sample while it is in the chamber. Furthermore, unlike the adiabatic mode, in which the random walk occurs continuously over time, the soliton mode dynamics occur only once per clocking cycle. Once the magnets flip to the easy axis, the only way to induce the signal cascade is to clock the magnets again.

To overcome these challenges, we fabricated chains consisting of nanomagnets with a wide range of aspect ratios. The aspect ratios include some chains in which the magnets had insufficient shape anisotropy to overcome the configurational anisotropy barrier and flip to the vertical axis after the application of a clocking field. When we image these chains in

PEEM after clocking, we observe them initially in the 'locked-up' state in which configurational anisotropy pins the concave nanomagnets along the horizontal axis. We then increase the temperature of the sample to deliver the energy needed to overcome the configurational anisotropy contribution to the potential barrier and induce the soliton behavior.

The sample we fabricated consisted of chains of nanomagnets with a width of 150 nm, concavity depth of 50 nm, and height that varied from 300 to 450 nm. The leftmost nanomagnet was ellipse-shaped, causing it to flip to the vertical axis as soon as the clocking field was removed to initiate signal transmission. As a control, chains of elliptical shaped nanomagnets with similar dimensions were also included. The in-plane dimensions of the nanomagnets were significantly larger than many of the nanomagnetic devices studied previously. This was done to reduce the sensitivity to lithographic variations, which caused concave nanomagnet chains with smaller critical dimensions to fail to exhibit the expected soliton behavior with low error rates. Prior to inserting the sample into the PEEM chamber, a clocking magnetic field of 2200 Oe was applied along the horizontal axis of the magnet chains. A scanning electron micrograph of a typical chain of concave nanomagnets is shown in the upper image of Fig. 7.5.

Initially, magnetic contrast images were taken with the sample stage at room temperature. The lower image of Fig. 7.5 is an example of a PEEM image of a nanomagnet chain whose shape anisotropy is too low for the signal to propagate at room temperature. On the left side of the chain, we observe the ellipse shaped input nanomagnet oriented in a uniform vertical magnetization state, which shows up as solid black in a PEEM image. This is as we expect in the absence of a clocking field along its horizontal axis. On the other hand, the zipper-like pattern to the right of the input nanomagnet indicates that the concave nanomagets are oriented along the horizontal axis. Closer examination of a single concave nanomagnet, shown in the inset on the right of Fig. 7.5, reveals that the zero-field magnetization state of the magnet is the inwardly bowed configuration predicted by micromagnetic simulations, in Fig. 7.2 (c).

After capturing images at room temperature, we raised the temperature of the sample stage to 120° C in order to initiate soliton dynamics. We then captured a time-lapse series of PEEM images of the heated sample over a period of several hours. As shown in Fig. 7.6, we observed, one-by-one, the process of cascade-like signal propagation in a chain of nanomagnets. The time required to capture PEEM images limits the observable signal transmission speed to minutes or hours. However, we observe in micromagnetic simulations that it is possible to engineer concave nanomagnets in which signal propagation occurs on a sub-nanosecond time scale, as in Fig. 7.3. Our results represent the first experimental observation of cascade-like signal propagation NML using nanomagnets with biaxial anisotropy. Next steps include carrying out ultrafast measurements to explore sub-nanosecond signal transmission in NML chains as well as the implementation of logic gates and circuits.

Fig. 7.7 shows error statistics as a function of nanomagnet aspect ratio for both concave and ellipse nanomagnet chains. The value we plot is average transmission distance, defined as the average number of error-free magnets starting from the input before the first error in a chain is encountered. The length of each chain is 10 magnets, which sets a maximum possible

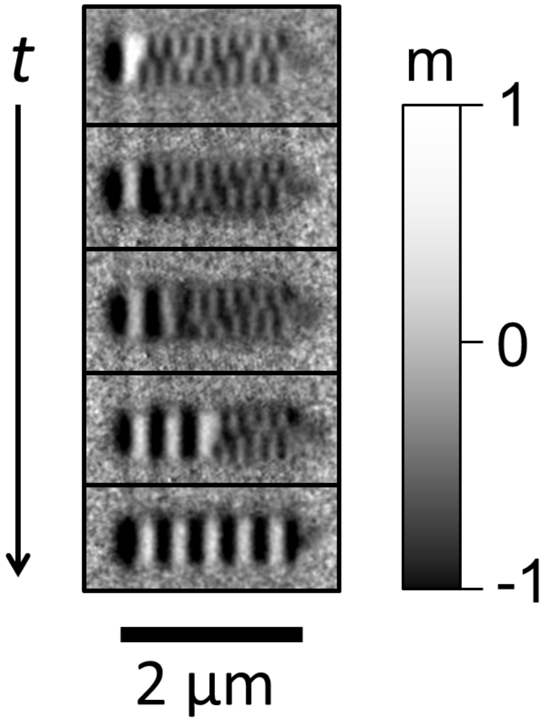

Figure 7.6: Time-lapse magnetic contrast images with the sample heated to 120° C. Over the course of several hours, cascade-like signal propagation occurs from left to right as concave nanomagnets flip from the horizontal axis to the vertical axis when perturbed by their leftmost neighbors.

transmission distance. The transmission distance is averaged over 14 chains of similar aspect ratio. For the concave nanomagnet chains, low aspect ratio chains do not transmit data at all (average transmission distance is zero), but high aspect ratio nanomagnets transmit data nearly nine out of 10 magnets on average, with further improvement expected for higher aspect ratios. The control elliptical shaped nanomagnets, transmit error-free data only about 3-6 magnets for all aspect ratio.

7.4 Discussion

In the last two chapters, we have conducted a detailed investigation to understand the impact of shape on configurational anisotropy in nanomagnets. Our focus has been on nanomagnets with concave geometries, in which we discover that small variations in parameters such as concavity depth result in large and predictable changes in the direction and strength of magnetic easy axes. Concave shapes derived from squares and triangles were examined

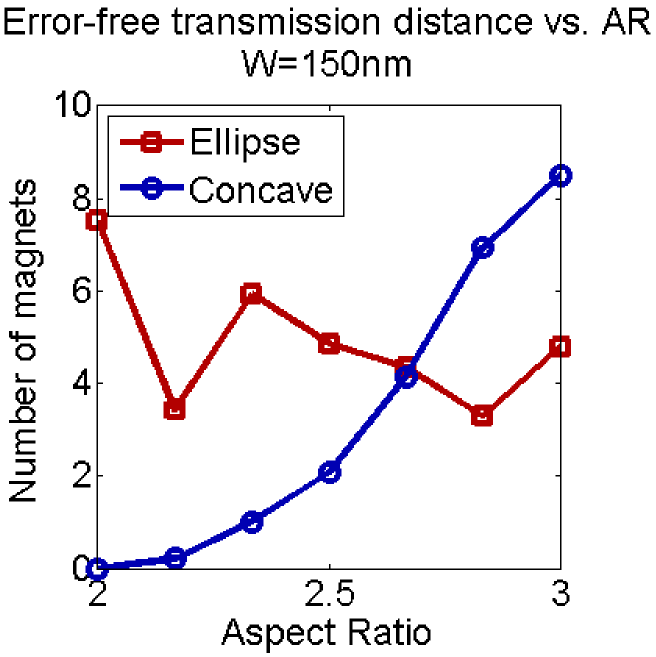

Figure 7.7: Signal transmission distance as a function of aspect ratio observed in a PEEM experiment. Each data point is the average transmission distance of 14 nanomagnet chains.

by MOKE microscopy, and we found a nearly linear increase in anisotropy strength with increasing concavity depth. We also designed a concave shape derived from a rectangle for use in nanomagnetic logic applications and experimentally demonstrated a method for improving the reliability of NML. It bears mentioning that NML is one of many possible applications of concave nanomagnets. Future work should seek to identify new applications that would benefit from the unique top-down control provided by configurational anisotropy in concave nanomagnets.

Chapter 8

Conclusion

8.1 NML: Addressing Societal Needs Through Innovation

The spread of information technology in the latter half of the 20th century has coincided with a period of economic growth throughout much of the globe. Many sectors have directly benefited from the efficiencies made possible by the use of information technology. For example, in transportation, computer-aided design and robotic manufacturing have led to the availability of increasingly fuel-efficient, safe, comfortable, and low-cost automobiles. Many other industries have either been transformed (e.g. entertainment) or created from scratch (e.g. software) since the start of the digital age. Notably, the adoption of computing technologies has not been limited to wealthy parts of the world, especially mobile communication devices. Still, it can be argued that we have so far only scratched the surface of realizing the benefits of living in an era of abundant information.

Continued progress in information technology will be tied largely to improvements in the performance and cost of microelectronic components. The longstanding trend of exponential improvements in conventional semiconductor electronics are due to end in the next decade. Beyond this threshold, new physical operating principles are needed to increase the speed, density, and energy efficiency of computing devices. It is likely that a successful solution will rely on physics that occur uniquely at the nanoscale, where many open-ended questions remain and opportunities lie.

The research presented in this dissertation focused on harnessing nanoscale magnetic phenomena for next-generation computing applications. In particular, the NML device architecture served as a starting point for studying the interactions between nanomagnetic bits on a chip. In Chapters 2 and 3, we showed that NML and magnetic memory devices can be used to make experimental contact with the thermodynamic limits of computation. While primarily a fundamental result, the push to develop energy efficient electronic products has become so strong so fast that there may soon be opportunities for practical applications of this research. In Chapters 4 to 7, we explored the dynamics of signal transmission in

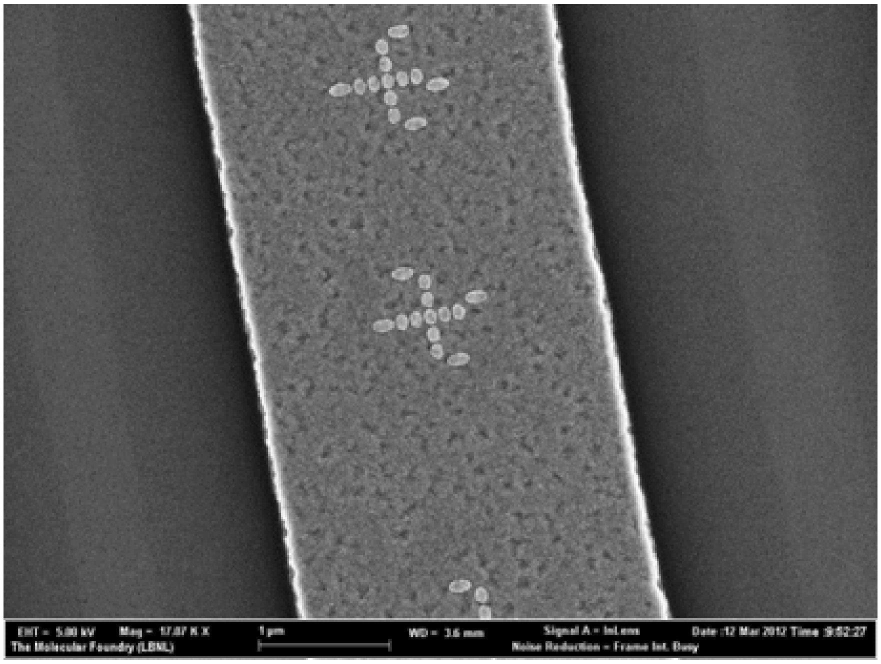

Figure 8.1: Scanning electron micrograph showing an MLG patterned on top of a copper wire for ultra-fast clocking experiments.

NML circuits and developed ways to improve on speed and reliability metrics. Significant progress has been made by first identifying the direction that NML must go in order to achieve long-term success and then by introducing specific design modifications that help us to get there.

8.2 Next Steps

Several of the experiments carried out in this dissertation suggest clear opportunities for follow-up research projects. For example, after our experimental investigation of Landauer erasure in nanomagnets, one of the next steps is to expand the devices under testing from arrays of isolated bits to mult-bit logic circuits that may address a broader portion of the theoretical thermodynamic limits of computation. Similarly, many of the studies of signal transmission in NML focused on simple chains of nanomagnets; it may be possible to gain greater insight from the experimental analysis of more complex logic circuits. Both simulations and experiments relating to combinatorial logic circuits, starting with MLG's and B-gates, should be fruitful.

The study of signal transmission in NML was also limited in the variety of clock waveforms that were tested. In particular, the clock field in all of our experiments was applied using an external magnet with a very slow rise and fall time – up to 30 seconds. Applying the clocking field at this time scale does not necessarily yield the same results as a more practical time scale for clocking NML, which is on the order of hundreds of picoseconds for GHz-scale operating frequencies. To address this gap in our experimental capabilities, we designed and prototyped NML circuits with on-chip clocking circuitry. The clocking circuitry consists of current-carrying wires that induce a localized magnetic field when injected with a current pulse. Fig. 8.1 shows a completed device. A near-term goal is to carry out statistical studies and image the signal transmission dynamics of NML devices clocked at the ultrafast time scale.

Addressing the medium term future, mechanisms for the voltage control of nanomagnetism are currently being studied in the context of NML. To date, the clocking force used in NML studies has been the Oersted fields generated by electric currents. While convenient, current flow leads to resistive heating and less than ideal energy efficiency. Voltage control of the clocking force, which from a circuit perspective is equivalent to charging and discharging a capacitor, can be accomplished much more energy efficiently. There are several approaches to coupling voltage and magnetism that are under investigation. For example, a class of materials called multiferroics, the most widely known of which is $BiFeO_3$ [52], have both magnetic and electronic ordering that are correlated with one another. Alternatively, composite multiferroics combine a material with electronic ordering with a material with magnetic ordering such that they couple at their interface [53]. Other approaches do not seek to eliminate the need for electronic currents entirely but rather reduce the required current, an example being the spin transfer torque effect [54, 24].

Like conventional computing components, the long-term prospects for NML and related devices will benefit from the progression to smaller size scales and faster time scales. At the ultimate size limit, single electronic spins may be used to replace nanomagnets in the NML architecture. One possible materials system that can serve as a platform for single-spin NML is diamond, in which nitrogen vacancies behave as single spins with a very long coherence time [55]. The ultimate performance of NML was initially thought to be limited by the precessional frequency of nanomagnets, which is on the order of GHz; however, recent experiments have shown the ability to flip nanomagnets on a sub-picosecond time scale using optical pulses [56]. Exploration of this regime of nanomagnet dynamics may uncover practical methods for achieving performance comparable to or superior to electronic computers. Overall, the long-term success of NML will require a number of still unanswered questions to yield positive answers, but the need to overcome these hurdles should not hold back future efforts to unlock the value that NML can uniquely bring to the next-generation of computing devices.

Appendix A

Nanomagnetic device fabrication

The deposition and patterning of magnetic materials is, in many cases, not unlike the deposition and patterning of normal materials. As a result, our fabrication process for nanomagnetic devices relied primarily on techniques that are in widespread use in the nanoscience community. One process flow in particular – electron beam lithography followed by electron beam evaporation and lift-off – was used to fabricate the majority of the samples described in this dissertation. Upon completion of device fabrication, the quality of our structures was checked by scanning electron microscopy (SEM) or, in a few cases, atomic force microscopy (AFM). This process flow was selected primarily for its convenience and reliability; other possible approaches, such as etching nanostructures, involve many process steps and do not reliably produce devices on the small size scale of nanomagnetic logic without significant process development. The elements of our typical process flow are depicted in Fig. A.1.

Electron beam lithography Electron beam lithography is the technique we used to transfer computer-generated patterns with nanometer-scale features to a flat substrate. We prepared mask files for nanomagnetic devices using automation software to facilitate the generation of repeated shapes with variable dimensions. Automation was essential because a typical nanomagnet sample consisted of hundreds or thousands of similar devices with small variations in size or shape. This file was then printed by an electron beam writer onto a silicon substrate coated with polymethyl-methacrylate (PMMA) resist. In most cases, the tool we used was a Vistec VB300 100 kV System located at the Molecular Foundry, Lawrence Berkeley National Laboratory. The exposed resist was developed in a solution of 7:3 isopropanol:water at -5° C. PMMA is a positive photoresist, as required for the liftoff process that follows. Feature sizes down to about 20-30 nm were reliably transferred using this patterning method.

Electron beam evaporation Electron beam evaporation is a physical vapor deposition method in which a crucible containing purified metal is heated to a temperature that causes the metal to evaporate at an appreciable rate. The evaporated metal then passes through a vacuum chamber and deposits in a thin film onto the surface of a sample. A crystal monitor,

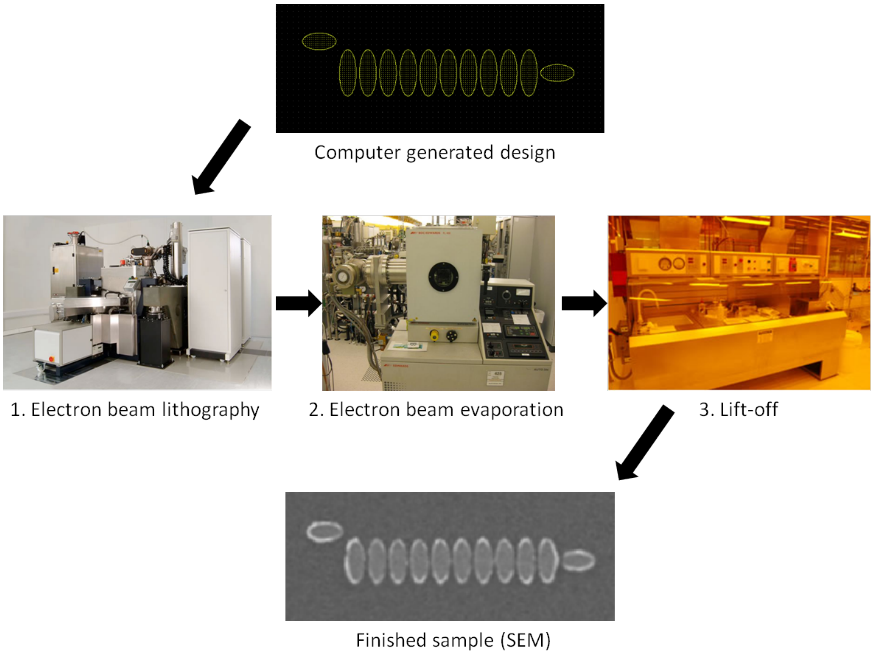

Figure A.1: Typical process used to fabricate nanomagnetic devices

whose resonance frequency shifts as metal deposits onto its surface, is positioned near the sample and is used to detect how much metal has been deposited over time. This technique allows for metal layers of a precise thickness and relatively good uniformity to be deposited onto a sample. The key advantage of electron beam evaporation over other deposition techniques, such as sputtering, is that the films are deposited in an anisotropic manner which facilitates high quality liftoffs. A typical nanomagnetic device requires three metal layers to be deposited. The first is titanium, about 5 nm thick, which serves as an adhesion layer between the silicon substrate (which is coated with a thin native oxide) and the magnetic metal. The next layer is the magnetic metal, usually permalloy, and last is a capping metal such as aluminum that prevents the magnetic material from oxidizing once removed from the vacuum chamber. The three metals are deposited sequentially without breaking vacuum, so we expect the interfaces to be largely free of contamination. The evaporated metal films are polycrystalline, which is significant for magnetic materials because it ensures that the impact of magnetocrystalline anisotropy is minimized.

Lift-off The last step of the fabrication process is to place the patterned sample covered in a metal film into a chemical solution to remove the PMMA photoresist. Typically, the chemical solution is PG Remover, which consists of n-methylpyrollidone and surfactants, heated to about 70° C. After about 15 minutes, most of the PMMA dissolves, lifting off the metal layers that were deposited on top of it. Only the exposed areas of the resist i.e. the nanomagnet patterns remain. The sample is then briefly placed into an ultrasonic bath to remove residual PMMA and other surface contaminants. Finally, the sample is removed from the heated PG Remover, rinsed with isopropanol, and blown dry with an N2 gun. A scanning electron microscope, in most cases a Zeiss Ultra60 FE-SEM located at the Molecular Foundry, is then used to image the surface of the sample and verify the quality of the devices.

Appendix B

Nanocharacterization: MOKE and PEEM

B.1 MOKE

Background

When a beam of polarized light is reflected from a magnetized surface, the polarization of the reflected beam is slightly rotated and elliptical relative to the incident beam. This effect is known as the magneto-optical Kerr effect (MOKE). While the effect is typically very small, the use of high quality components such as prism-based polarizers and photoelastic modulators in the optical apparatus makes sensitive measurements by MOKE possible. For our experiments, we built a multifunctional MOKE apparatus to characterize the magnetic nanostructures used in nanomagnetic logic.

The magneto-optical Kerr effect arises from spin-orbit coupling between conduction electrons and fixed spins in a magnetic material. When illuminated by polarized light, the conduction electrons oscillate along the axis of polarization and reflect a portion of the light. In a non-magnetic, non-birefringent material, the reflected light has the same polarization as the incident light. However, if the conduction electrons undergo spin-dependent scattering during their oscillation, as they do in a magnetic material, a polarization component orthogonal to the incident polarization angle may be induced. The orthogonal component is not, in general, in phase with the incident light, and therefore the reflected light has a polarization that is both offset from and elliptical relative to the incident linearly polarized light. These changes - the Kerr rotation and Kerr ellipticity - are what is measured by a MOKE apparatus.

The axis of MOKE sensitivity is determined by the polarization angle of the incident light and the angle of incidence relative to the sample. In polar MOKE, the axis of sensitivity is in the out-of-plane axis of the magnetic sample. To obtain maximum sensitivity, the light should arrive at normal incidence and can have an arbitrary polarization angle. In longitudinal and transverse MOKE, the in-plane magnetization of a sample is measured. Longitudinal

MOKE requires the plane of incidence and the polarization of the light to be perpendicular to one another, whereas in transverse MOKE they are parallel. Longitudinal MOKE is better suited for sensitive measurements of in-plane magnetic films than transversal MOKE because it results in a change in the polarization of the light, whereas transverse MOKE results in only a change in reflectivity. Therefore, our apparatus is designed to measure longitudinal MOKE.

Pioneering work on the use of longitudinal MOKE for the investigation of magnetic nanostructures was carried out by Cowburn *et al.* in the late 1990s [41, 45, 57]. In order to use MOKE to investigate magnetic nanostructures, an apparatus is constructed to focus laser light on to arrays of identical nanomagnets. Because each nanomagnet is smaller than the diffraction limited spot size of the laser beam, the measured Kerr rotation is a function of the average magnetization of the array. By applying an oscillating magnetic field to the sample along the axis of MOKE sensitivity, the hysteresis properties of nanomagnets can be measured. This is useful for characterizing the magnetic response of nanomagnets as well as calculating the energy transferred from the magnetic field to the nanomagnets, which is given by the area of the hysteresis curve. The design of a nano-MOKE apparatus is shown in Fig. B.1 (a).

For noise reduction in optical measurements, a modulator is often used to minimize the effect of low frequency noise. The output of the measurement is then demodulated using a lock-in amplifier that uses the modulator as a reference signal. Because MOKE is a polarization measurement, it is possible to use a photoelastic modulator (PEM) based technique. A PEM is a device in which light passes through a birefringent material with a modulated amount of stress applied one axis. The resulting strain causes the phase of light polarized along one axis to be modulated relative to the unstrained axis. If the incident light is polarized at 45° to the strained axis, and the modulation amplitude is one quarter wavelength of the light, then the light modulates between linearly and circularly polarized light. Incident light which is circularly polarized modulates between 45° and -45° linearly polarized light. Finally, incident light which is linearly polarized directly along either the strained or unstrained axis is not modulated at all. These three permutations and their significances are depicted in Fig. B.1 (b).

Specifications

Optical components The MOKE apparatus we constructed for our experiments is shown in Fig. B.2 (a). The optical path consists of a 632 nm HeNe laser that outputs 8 mW of optical power, a polarizer that is oriented to transmit only the p-polarized component of the incident light, a focusing lens, the magnetic sample, a collimating lens, a photoelastic modulator (PEM), another polarizer oriented at 45° relative to the first polarizer, and a photodetector. The polarizers are Glan-Laser prisms mounted in manual rotation mounts. When crossed, the polarizers have an extinction ratio of nearly 995,238:1. The PEM is a PEM-100 by Hinds Instruments, a 50 kHz modulator with an antireflective coating for 632 nm wavelength light. The modulation amplitude is adjustable through the controller shown

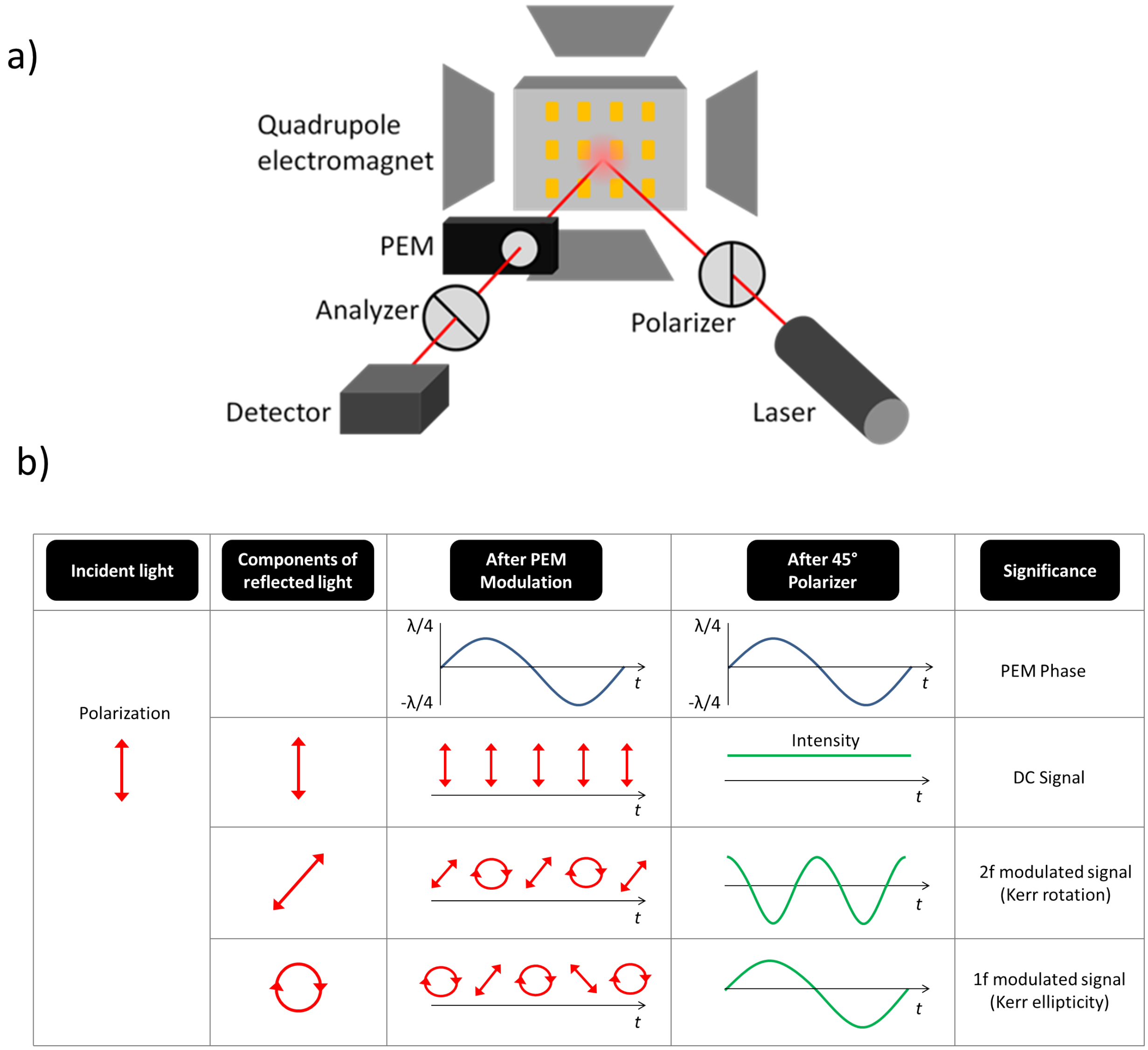

Figure B.1: (a) Diagram of a MOKE apparatus and (b) chart illustrating the dc, 1f, and 2f components of MOKE signal using PEM modulation.

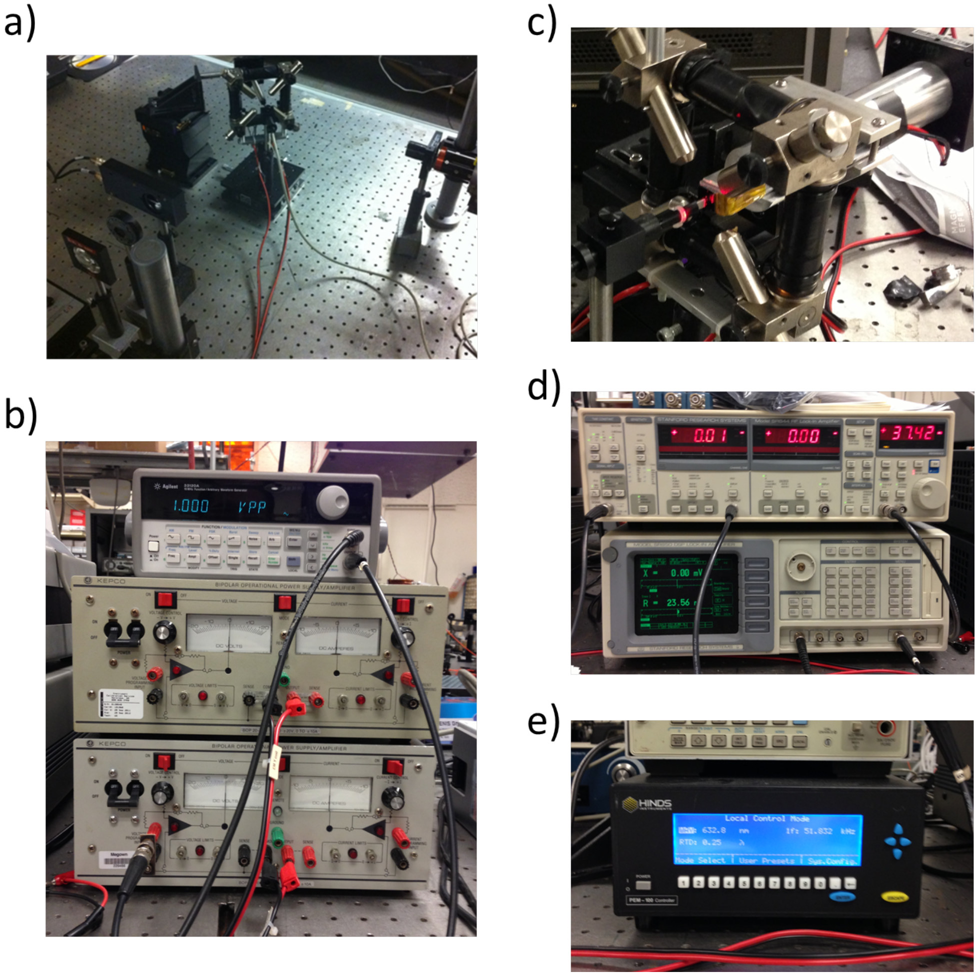

Figure B.2: Photographs of MOKE apparatus (a) overview of optical components, (b) (top) Agilent 33120A waveform generator (middle and bottom) Kepco BOP 20-10 power supplies to drive electromagnet, (c) sample stage comprising a quadrupole electromagnet, heated sample holder, and Hall sensor (d) (top) SR844 RF Lock-in Amplifier and (bottom) SR850 Lock-in amplifier, (e) Hinds PEM-100 controller.

in Fig. B.2 (e) and is set to one quarter wavelength for our experiments. The photodetector is a 125 kHz Nirvana Auto-Balanced Photoreceiver by Newport Instruments operating in ‘SIG’ mode. The reference photodiode remains capped for all experiments, such that only the signal photodiode is active.

Sample stage The sample stage, shown in Fig. B.2 (c), consists of an adjustable sample holder and an electromagnet. The magnet is a quadrupole electromagnet obtained by custom order from Durham Magneto-Optics. The electromagnet has four pole pieces each oriented diagonally in the plane of the sample, forming an open cr

Part I

title

oss in the middle of which the sample is positioned. The magnetic field is controlled by two Kepco BOP 20-10 bipolar current supplies, one of which controls the horizontal component of the magnetic field and the second of which controls the vertical field. In order to apply an oscillating magnetic field along one axis, an Agilent 33120A waveform generator is connected to the voltage control input of one of the BOP sources and set to the desired waveform. These components are shown in Fig. B.2 (b). The magnetic field is measured by a Hall Effect sensor positioned between the pole pieces in the vicinity of the sample and rotated for the desired axis of sensitivity. The maximum strength of the magnetic field that can be applied is limited by the current rating of the conductive coils, 5 A, and the spacing of the adjustable poles. At the closest spacing, the maximum applied field is about 125 mT and at the farthest spacing, the maximum applied field is about 25 mT. The tradeoff for a larger field is that the volume in the center of the poles over which the field is approximately uniform is reduced; the maximum volume is about 1 cubic centimeter and the minimum volume is about 1 cubic millimeter. The sample holder has a flexible construction, but typically the sample is held in place by a rod attached to a stage that offers three axes of manual translation and one axis of rotation. For some experiments, the sample is mounted on a thermoelectric pad that can be heated or cooled upon the application of an electrical current. The temperature is measured by a thermocouple located near the sample. Due to the magnetic fields present in the application, a type E thermocouple must be used. An active feedback system for the temperature control was not constructed; only manual adjustment is used in the current setup.

Electrical signal processing A diagram of the electrical signal processing portion of the MOKE apparatus is shown in Fig. B.3. During data acquisition, the signal voltage output (labeled ‘SIG’) of the Nirvana photoreceiver and the 1f reference signal from the PEM-100 controller are connected to the signal and reference inputs, respectively, of a Stanford Research Systems SR844 Digital RF lock-in amplifier, shown in Fig. B.2 (d). In most cases, the SR844 is used to measure the 1f component of the input waveform, corresponding to the Kerr ellipticity induced by the magnetic sample. Typically, the 1f waveform is a few tens of millivolts in amplitude, compared to a dc intensity of several volts. The settings of the low pass filter built into the SR844 play a key role in minimizing noise in the measurement. For high quality measurements, the settings must be calibrated to block as much high frequency noise as possible without affecting the measured 1f voltage. The settings are selected based on the ramp rate of the magnetic field and the expected shape of the output waveform. For example, measuring a hysteresis curve with a highly rectangular shape in principle requires an infinitely high bandwidth to accurately capture the sharp edges of the curve. In practice, when measuring hysteresis curves, an electromagnet oscillation frequency of 20 mHz and a low-pass filter time constant of 30 ms at 18 dB/oct was found to result in low-noise and accurate curves. When conducting MFMA measurements, which require an electromagnet oscillation frequency of about 10 Hz, the time constant of the filter must be significantly lower, around 0.3 ms.

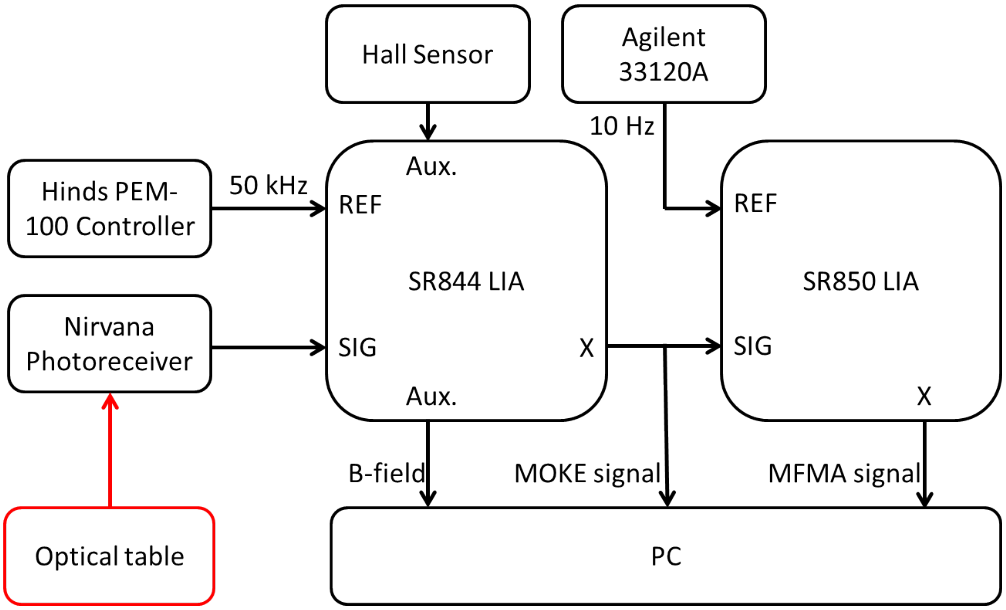

Figure B.3: Diagram of electrical signal processing portion of MOKE apparatus

A second lock-in amplifier is required for the MFMA technique described in the 'Applications' section of this appendix. We used a Stanford Research Systems SR850 DSP lock-in amplifier, the bottom amplifier shown in Fig. B.2 (d). The signal input of the SR850 amplifier is connected to the 'X' output of the SR844 amplifier, and the reference input is connected to the 'Sync' output of the Agilent waveform generator driving the electromagnet. Similar to the SR844, the low-pass filter settings of the SR850 play a large role in the quality of the measurement. In most cases, the necessary bandwidth of the measurement is much lower than the bandwidth required at the first lock-in amplifier, so large time constants e.g. 1 s can be used.

Both lock-in amplifiers are used to measure values that modulate as a function of the applied magnetic field. The field itself must therefore be measured synchronously with the amplifier output. The Hall Effect sensor used to probe the magnetic field outputs a voltage that is proportional to the detected magnetic field by the factor 50 V/T. Originally, the Hall probe output voltage was measured by a LabJack U3 module, and the computer would query the LabJack unit and the lock-in amplifier once per data point. However, even at relatively slow ramp rates, the synchronization provided by this method was insufficient for applications that require a very accurate quantitative measure of the applied field. Instead, we now measure the output voltage of the Hall sensor using the auxiliary input of the SR844 unit, allowing both the field and amplifier voltage to be queried in a truly synchronous manner.

Control software The output voltage from the lock-in amplifier and the Hall sensor voltage are passed to data acquisition software and represented graphically. The software portion of the apparatus is written in LabView. Because the MOKE apparatus is multifunctional, a number of virtual instruments were coded for different tasks. Many virtual instruments share utility functions for tasks such as reading out a magnetic field value and saving data. Specific examples of virtual instruments and their usage are described in the next section.

Noise reduction Between the initial construction of the MOKE apparatus and the present construction of the tool, many improvements were made in order to reduce noise levels during measurement. Most of these improvements were made when carrying out the ultra-high precision experiments described in Chapter 3, and are therefore discussed in detail in that chapter. Considerations included mechanical mounting of optical components, sample design, and electrical signal filtering. Overall, there are a wide range of parameters to optimize, and different experiments frequently require different tradeoffs to be made. Making design choices based on the specifications of the apparatus discussed in this section should serve as a starting point for using the apparatus for future experiments.

Applications

Hysteresis curves One of the simplest and most important uses of MOKE is to characterize the hysteretic behavior of magnetic materials or nanomagnet arrays. The measurement process entails mounting the sample, adjusting the components in the optical path to maximize the dc voltage from the photodiode, and measuring the 1f signal from the lock-in amplifier as a function of applied magnetic field. In measurements that strictly require zero magnetic field oriented in the vertical direction (orthogonal to the axis of MOKE sensitivity), an additional step at the beginning of the measurement is required to demagnetize the poles in the vertical direction. Using the waveform generator to control the BOP source for the vertical coils, an oscillating field is applied that is slowly reduced from a maximum value to zero, typically over a duration of about two minutes. Alternately, the vertical field can be set to a desired fixed field during the hysteresis measurement by applying a dc current to the vertical coils.

The LabView interface for running a hysteresis measurement is shown in Fig. B.4. The program has an optional timer function such that the measurement automatically stops after a fixed duration. It also provides an option for saving data to a user-defined filename. Communication with the SR844 occurs by GPIB, so the GPIB address must also be defined. During the measurement, indicators display the applied field and amplifier voltage as the graph of the hysteresis curve is populated. An averaged hysteresis curve, which helps to reduce much of the measurement noise, can be obtained by post-processing of the saved data.

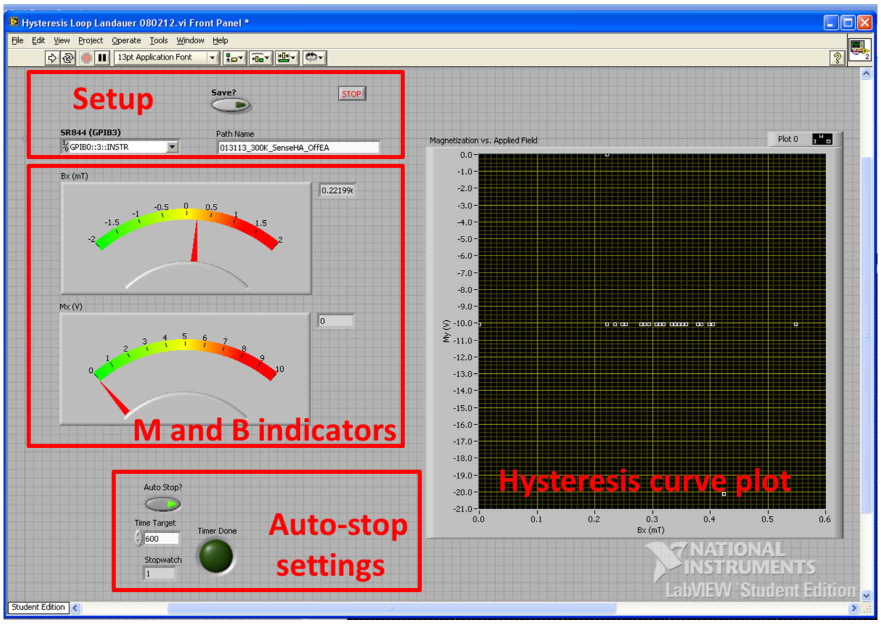

SR844 (GPIB3): GPIB0::3::INSTR
Path Name: 013113_300K_SenseHA_OffEA
Bx (mT): 0.22199
Mx (V): 0
Time Target: 600
Stopwatch: 1

Figure B.4: LabView interface for measuring MOKE hysteresis curves

Polar MOKE Polar MOKE is traditionally carried out with the light source at normal incidence to the sample. However, even in an configuration of the apparatus that is optimized for longitudinal MOKE it is possible to carry out polar MOKE with little modification. The quadrupole magnet merely needs to be rotated such that the oscillating magnetic field is applied out of the plane of the sample. Now, the MOKE signal varies with the out of plane component of the magnetization. The unique diagonally crossed geometry of the quadrupole elecromagnet facilitates rapid switching between longitudinal and polar MOKE measurements by not requiring the sample stage to be rebuilt. The LabView control software for polar MOKE is identical to longitudinal MOKE.

MFMA measurements Modulated field magnetic anisometry (MFMA) is a method for using MOKE to characterize the anisotropy properties of nanomagnets. In this method, the sample is magnetized along a particular axis by a fixed magnetic field and the susceptibility in the transverse direction is measured. The sample is then rotated and the measurement is repeated for different axes. The reasoning behind this method is that if the sample is magnetized along an easy axis, it is stable and has a low susceptibility to applied fields in the orthogonal direction. Conversely, when magnetized along the hard axis, it is unstable and therefore has a high susceptibility. A full anisotropy profile that identifies easy, hard, and locally easy axes of films or nanomagnets can be constructed using this technique.

In MOKE, susceptibility can be measured by using a lock-in technique in which an ac modulating field induces an ac MOKE signal with an amplitude that is proportional to the susceptibility. Typically, the ac field we use is a sinusoidal waveform with a frequency of

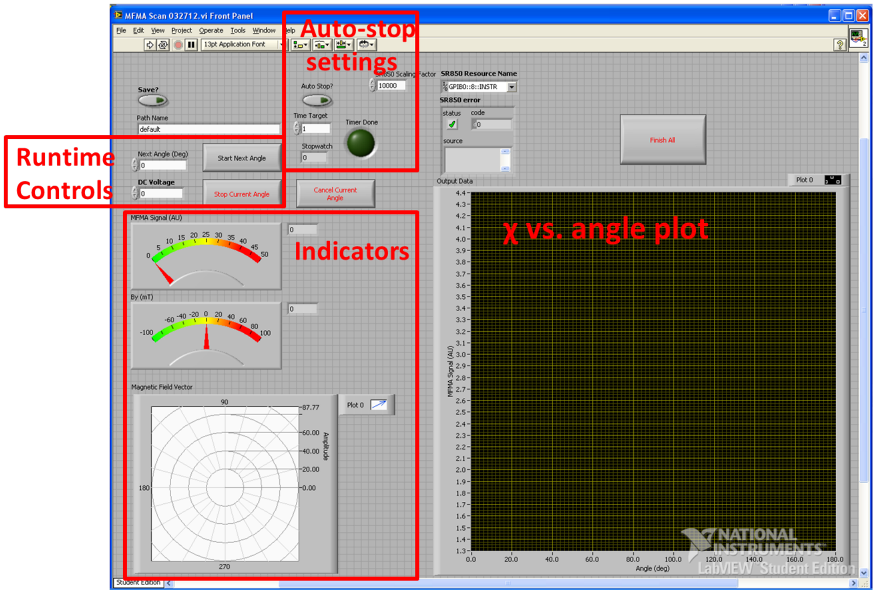

Path Name: default
Next Angle (Deg): 0
DC Voltage: 0
SR850 Scaling Factor: 10000
SR850 Resource Name: GPIB0::8::INSTR
Time Target: 1
Stopwatch: 0

Figure B.5: LabView interface for measuring MFMA anisotropy profiles

10 Hz and a peak-to-peak amplitude of 4 mT. In order to magnetize the sample along a particular axis, a large magnetic field is applied along the vertical axis of the sample. The field, at minimum, must be large enough to fully saturate the magnetic film or nanomagnets along their hard axis. The minimum field thus depends on the sample under investigation, and we typically found a strength of 40-50 mT to be sufficient to analyze nanomagnet arrays.

The LabView interface for an MFMA measurement is shown in Fig. B.5. After the sample has been positioned and the optical path aligned, the user starts the LabView program running. Next, the angle of the sample and the dc voltage from the photodiode are specified in the box labeled ‘Runtime controls’. Because the sample is physically rotated during the MFMA measurement, the dc voltage shifts slightly throughout the measurement, so the output voltage from the lock-in amplifier must be scaled by this dc voltage. Once these values are specified, the user presses the ‘start next angle’ button to begin averaging the measured amplifier voltage. The averaging process continues for the amount of time specified by the ‘autostop settings’, typically 30 s. The sample is then rotated to the next angle and the measurement is repeated. Over time, the graph of MFMA signal as a function of angle is populated and saved. In a typical measurement, data points are taken at 5° or 10° over a span of 180° (due to symmetry it is not necessary to measure a full circle). In post-processing, the MFMA values are inverted and graphed in a polar plot, such that easy axes show up as lobes.

Once the hard axes of the sample are identified, a second measurement may be performed to better quantify the anisotropy strength (the information contained in the anisotropy profile described above is mostly qualitative). In this measurement, the magnet is rotated with the hard axis in the vertical direction (the axis of the dc field) and the susceptibility is

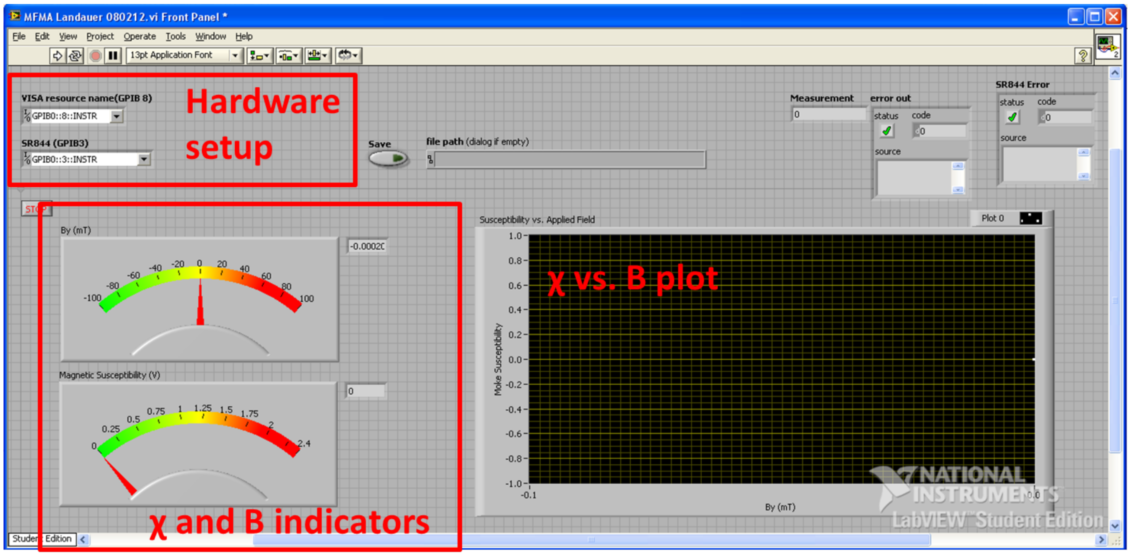
MFMA Landauer 080212.vi Front Panel *

VISA resource name(GPIB 8): GPIB0::8::INSTR

SR844 (GPIB3): GPIB0::3::INSTR

Measurement: 0

error out: status ✓ code 0

SR844 Error: status ✓ code 0

By (mT): -0.0002C

Magnetic Susceptibility (V): 0

Figure B.6: LabView interface for measuring MFMA anisotropy field

measured in the transverse direction using the same lock-in technique used to measure the anisotropy profile. However, rather than setting the dc field to a fixed value and measuring the susceptibility as a function of sample angle, the dc field is swept over a range of values. The goal is to identify the peak susceptibility as a function of the dc field, which corresponds to the field strength needed to saturate the sample along its hard axis. The larger the field that is required, the greater the anisotropy strength. The LabView interface for this technique is shown in Fig. B.6. It is a simple interface that graphs susceptibility as a function of applied magnetic field along the vertical axis. The magnetic field is typically swept by hand, as the Agilent waveform generator is already used to supply the 10 Hz waveform along the horizontal axis. In post-processing, the curve is averaged and the field at which the peak value occurs is picked out, representing the anisotropy field for this sample.

B.2 PEEM

X-ray magnetic circular dichroism photoelectron emission microscopy (XMCD-PEEM or PEEM) is one of the primary tools we used to capture magnetic contrast images with size resolution on the order of the size of the nanomagnets. The tool is located at the Advanced Light Source, Lawrence Berkeley National Laboratory at beamline 11.0.1. PEEM operates by illuminating a magnetic sample with circularly polarized X-rays under vacuum and imaging the photoelectrons that are ejected from the sample, as shown in Fig. B.7 (a). Two images are captured, one for left- and one for right- circularly polarized X-rays and the images are divided. In the resulting image, magnetic regions aligned in the plane of incidence of the X-ray beam show up as light or dark as a result of the XMCD effect. The photoelectron

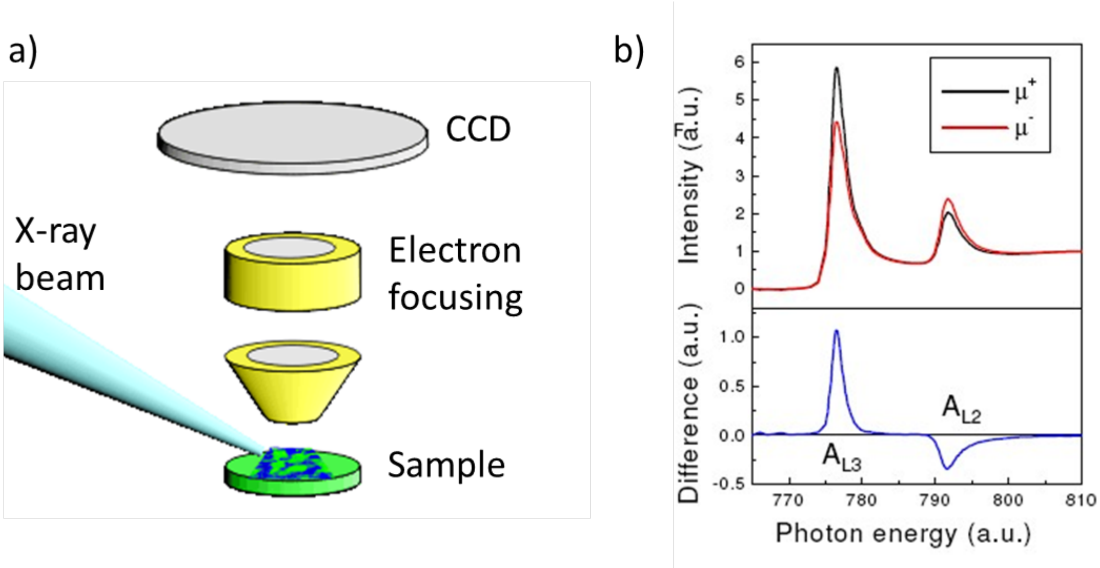

Figure B.7: (a) Illustration of the PEEM apparatus and (b) demonstration of XMCD at particular photon energies. Source: Advanced Light Source

intensity difference resulting from XMCD is illustrated in Fig. B.7 (b).

PEEM is a uniquely useful tool for us due to its sharp spatial and magnetic contrast and high imaging throughput after loading a sample. We regularly achieved spatial resolution on the order of 50 nm in PEEM, sufficient to clearly distinguish the magnetization states of neighboring nanomagnetes in an NML circuit. Equally importantly, we often imaged hundreds or even thousands of NML devices in a period of several hours due to the relatively wide field of view and built-in ability to quickly translate the sample stage in PEEM. Other benefits of PEEM include its temperature-controlled sample stage and the ability to set up automated image scans that take repeated images without user intervention. One limitation of PEEM is the relatively long setup time, often several hours, which limits the numbers of samples that can be imaged in any one session to only about one or two.

During our experience using PEEM we developed an understanding of capping layers and their effect on imaging resolution. PEEM is a highly surface sensitive measurement technique, so our early PEEM measurements failed to generate good images because our magnets oxidized or conversely because we used a Cr capping layer that was too thick to image through, up to about 5 nm. We eventually found an optimal capping layer to consist of 1.5-2 nm of Al. This is sufficiently thick to prevent the underlying magnetic material from oxidizing quickly, but is thin enough to allow the X-ray illumination to penetrate to the magnetic layer and for the resulting photoelectrons to escape the sample. Al is also advantageous over Cr because its oxide is not antiferromagnetic whereas the Cr oxide is, which risks biasing the results. Specific applications of PEEM and the techniques we used to obtain our results are discussed in Chapters 4, 5, and 7.

Appendix C

Micromagnetic simulations

Almost every experiment that we carried out was preceded by micromagnetic simulations. Our simulation tools were used to verify hypotheses, optimize sample design, and predict experimental outcomes. Two simulation tools in particular played a central role in the studies presented in this dissertation, one based on custom built MATLAB code and the other based on publicly available OOMMF software. Both have similar functionality: calculate the evolution of a micromagnetic system by solving the Landau-Lifshitz-Gilbert equation for each magnetic domain that makes up the system [36]. The difference lies primarily in how the magnetic domains are discretized, which leads to their applicability to different types of problems.

C.1 MATLAB Simulations

Overview

The key elements of a typical MATLAB micromagnetic simulation are described in Fig. C.1. First, the parameters that define a nanomagnet using a single-spin approximation

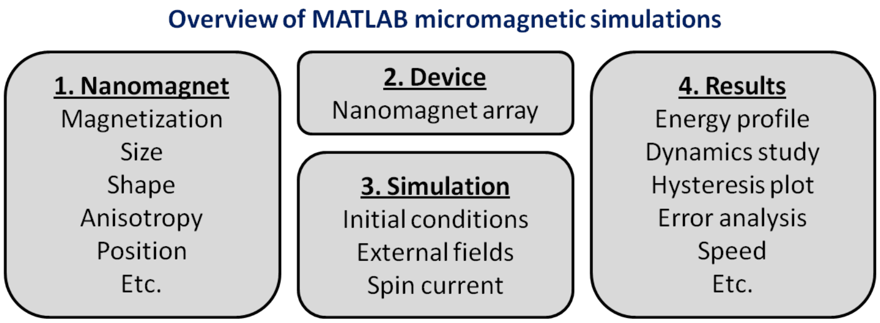

Figure C.1: Overview of micromagnetic simulations in MATLAB are encapsulated in a data structure. The relevant information stored in the nanomagnet structure includes but is not limited to the magnetization vector and its evolution over time, the anisotropy energy, the volume, and the position in relation to other nanomagnets in the device. Second, a device that comprises multiple nanomagnets is defined such that the interactions among neighbors may be accounted for. Third, a simulation is run. Several types of simulation may be run, but typically we are interested in calculating the evolution of the system in response to time-dependent external stimuli like magnetic fields and spin transfer torques. Whether or not the effect of temperature is included is also an important decision. Finally, the simulation outputs data, which can take various forms depending on the application. Fig. C.2 illustrates a sampling of the variety of applications that MATLAB micromagnetic simulations may be used in.

Specifications

The `singlespin` class The central element of a MATLAB simulation is a class called '`singlespin`' which represents a single nanomagnet. The `singlespin` class encapsulates all of the fixed parameters of a magnet such as its saturation magnetization, variable parameters such as its current magnetization vector, and also its history of magnetization as a function of time or applied field. An instance of the `singlespin` class is called by:

```
myspin = singlespin(dim,Ms,M0,Eu,Eb,H,temp,alpha,pos,tilt)
```

where `dim` is a 3-component vector representing the X, Y, and Z dimensions of the magnet in nm, `Ms` is the saturation magnetization, `M0` is a 3-component unit vector representing the initial magnetization orientation, `Eu` is the uniaxial anisotropy energy in eV, `Eb` is the biaxial anisotropy energy in eV, `H` is the external magnetic field, `temp` is the sample temperature, `alpha` is the Gilbert damping constant, `pos` is a 3-component vector representing the center position of the magnet, and `tilt` is the angle of the shape relative to the vertical axis. The geometry of a `singlespin` element is depicted in Fig. C.3.

Given a spin with specified dimensions, the `singlespin` class calculates the demagnetization factors based on the assumption that the nanomagnet has a three dimensional ellipse shape. The procedure for calculating the demagnetization factors is given by Ref. [58]. These terms result in a third anisotropy energy Esh in addition to the user-defined Eu and Eb. These three anisotropy energies sum up to define the full anisotropy profile of the `singlespin` element. Intrinsic parameters such as the temperature and Gilbert damping constant are stored and returned when requested by another function.

Characterizing a `singlespin` element Several functions were developed to graphically represent the properties of a `singlespin` element. These include:

- `plotenergyprofile()`: produces a plot of the energy landscape of the `singlespin` element in the xy plane

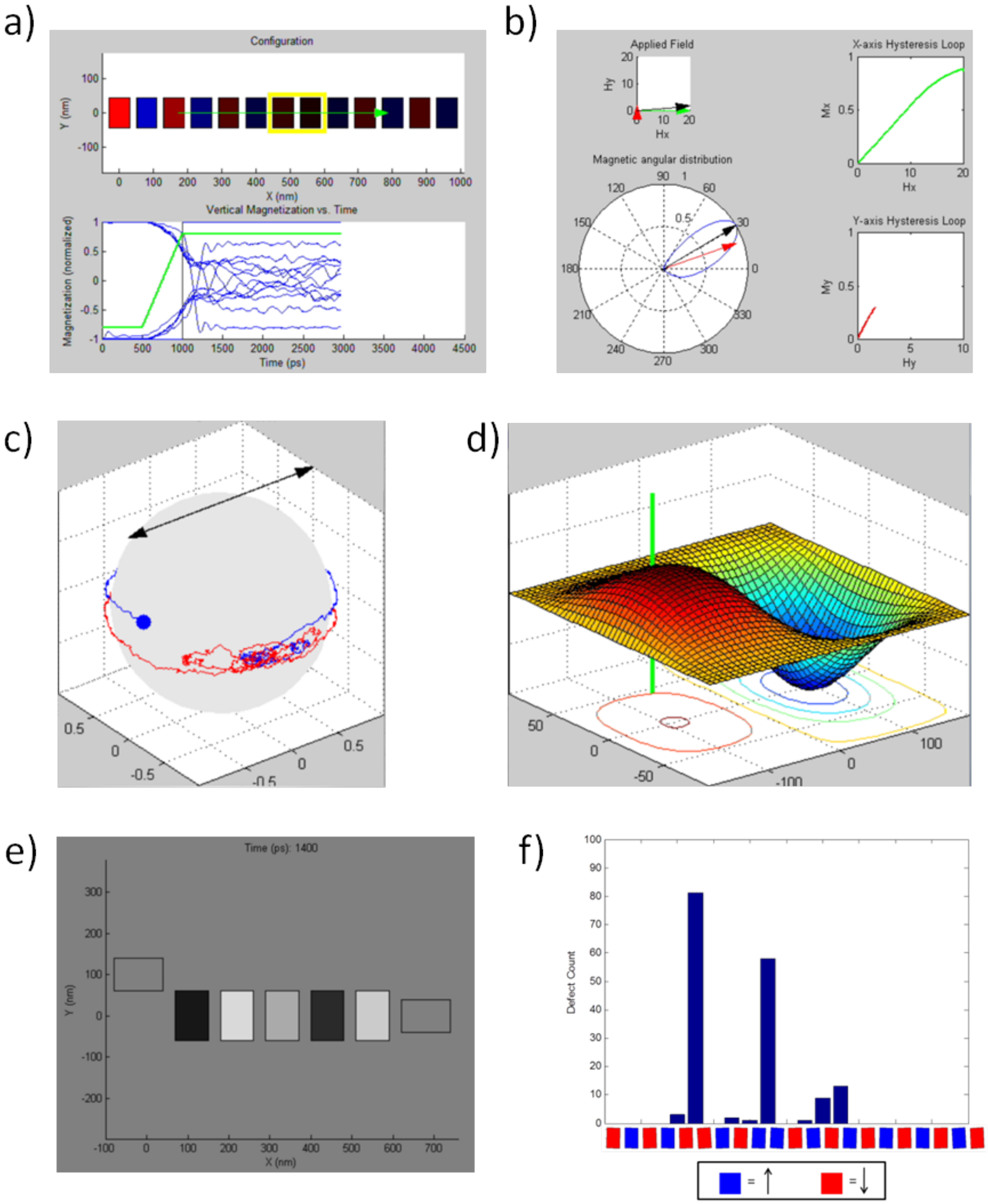

Figure C.2: Examples of applications of MATLAB micromagnetic simulations: (a) Observation of random-walk dynamics in nanomagnet chain; (b) evolution of a nanomagnet during Landauer erasure; (c) conversion of information to energy in a nanomagnet coupled to a thermal bath; (d) three dimensional energy profile of a nanomagnet; (e) simulation correponding to a PEEM experiment; (f) histogram of error distribution of a non-ideal nanomagnet chain.

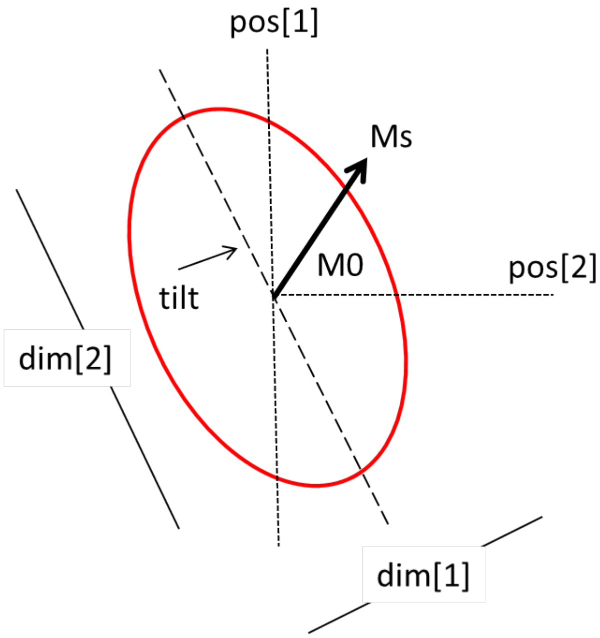

Figure C.3: Diagram mapping variables of the `singlespin` class to geometric features of a nanomagnet

- `plotenergyprofile3d()`: produces a plot of the energy landscape in three dimension.
- `drawnanomagnet()`: draws a rectangular element with dimensions corresponding to the xy-dimensions of the `singlespin` element and whose color varies from red to blue depending on the Y-component of the magnetization
- `drawdipole3d()`: renders a three-dimensional sphere with a red and blue dot indicating the north and south pole of the magnetization of the `singlespin` element in three dimensions. Optionally, thin lines tracing the history of the magnetization over time can be rendered as well

These programs serve as utility functions and supply the graphical output for a variety of simulations. The energy profile functions are also useful in some standalone cases for evaluating or comparing the effect of changes in shape, anisotropy, or applied field on the energy landscape.

Evolving a `singlespin` element Given a `singlespin` element with a known magnetization and external fields, it is possible to calculate its state a short time later using the Landau-Lifshitz-Gilbert equation. We coded several MATLAB functions to evolve the state of a `singlespin` element by a single timestep using the finite difference midpoint technique described by D'Aquino *et al.* [36]. This method requires an optimization step, for which we use the `fsolve()` function from the MATLAB optimization toolbox. For best performance, the Levenberg-Marquadt algorithm is used and the cross-product in the LLG equation is calculated explicitly rather than using the built-in `cross()` function.

- `llgevolve()`: Solves the most basic form of the LLG equation without accounting for temperature or spin transfer torque. The equation that describes the spin dynamics is:
  $$\frac{d\mathbf{m}}{dt} = -\left|\gamma\right| \mathbf{H_{eff}} \times \mathbf{m} + \alpha\mathbf{m} \times \frac{d\mathbf{m}}{dt} \tag{C.1}$$
  where γ is the gyromagnetic ratio, and α is the Gilbert damping constant.
- `sttevolve()`: Includes a term in addition to the basic LLG equation to account for spin transfer torque as specified by Ref. [59]. The LLG equation now takes the form:
  $$\frac{d\mathbf{m}}{dt} = -\left|\gamma\right| \mathbf{H_{eff}} \times \mathbf{m} + \alpha\mathbf{m} \times \frac{d\mathbf{m}}{dt} + u \cdot \mathbf{m} \times \left(\mathbf{m} \times \frac{d\mathbf{m}}{dx}\right) + \beta \cdot u \cdot \mathbf{m} \times \frac{d\mathbf{m}}{dx} \tag{C.2}$$
  where u is a parameter proportional to the spin current density and β is the non-adiabatic spin torque component
- `stttempevolve()`: Additionally includes a random field term that simulates the effect of temperature. The LLG equation (neglecting the spin torque terms) now has the form:
  $$\frac{d\mathbf{m}}{dt} = -\left|\gamma\right| \left(\mathbf{H_{eff}} + \nu\mathbf{H_N}\right) \times \mathbf{m} + \alpha\mathbf{m} \times \frac{d\mathbf{m}}{dt} \tag{C.3}$$
  where $\nu\mathbf{H_N}$ is the random thermal field, an isotropic white-noise vector whose components are independent Gaussian random variables with variance ν^2.
- `tiltevolve()`: Handles nanomagnets with an easy axis that is offset from the X or Y axis by a tilt angle.
- `biaxevolve()`: Handles nanomagnets with a biaxial anisotropy term in addition to the uniaxial anisotropy energy

Each time one of these functions is called, the simulation is iterated by one timestep, typically a parameter that is set to about 0.1-10 ps. To carry out a full simulation of a nanomagnet device over the course of nanoseconds, the evolve functions must be placed inside of a loop and called repeatedly.

Simulating a nanomagnetic logic circuit In order to simulate a nanomagnetic device consisting of multiple nanomagnets, the dipole interactions among neighboring nanomagnets must be accounted for. First, the positions of all nanomagnets must be defined relative to one another. This is accomplished by generating a data structure that contains a number of `singlespin` elements with their center positions specified such that the circuit has the desired geometry. Next, this data structure is passed to a function called `couplingmatrix` which outputs a matrix that defines the coupling interactions between all pairs of nanomagnets. The size of the coupling matrix is n x n x 3 x 3, where n is the number of `singlespin` elements in the device. For each pair of nanomagnets ij, the reduced matrix is a 3 x 3 array that specifies the coupling interaction in 3 dimensions:

$$C_{ij} = \frac{\mu_0}{4\pi r^5}\begin{bmatrix} 3x^2 - r^2 & 3xy & 3xz \\ 3yx & 3y^2 - r^2 & 3yz \\ 3zx & 3zy & 3z^2 - r^2 \end{bmatrix} \tag{C.4}$$

where x, y, and z are the distances between the pair of magnets in the three dimensions and $r^2 = x^2 + y^2 + z^2$. In order to calculate the total dipole field at the ith magnet at a particular timestep, the coupling matrix is multiplied by the magnetization state of all of the other magnets in the device and the resulting field vectors are added up. This sum is added to the external applied field and the internal anisotropy fields of the nanomagnet to yield the total effective field H_{eff}. Once H_{eff} is known it is possible to invoke one of the evolver functions to calculate the LLG equation for that timestep. The process is then iterated until the simulation is complete.

C.2 OOMMF Simulations

Overview

For simulations in which the single spin approximation is inadequate, the relatively poor performance of the MATLAB based simulation prohibits its use. In these cases, the performance-optimized OOMMF software package is used instead [50]. While not as flexible as a MATLAB simulation that is built from the ground up, OOMMF is able to address many problems related to nanomagnetic logic and has several useful packages that expand its applicability. One of the main applications of OOMMF is to devices in which the nonuniform internal magnetization configuration of a magnetic element is relevant to its behavior. Specific applications include nanomagnets with configurational anisotropy and/or domain walls. Examples of results of OOMMF simulations are shown in Fig. C.4.

For extensive parametric studies, even OOMMF simulations do not offer high enough performance to generate results in a reasonable amount of time when it runs on a typical desktop computer. As a result, we applied for and received access to a computing cluster located at UC Berkeley, the IBM-CITRIS cluster. This resource has 132 processors that can be used to run multiple simulations in parallel. Control software was developed to

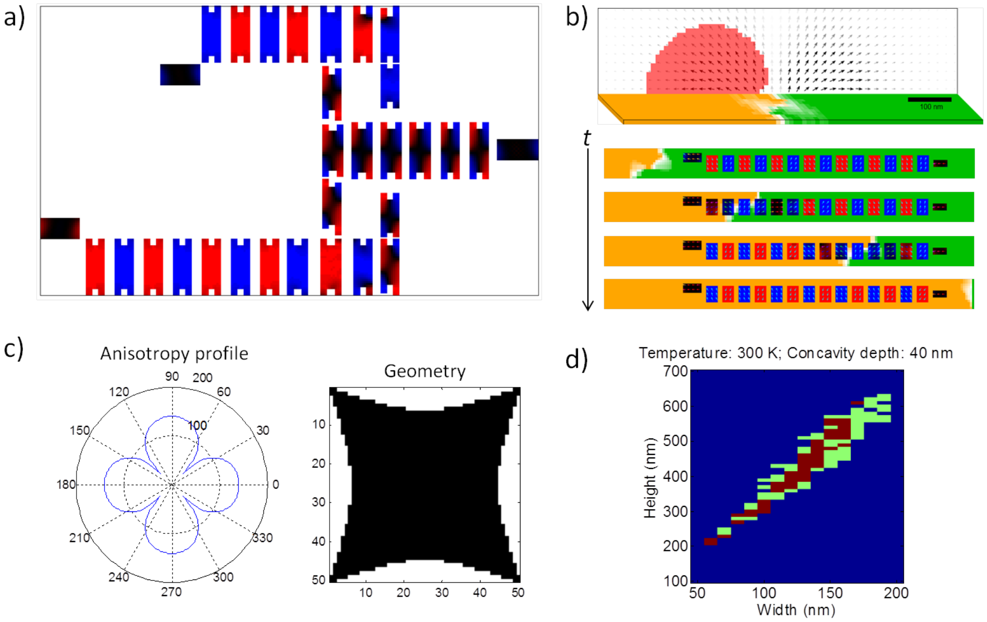

Figure C.4: Examples of applications of OOMMF micromagnetic simulations: (a) Configurational B-gate that functions correctly at 0K; (b) spin torque driven domain wall being used to clock a nanomagnet chain with its stray fields; (c) anisotropy profile of a concave nanomagnet with configurational anisotropy; (d) parametric study of concave nanomagnet chains carried out on the IBM-CITRIS cluster.

automate the launching and analysis of OOMMF simulations on the IBM-CITRIS cluster. Applications thus far have included parametric studies of the strength of configurational anisotropy as a function of geometry and the optimization of concave nanomagnet chains.

Specifications

Image generation The input for an OOMMF simulation is an image file in which pixels are color-coded to represent their initial conditions. For example, white pixels may represent non-magnetic regions, green pixels may be initially magnetized to the right, and blue pixels may be fixed spins that do not evolve during the simulation. These image files can be drawn by hand or generated by an automated script. A MATLAB image generator script was used to generate large batches of nanomagnet chains for parametric studies, taking the positions and dimensions of nanomagnets as input parameters. A different script was used to generate concave shaped nanomagnets in which the concavity shape was a hyperbola; such a curved edge would have been difficult to draw by hand.

Batch simulations Defining simulation parameters in a .mif2 document and running individual simulations given an input image file is follows straightforwardly from the OOMMF user's manual. When running batch simulations, we found that some customization was needed. An example of a batch file is shown below, in which the iterator `A` is passed as a parameter to the simulation file `mysim.mif2`:

```
FOR /L %%A IN (1,1,10) DO ^
tclsh oommf.tcl boxsi -threads 1 -parameters "sim %%A" mysim.mif2
```

The value of `A`, which in this case has a range of 1-10, is used by OOMMF to select the input image file e.g. `image-A.bmp` and other input and output parameters. Combined with image generation scripts, running batch simulations is a powerful and convenient tool for running parametric studies of nanomagnets of varying shapes and sizes.

Anisotropy profile generation One application of OOMMF is to generate anisotropy profiles similar to those obtained experimentally using the MFMA technique described in Appendix B. The image file in this type of simulation is a single nanomagnet with the desired shape or anisotropy properties to be studied. Using the `Oxs_ScriptUZeeman` specification in OOMMF that allows the user to define a variable magnetic field, a rotating magnetic field is of constant magnitude applied in increments of about 4°. As in the MFMA technique, the field is large enough to nearly saturate the nanomagnet along its hard axis. At each angle, the average magnetization vector of the sample is saved. What is important is the component of the magnetization vector orthogonal to the angle of the applied field. The difference in the orthogonal magnetization components of two neighboring points is proportional to the transverse susceptibility at the center point. For example, the difference between the magnetization when the magnetic field is oriented at -2° and 2° is related to the transverse susceptibility at 0°. A MATLAB script is used to automate this calculation around a full circle, and the output is a polar plot of the inverse transverse susceptibility as a function of angle that contains equivalent information to an experimental MFMA anisotropy profile.

Bibliography

[1] G.E. Moore. Cramming more components onto integrated circuits. *Proceedings of the IEEE*, 86(1):82 –85, Jan. 1998.

[2] J.G. Koomey, S. Berard, M. Sanchez, and H. Wong. Implications of historical trends in the electrical efficiency of computing. *Annals of the History of Computing, IEEE*, 33(3):46 –54, March 2011.

[3] Brown R, Masanet E, Nordman B, Tschudi B, Shehabi A, and Stanley J. Report to congress on server and data center energy efficiency: public law, 2007.

[4] International technology roadmap for semiconductors.

[5] P.M. Solomon, I. Lauer, A. Majumdar, J.T. Teherani, M. Luisier, J. Cai, and S.J. Koester. Effect of uniaxial strain on the drain current of a heterojunction tunneling field-effect transistor. *Electron Device Letters, IEEE*, 32(4):464 –466, april 2011.

[6] T.-J.K. Liu, D. Markovic, V. Stojanovic, and E. Alon. The relay reborn. *Spectrum, IEEE*, 49(4):40 –43, april 2012.

[7] Hei Kam, Tsu-Jae King Liu, and E. Alon. Design requirements for steeply switching logic devices. *Electron Devices, IEEE Transactions on*, 59(2):326 –334, feb. 2012.

[8] T.L. Gilbert. A phenomenological theory of damping in ferromagnetic materials. *Magnetics, IEEE Transactions on*, 40(6):3443 – 3449, nov. 2004.

[9] William Fuller Brown. Thermal fluctuations of a single-domain particle. *Phys. Rev.*, 130:1677–1686, Jun 1963.

[10] E. C. Stoner and E. P. Wohlfarth. A mechanism of magnetic hysteresis in heterogeneous alloys. *Phil. Trans. R. Soc. Lond. A*, 240(826):599–642, 1948.

[11] J.I Martn, J Nogus, Kai Liu, J.L Vicent, and Ivan K Schuller. Ordered magnetic nanostructures: fabrication and properties. *Journal of Magnetism and Magnetic Materials*, 256(13):449 – 501, 2003.

[12] S. I. Kiselev, J. C. Sankey, I. N. Krivorotov, N. C. Emley, R. J. Schoelkopf, R. A. Buhrman, and D. C. Ralph. Microwave oscillations of a nanomagnet driven by a spin-polarized current. *Nature*, 425:380–383, 2003.

[13] R. P. Cowburn and M. E. Welland. Room Temperature Magnetic Quantum Cellular Automata. *Science*, 287(5457):1466–1468, 2000.

[14] R. P. Cowburn. Magnetic nanodots for device applications. *Journal of Magnetism and Magnetic Materials*, 242-245(Part 1):505 – 511, 2002.

[15] K.M. Krishnan. Biomedical nanomagnetics: A spin through possibilities in imaging, diagnostics, and therapy. *Magnetics, IEEE Transactions on*, 46(7):2523 –2558, july 2010.

[16] C S Lent, P D Tougaw, W Porod, and G H Bernstein. Quantum cellular automata. *Nanotechnology*, 4(1):49, 1993.

[17] A. Imre, G. Csaba, L. Ji, A. Orlov, G. H. Bernstein, and W. Porod. Majority Logic Gate for Magnetic Quantum-Dot Cellular Automata. *Science*, 311(5758):205–208, 2006.

[18] D. B. Carlton, N. C. Emley, E. Tuchfeld, and J. Bokor. Simulation studies of nanomagnet-based logic architecture. *Nano Letters*, 8(12):4173–4178, 2008.

[19] Brian Lambson, David Carlton, and Jeffrey Bokor. Exploring the thermodynamic limits of computation in integrated systems: Magnetic memory, nanomagnetic logic, and the landauer limit. *Phys. Rev. Lett.*, 107:010604, Jul 2011.

[20] Behtash Behin-Aein, Deepanjan Datta, Sayeef Salahuddin, and Supriyo Datta. *Nature Nanotech.*, pages 266–270, 2010.

[21] S. S. P. Parkin, K. P. Roche, M. G. Samant, P. M. Rice, R. B. Beyers, R. E. Scheuerlein, E. J. O'Sullivan, S. L. Brown, J. Bucchigano, D. W. Abraham, Y. Lu, M. Rooks, P. L. Trouilloud, R. A. Wanner, and W. J. Gallagher. Exchange-biased magnetic tunnel junctions and application to nonvolatile magnetic random access memory (invited). *Journal of Applied Physics*, 85:5828–5833, April 1999.

[22] S. S. P. Parkin, C. Kaiser, A. Panchula, P. M. Rice, B. Hughes, M. Samant, and S.-H. Yang. Giant tunnelling magnetoresistance at room temperature with MgO (100) tunnel barriers. *Nature Materials*, 3:862–867, December 2004.

[23] S. Yuasa, T. Nagahama, A. Fukushima, Y. Suzuki, and K. Ando. Giant room-temperature magnetoresistance in single-crystal Fe/MgO/Fe magnetic tunnel junctions. *Nature Materials*, 3:868–871, December 2004.

[24] Luqiao Liu, Chi-Feng Pai, Y. Li, H. W. Tseng, D. C. Ralph, and R. A. Buhrman. Spin-torque switching with the giant spin hall effect of tantalum. *Science*, 336(6081):555–558, 2012.

[25] M.T. Niemier, X.S. Hu, M. Alam, G. Bernstein, W. Porod, M. Putney, and J. DeAngelis. Clocking structures and power analysis for nanomagnet-based logic devices. In *Low Power Electronics and Design (ISLPED), 2007 ACM/IEEE International Symposium on*, pages 26 –31, aug. 2007.

[26] Rolf Landauer. Irreversibility and heat generation in the computing process. *IBM J. Res. Dev.*, 5(3):183, Jul 1961.

[27] Charles Bennett. The thermodynamics of computationa review. *Int. J. Theor. Phys.*, 21(12):905–940, Dec 1982.

[28] Edward Fredkin and Tommaso Toffoli. Conservative logic. *International Journal of Theoretical Physics*, 21:219–253, 1982.

[29] O. J. E. Maroney. Generalizing landauer's principle. *Phys. Rev. E*, 79(3):031105, Mar 2009.

[30] Takahiro Sagawa and Masahito Ueda. Minimal energy cost for thermodynamic information processing: Measurement and information erasure. *Phys. Rev. Lett.*, 102(25):250602, Jun 2009.

[31] Raoul Dillenschneider and Eric Lutz. Memory erasure in small systems. *Phys. Rev. Lett.*, 102(21):210601, May 2009.

[32] Jan Liphardt, Sophie Dumont, Steven B. Smith, Ignacio Tinoco, and Carlos Bustamante. Equilibrium information from nonequilibrium measurements in an experimental test of jarzynski's equality. *Science*, 296(5574):1832–1835, 2002.

[33] Shoichi Toyabe, Takahiro Sagawa, Masuhito Ueda, Eiro Muneyuki, and Masaki Sano. Experimental demonstration of information-to-energy conversion and validation of the gerneralized jarzynski equality. *Nature Physics*, 6(12):988–992, 2010.

[34] Antoine Berut, Artak Arakelyan, Artyom Petrosyan, Sergio Ciliberto, Raoul Dillenschneider, and Eric Lutz. Experimental verification of landauer's prinicple linking information and thermodynamics. *Nature*, 483(7388):187–189, 2012.

[35] Charles H. Bennett. Notes on landauer's principle, reversible computation, and maxwell's demon. *Studies In History and Philosophy of Science Part B: Studies In History and Philosophy of Modern Physics*, 34(3):501 – 510, 2003. Quantum Information and Computation.

[36] M. d'Aquino, C. Serpico, G. Coppola, I. D. Mayergoyz, and G. Bertotti. Midpoint numerical technique for stochastic landau-lifshitz-gilbert dynamics. *Journal of Applied Physics*, 99(8):08B905, 2006.

[37] B. Behin-Aein, S. Salahuddin, and S. Datta. Switching energy of ferromagnetic logic bits. *IEEE Transactions on Nanotechnology*, 8(4):505 –514, july 2009.

[38] O.J.E. Maroney. The (absence of a) relationship between thermodynamic and logical reversibility. *Studies In History and Philosophy of Science Part B: Studies In History and Philosophy of Modern Physics*, 36(2):355 – 374, 2005.

[39] D. Carlton, B. Lambson, A. Scholl, A. Young, P. Ashby, S. Dhuey, E. Tuchfeld, and J. Bokor. Computing in thermal equilibrium with dipole-coupled nanomagnets. *Nanotechnology, IEEE Transactions on*, PP(99):1, 2011.

[40] M. P. Sharrock. Time dependence of switching fields in magnetic recording media (invited). *Journal of Applied Physics*, 76(10):6413–6418, 1994.

[41] R. P. Cowburn, A. Ercole, S. J. Gray, and J. A. C. Bland. A new technique for measuring magnetic anisotropies in thin and ultrathin films by magneto-optics. *J. Appl. Phys.*, 81(10):6879–6883, 1997.

[42] Brian Lambson, Zheng Gu, David Carlton, Scott Dhuey, Andreas Scholl, Andrew Doran, Anthony Young, and Jeffrey Bokor. Cascade-like signal propagation in chains of concave nanomagnets. *Applied Physics Letters*, 100(15):152406, 2012.

[43] Anna Carlsund. First passage time for random walks and birth-and-death processes with sign depending transition probabilities. *Licentiate Thesis*, 1991.

[44] D. Carlton, B. Lambson, A. Scholl, A. Young, P. Ashby, S. Dhuey, and J. Bokor. Investigation of defects and errors in nanomagnetic logic circuits. *Nanotechnology, IEEE Transactions on*, 11(4):760 –762, july 2012.

[45] R. P. Cowburn, A. O. Adeyeye, and M. E. Welland. Configurational anisotropy in nanomagnets. *Phys. Rev. Lett.*, 81:5414–5417, Dec 1998.

[46] R. P. Cowburn and M. E. Welland. Micromagnetics of the single-domain state of square ferromagnetic nanostructures. *Phys. Rev. B*, 58:9217–9226, Oct 1998.

[47] R P Cowburn. Property variation with shape in magnetic nanoelements. *Journal of Physics D: Applied Physics*, 33(1):R1, 2000.

[48] D. K. Koltsov and M. E. Welland. Control of micromagnetics in permalloy nanomagnets by means of indentation. *J. Appl. Phys.*, 94(5):3457–3461, 2003.

[49] F. Lee. Shape-induced biaxial anisotropy in thin magnectic films. *Magnetics, IEEE Transactions on*, 4(3):502 – 506, sep 1968.

[50] M.J. Donahue and D.G. Porter. Oommf user's guide, version 1.0. Technical report, National Institute of Standards and Technology, Gaithersburg, MD, Sept 1999.

[51] A. Kozhanov and S. J. Allen. Nanomagnetic triangles for a non-volatile logic applications. In *APS Meeting Abstracts*, page 15003, February 2012.

[52] J. Wang, J. B. Neaton, H. Zheng, V. Nagarajan, S. B. Ogale, B. Liu, D. Viehland, V. Vaithyanathan, D. G. Schlom, U. V. Waghmare, N. A. Spaldin, K. M. Rabe, M. Wuttig, and R. Ramesh. Epitaxial bifeo3 multiferroic thin film heterostructures. *Science*, 299(5613):1719–1722, 2003.

[53] J. Atulasimha and S. Bandyopadhyay. Bennett clocking of nanomagnetic logic using multiferroic single-domain nanomagnets. *Applied Physics Letters*, 97(17):173105, 2010.

[54] I. N. Krivorotov, N. C. Emley, J. C. Sankey, S. I. Kiselev, D. C. Ralph, and R. A. Buhrman. Time-domain measurements of nanomagnet dynamics driven by spin-transfer torques. *Science*, 307(5707):228–231, 2005.

[55] A. Gruber, A. Drbenstedt, C. Tietz, L. Fleury, J. Wrachtrup, and C. von Borczyskowski. Scanning confocal optical microscopy and magnetic resonance on single defect centers. *Science*, 276(5321):2012–2014, 1997.

[56] E. Beaurepaire, J.-C. Merle, A. Daunois, and J.-Y. Bigot. Ultrafast spin dynamics in ferromagnetic nickel. *Phys. Rev. Lett.*, 76:4250–4253, May 1996.

[57] D A Allwood, Gang Xiong, M D Cooke, and R P Cowburn. Magneto-optical kerr effect analysis of magnetic nanostructures. *Journal of Physics D: Applied Physics*, 36(18):2175, 2003.

[58] J. A. Osborn. Demagnetizing factors of the general ellipsoid. *Physical Review*, 1945.

[59] A. Thiaville, Y. Nakatani, J. Miltat, and Y. Suzuki. Micromagnetic understanding of current-driven domain wall motion in patterned nanowires. *EPL (Europhysics Letters)*, 69(6):990, 2005.